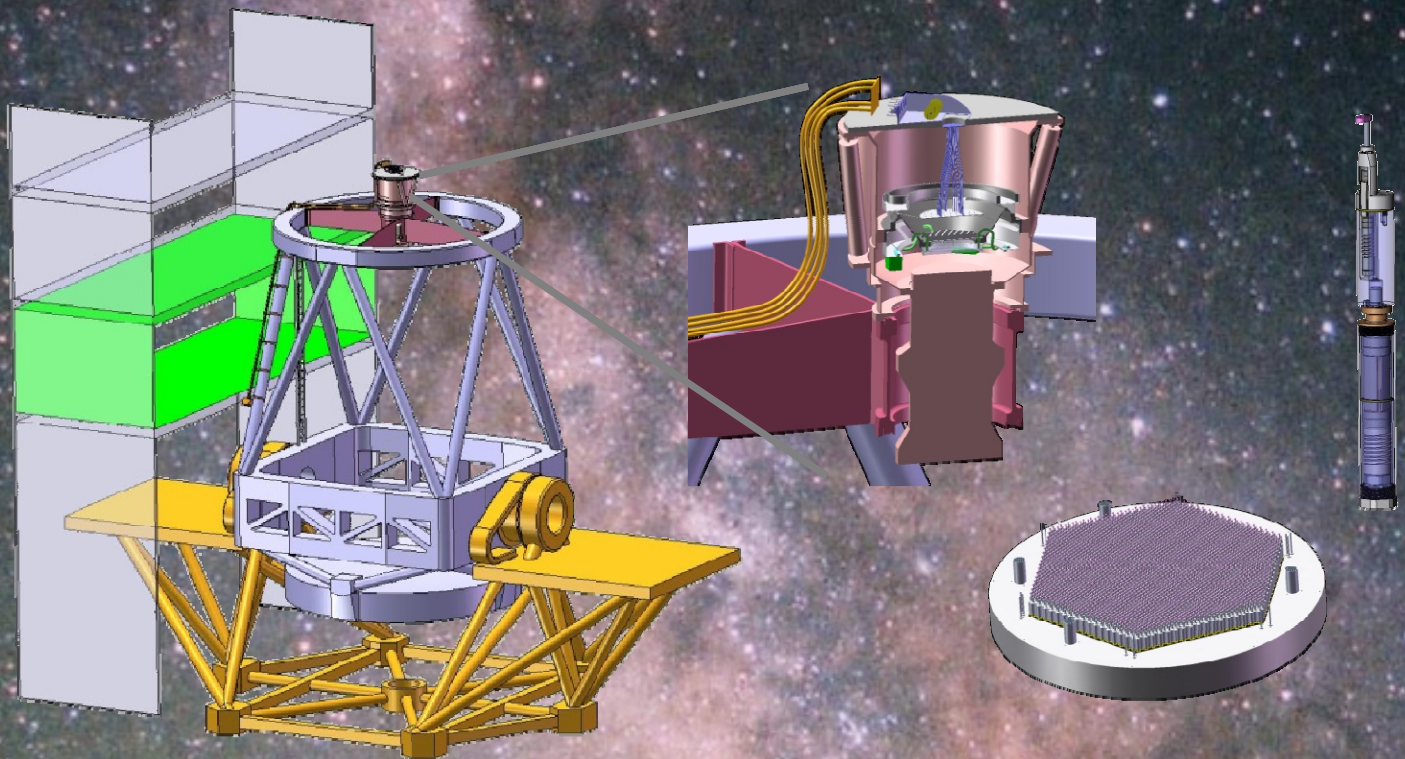


WIDE FIELD FIBER-FED OPTICAL MULTI-OBJECT SPECTROMETER

WF MOS

OPERATIONAL CONCEPT DESIGN DOCUMENT (OCDD)

JANUARY 30, 2009



CALTECH



JPL

Document Title	WMOS Initial Operational Concept Design Document
Issue	1.1
Date	January 30, 2009

Contributors to the WMOS Study:

Richard Ellis, *Principal Investigator, Caltech*

Mary White, *Project Manager, JPL*

Robin Bruno, *Proposal Manager, JPL*

Michael Seiffert, *Project Scientist, JPL*

Stuart Lynn, *IfA, Univ. of Edinburgh*

Peder Norberg, *IfA, Univ. of Edinburgh*

John Peacock, *IfA, Univ. of Edinburgh*

Fergus Simpson, *IfA, Univ. of Edinburgh*

Masahiro Takada, *IPMU, University of Tokyo*

Masami Ouchi, *Carnegie Observatories*

Thomas Kitching, *Univ. of Oxford*

Filipe Abdalla, *Univ. College London*

Ofer Lehav, *Univ. College London*

Ignacio Ferreras, *MSSL—Univ College London
Laerte Sodre, Sau Paulo*

Scott Chapman, *Inst. of Astronomy, Univ. of
Cambridge*

Mike Irwin, *Inst. of Astronomy, Univ. of
Cambridge*

Geraint Lewis, *School of Physics, Univ. of Sydney*

Rodrigo Ibata, *Observatoire de Strasbourg*

Vanessa Hill, *Observatoire de Paris*

Alan McConnachie, *Dept. of Physics and
Astronomy, Univ. of Victoria*

Kim Venn, *Dept. of Physics and Astronomy, Univ.
of Victoria*

Mark Wilkinson, *Dept. of Physics & Astronomy,
University of Leicester*

Nobuo Arimoto, *National Astronomical
Observatory of Japan*

Amina Helmi, *Kapteyn Astronomical Institute,
Univ. of Groningen*

Chris Evans, *UK Astronomy Technology Centre, Royal
Observatory, Edinburgh*

Beatriz Barbuy, *Universidade de Sao Paulo, IAG*

Luciana Pompeia, *IP&D, Universidade do Vale do
Paraiba*

Dante Minniti, *Dept. of Astronomy, Pontificia
Universidad Catolica*

Rich Dekany, *Caltech*

Anna Moore, *Caltech*

Roger Smith, *Caltech*

Steven Beard, *UK Astronomy Technology Centre*

Ian Bryson, *UK Astronomy Technology Centre*

Andy Vick, *UK Astronomy Technology Centre*

Peter Doel, *Univ. College London*

Dave King, *Univ. of Cambridge*

Ian Parry, *Univ. of Cambridge*

Dave Braun, *JPL*

Charles Fisher, *JPL*

Amanda Frieze, *JPL*

Larry Hovland, *JPL*

Muthu Jeganathan, *JPL*

Joel Kaluzny, *JPL*

Roger Lee, *JPL*

Norman Page, *JPL*

Lewis Roberts, *JPL*

S. Tere Smith, *JPL*

Ron Steinkraus, *JPL*

Karl Reichard, *Penn State University*

Antonio Cesar de Oliveira, *LNA, Brazil*

Ligia Souza de Oliveira, *LNA, Brazil*

Table of Contents

1	INTRODUCTION	1
1.1	Purpose of Document.....	1
1.2	Background	1
1.3	Instrument Identification	2
1.4	Document Layout	2
2	DOCUMENTS	3
2.1	Applicable Documents.....	3
3	WF MOS, DARK ENERGY, AND MODIFIED GRAVITY	4
3.1	The Challenge of Cosmic Acceleration	4
3.1.1	Dark Energy Observables	4
3.1.2	The Evolution of Dark Energy.....	6
3.1.3	Modified Gravity.....	7
3.2	Baryon Acoustic Oscillations	9
3.2.1	Standard Rulers.....	9
3.2.2	Precision of BAO Measurement	11
3.2.3	Non-linear Effects on BAOs.....	15
3.2.4	Scale-Dependent Bias.....	19
3.3	Expected Performance of WF MOS in Measuring the BAO Signature	20
3.3.1	Contrasting High and Low Redshift Surveys	22
3.3.2	Fisher Matrices and Figures of Merit.....	24
3.4	Redshift-Space Distortions and Modified Gravity	26
3.5	Further Applications and Challenges	29
3.5.1	Neutrino Mass Constraints	29
3.5.2	Galaxy Biasing.....	31
3.6	Lensing Synergy.....	34
3.6.1	Strategic Considerations	34
3.6.2	Benefits of Combining a BAO and 3-D Weak Lensing Survey	34
3.6.3	Broader Synergy between WF MOS and HSC.....	37
3.7	Proposed WF MOS Surveys	38
3.7.1	The International Perspective.....	38
3.7.2	Low-Redshift Survey	39
3.7.3	High-Redshift Survey.....	44
3.7.4	Requested Time	45
3.8	Summary of Survey Strategy for Dark Energy and Modified Gravity	47
4	STELLAR ARCHAEOLOGY AND GALAXY GENESIS	49
4.1	Science Case	49
4.1.1	Overview.....	49
4.1.2	Redesigning the Galactic Archaeology (GA Surveys)	50
4.1.3	Addressing the Big Questions	55
4.2	Detailed Survey Design.....	63

4.2.1	The Galactic Bulge	63
4.2.2	The Outer Disk	67
4.2.3	The Galactic Halo	68
4.2.4	Targeting Substructure; Streams & Dwarfs	71
4.2.5	Targeting M31 & M33	71
4.2.6	Overall Survey Design	71
4.3	Technical Considerations	73
4.3.1	Spectroscopic Requirements	73
4.3.2	Data Reduction Requirements	78
4.3.3	Continuum Estimation	80
4.3.4	Velocity and EW Estimation	80
4.3.5	Stellar Atmosphere Modelling	81
4.3.6	Chemical Tagging	83
4.4	Competition	84
5	GALAXY FORMATION AND LARGE SCALE STRUCTURE	87
5.1	Introduction	87
5.2	Strategic Issues	87
5.3	Sample Science Programs	88
5.3.1	A High Quality Spectroscopic Survey to $z \sim 1.6$	88
5.3.2	Studies of $z > 3$ galaxies	90
5.3.3	QSOs, Clusters, and Other Sources	91
5.3.4	Implications for Instrument Design	92
6	TECHNICAL DETAILS	93
6.1	Introduction	93
6.2	Target Catalogs – Dark Energy Surveys	93
6.3	Strategy for Target Selection	94
6.4	Predicting Emission Lines from Broad-Band Photometry	96
6.5	Spectroscopic Simulations – Dark Energy Surveys	97
6.6	Target Catalogs – Galactic Archaeology	99
6.7	Sky Subtraction	100
6.8	Fiber Allocation Efficiency	103
6.9	Fiber Diameter	107
6.10	Estimated Survey Time	108
6.10.1	Dark Energy	108
6.10.2	Galactic Archaeology	110
7	SCIENCE REQUIREMENTS SUMMARY	111
7.1	Dark Energy Science Objectives and Top Level Requirements	111
7.2	Galactic Archaeology Science Objectives and Top Level Requirements	113
8	INSTRUMENT DESCRIPTION	115
8.1	System Description	115
8.2	Instrument Operational Modes	119

8.2.1	Start-up.....	119
8.2.2	Target Acquisition.....	119
8.2.3	Observation.....	120
8.2.4	Calibration.....	121
8.2.5	Testing.....	122
9	OPERATIONAL CONCEPT MODEL.....	123
9.1	Introduction.....	123
9.2	WF MOS Observation Preparation.....	124
9.3	WF MOS Observation Execution.....	125
9.4	WF MOS Engineering.....	127
10	REFERENCES.....	129
11	ACRONYMS AND ABBREVIATIONS.....	133

List of Figures

Figure 3-1: Perturbation around $\Omega_m = 0.25$ and $w = -1$ of the dependence on redshift of the Hubble parameter H , the distance D and density growth factor g . The parameter p refers to either w or $\ln \Omega_m$; solid lines shows the effect of an increase in w , dashed lines the effect of an increase in Ω_m	6
Figure 3-2: Acoustic oscillations in the radiation-baryon fluid imprint a pattern in the Fourier spectrum of both CMB (top) and density (bottom) fluctuations (e.g., Meiksin, White & Peacock 1999). In the latter case the effect is much smaller, because the dominant dark matter has no intrinsic oscillations. Nevertheless, the same acoustic scale can be picked out at low and high redshift, opening the way to a relatively clean geometrical tool in cosmology.....	10
Figure 3-3: Confidence contours on the plane of w versus Ω_m from the WMAP year-3 data (Spergel et al. 2006). It is assumed that w does not evolve, and also that the universe is spatially flat, although this latter assumption is not critical.....	11
Figure 3-4: Increase in the power spectrum noise as a function of survey galaxy density. For a canonical value of the power spectrum of $2500 (h^{-1}\text{Mpc})^3$, and assuming more targets than fibers, a target density of $4 \times 10^{-4} h^3\text{Mpc}^{-3}$ optimizes survey efficiency. At lower densities, shot noise dominates the error on the power spectrum. Higher target density produces somewhat improved estimates, but such surveys are less efficient, leading to an overall noise increase if the survey is constrained to fixed total time.....	13
Figure 3-5: The matter power spectrum at $z = 1$ from an N-body simulation of a cube of side $2000 h^{-1} \text{Mpc}$. Linear theory (green line) is compared with nonlinear results, varying the spectrum normalization (zero-redshift σ_8). Note the suppression in power for wavenumbers beyond the principal peak at $k \approx 0.06 h\text{Mpc}^{-1}$, and the visible shift in peak location in the high-normalization case.....	17
Figure 3-6: The fractional shift in the location of the principal acoustic peak owing to large-scale quasilinear effects. These plots consider the mass distribution at $z = 1$ and varies the zero-redshift normalization, σ_8 , together with the spectral shape parameter, $\Omega_m h$ (first panel), and the baryon fraction, Ω_b/Ω_m (second panel).....	18
Figure 3-7: The power spectrum from the Millennium Simulation (Springel et al. 2005). The plot shows the linear power spectrum ratioed to a smooth model (black), the nonlinear mass power spectrum (red), and the galaxies (green), scaled to allow for bias.....	20
Figure 3-8: Expected performance of WF MOS for determining $D_A(z)$ and $H(z)$ at each redshift of the surveyed redshift slices based on the BAO geometrical test. The accuracy shown here is relative to the fiducial model with cosmological constant. We have assumed WF MOS surveys that differ from the feasibility survey, consistent with our final proposals.....	22

- Figure 3-9:** 68% error on w_p , marginalized over other parameter uncertainties, for the model $w(a) = w_p + w_a(a - a_p)$ with varying parameter a_p . The errors are for WF MOS combined with SDSS ($z < 0.3$) and Planck. The three curves correspond to the results expected when either alone of the $z = 1$ or $z = 3$ slices is used or the two surveys are combined. 24
- Figure 3-10:** The redshift-space correlation function at $\langle z \rangle = 0.8$, shown in false color to emphasize the Kaiser flattening at amplitudes $\xi = 0.1$. Note the ‘finger-of-God’ radial stretching that arises from virialized random motions at separations of a few Mpc. The superimposed contours show the best-fitting model of a Kaiser flattening plus this small-scale elongation. The first panel shows the VVDS measurements with 6000 galaxies (Guzzo et al. 2008); the second panel is a simulation of the results expected from a forthcoming new VLT survey of 100,000 redshifts. 28
- Figure 3-11:** The masses of the individual neutrino mass eigenstates, as constrained by neutrino oscillation experiments, plotted against the total neutrino mass for a normal hierarchy (solid lines) and an inverted hierarchy (dashed lines). Current cosmological data set an upper limit on the total mass of light neutrinos of around 0.6 eV 30
- Figure 3-12:** A potential improvement in the projected 2-parameter 68% C.L. errors in (w_0, w_a) subspace, expected for an extensive use of the WF MOS galaxy power spectrum. The outermost contour shows the forecast when the pure geometrical test of BAO experiment is used. The middle and innermost contours show the improvements when the growth rate information is included or the redshift distortion is further included. 33
- Figure 3-13:** Dark energy parameters for a WF MOS BAO survey with a HyperSuprimeCam (HSC) 3-D Weak Lensing survey and the Planck Surveyor CMB experiment. From top left to right and top to bottom are shown (i) HSC shear power and Planck CMB, (ii) HSC shear power and WF MOS BAO, (iii) HSC shear power and shear ratios, (iv) WF MOS BAO and Planck CMB, (v) HSC shear ratios and WF MOS BAO, (vi) shear ratios and Planck CMB. 35
- Figure 3-14:** Combining three independent experiments. Left to right: (i) Planck CMB, HSC shear power and shear ratios, (ii) WF MOS BAO, HSC shear power and shear ratios, (iii) WF MOS BAO, HSC shear power and Planck CMB, and (iv) WF MOS BAO, HSC shear power and Planck CMB. 36
- Figure 3-15:** The redshift distribution of DEEP2 galaxies derived via multicolor selection in BRI space (Coil et al. 2004). The cutoff at $z = 0.7$ results from the photometric preselection, whereas that at $z = 1.4$ reflects the red limit of DEEP2 spectroscopy. The two lines are alternative models for the selection function. 41
- Figure 3-16:** A plot of the growth factor $f_g(z) \equiv d \ln \delta / d \ln a$ against redshift for various models. The solid black line shows the standard $\Omega_m = 0.25$ Λ -dominated model, and the dashed black line shows the same expansion history but with the stronger DGP-style dependence of growth on $\Omega_m(a)$: $f_g(a) = \Omega_m(a)^{0.68}$. The blue dot-dashed line shows the DGP model itself (with $\Omega_m = 0.25$ today) and the red treble-dot-dashed line shows the behavior for a standard open $\Omega_m = 0.25$ model without dark energy. The three points at $z < 1$ are (in order of increasing z): 2dFGRS (E. Hawkins et al., 2003, MNRAS 346, 78); 2SLAQ LRGs (N. Ross et al., 2007, MNRAS 381, 573); VVDS (Guzzo et al. 2008). The points at higher redshift show the predicted performance from our proposed WF MOS surveys: 4×10^6 galaxies at redshift $z \sim 1$ and 10^5 LBGs at $z \sim 3$ (each split into two redshift bins). 44
- Figure 3-17:** Histograms of the equivalent width of [O II] 3737 emission line derived from DEEP2 galaxies in two different redshift bins. This indicates that an 80% redshift success rate will be achieved for the $z = 1$ survey provided a line of equivalent width as small as 20Å can be reliably detected. 46
- Figure 4-1:** The field of Streams from Belokurov et al. (2006) showing SDSS stars having $(g-r) < 0.4$ for a region around the North Galactic Cap. Colors denote depth along the line-of-sight with red being the most distant objects at $d \sim 50$ kpc and blue the nearest at $d \sim 10$ kpc. The right-hand panel shows a composite including the 2MASS M-giant distribution from Majewski et al. (2003). Several streams are readily visible. 50

Figure 4-2: The region around the $[OI]_{6300}$ line from a 5400s VLT-FLAMES exposure at $R=20,000$ of a metal-rich, $[Fe/H] = -0.41$ Bulge giant with $S:N \sim 200/A$. An unconstrained multi-component Gaussian model fit of the most prominent lines is shown overlaid in red.....	53
Figure 4-3: The INT/CFHT survey of the southern halo regions of M31; M33 can be seen in the lower left-hand corner of the image. The stellar haloes of M31 & M33 overlap and are replete with substructure (Ibata et al 2007).....	60
Figure 4-4: Dynamical predictions based upon a N-body simulation of a stellar bar and an axisymmetric bulge model. The comparison assists in determining the observing strategy necessary to distinguish different models for the Galactic bulge.....	66
Figure 4-5: The properties of a numerical simulation of the demise of the putative Canis Major dwarf galaxy and the resultant Monoceros Stream (Penarrubia et al. 2005).....	67
Figure 4-6: Distribution of debris from an inner halo satellite after 12 Gyr as a function of RA and Dec.	69
Figure 4-7: Aitoff projection of the proposed Primary Galactic Archaeology Survey.	73
Figure 4-8: The curve-of-growth of typical weak lines highlighting the critical dependence of the abundance determination on knowledge of the microturbulent velocity.....	74
Figure 4-9: Top panel: the upper portion presents the CaT region for a K-giant in the Sculptor dSph with derived $[Fe/H] = -1.50$ dex LR (-1.63 dex HR), showing an example of automated continuum fitting (dashed line). The lower portion presents the residual after continuum removal and after subtracting Gaussian model fits to the three CaT lines. Lower panel: the derived cross-correlation function and associated Gaussian fit around the peak region.	75
Figure 4-10: Example of automated continuum estimation and normalization using FLAMES benchmark HR test data.	79
Figure 4-11: The best fitting continuum-subtracted model spectra for solar and alpha-enhanced abundance ratios compared to an HR VLT-FLAMES $R=20000$ continuum-subtracted spectrum with $S:N \sim 100/A$. Upper panel: continuum-normalized data; lower panel: top is alpha-enhanced model spectrum (black); middle offset solar ratio model spectrum (green); the mask function used in the fit is in blue. The solar abundance ratio spectrum gives a marginally better fit.	82
Figure 4-12: Example of chemical tagging for the solar spectrum.....	83
Figure 5-1: Recovering the star formation timescale (τ) and metallicity Z for a red $l \sim 22$ $z \sim 0.7$ galaxy. The top panel refers to a low signal/noise spectrum such as that achieved for a dark energy survey of luminous red galaxies; the data is sufficient to secure the redshift but little more. The bottom panel refers to a much higher signal/noise spectrum such as would be possible with longer integrations on brighter objects ($R \sim 21$) over a wide area. In conjunction with an earlier survey by FMOS, it is proposed WF MOS could secure robust stellar properties for a large sample of bright galaxies over $0.7 < z < 1.6$	89
Figure 5-2: The spatial distribution Lyman alpha emitters in the well-studied SSA22 field (preliminary results from the ongoing survey, courtesy of Yamada et al). WF MOS, working in concert with HSC, would enable a huge increase in survey mapping speed and provide emission line statistics for yet larger samples.	90
Figure 5-3: Stacked Lyman alpha line profiles for emitters located from Suprime-Cam narrow band imaging (from the ongoing survey by Yamada and co-workers). Line widths and profile shapes constrain outflow models and the nature of the local intergalactic medium.....	91
Figure 5-4: Panoramic spectroscopy of clusters of galaxies at intermediate redshift (courtesy of Tanaka & Kodama and collaborators). The turn-around region for galaxies falling into a rich $z \sim 0.5$ cluster corresponds to a diameter of $\sim 15-20$ Mpc and fits neatly within a single WF MOS pointing. Detailed spectroscopy provides velocities and star formation diagnostics for thousands of members per cluster. This will enable a variety of studies which attempt to understand how the cluster environment both enhances and truncates star formation and rearranges the galaxy morphologies.	92
Figure 6-1: Sky coverage for DES (blue, 5000 deg^2), KIDS (red, 1500 deg^2) and CFHTLS-Wide (green, 150 deg^2). Pan-STARRS (omitted for clarity) will map 3π steradians seen from Hawaii. HSC coverage is not yet decided.	93

Figure 6-2: (Left): Photometric selection from the DEEP2 survey: red and blue points represent galaxies above and below a redshift of 0.7 respectively, based on BRI photometry alone. (Right): Simulation illustrating substantially improved photometric redshifts expected for the Dark Energy Survey (grizY filters) combined with the VISTA Hemisphere Survey (JHK filters). Deeper data such as that possible with HyperSuprimeCam would further improve the accuracy.	95
Figure 6-3: Neural network prediction of the [OII] equivalent width given BRI data used to pre-select DEEP2 galaxies. With more bands it will be possible to improve this performance.	97
Figure 6-4: (Left) Simulation of WF MOS spectra using realistic sky subtracted noise. We show as an example a galaxy at the high redshift end of the range for the $z \sim 1$ DE survey. (Right) Illustration of the significance needed in order to confirm that the line is indeed [OII].	98
Figure 6-5: Simulations of high redshift Lyman break galaxies in two different cases: via absorption lines (top) and via Lyman alpha emission (bottom). The absorption line detection requires a continuum signal to noise of four and the emission line detection requires a continuum signal to noise of one.	99
Figure 6-6: Example of automated LR sky subtraction from FLAMES benchmark test data.	102
Figure 6-7: An illustration of sky subtraction on a SDSS galaxy spectrum. The top panel is the observed spectrum from the SDSS archive, while the bottom panel is the 'clean' spectrum after sky subtraction with the PCA method. The second and third plots from the top show the 'sky' pixels and the reconstructed sky spectrum, respectively (from Wild & Hewett 2005).	103
Figure 6-9: Positioner allocation efficiency for the high-resolution spectrograph mode versus number of targets in the field. Shown are the efficiencies for ideal allocation (black), such as one might expect from a plug-plate allocation scheme, and the WF MOS high resolution spectrograph mode (green). The WF MOS efficiency is superior to that achieved by a system that selects a fixed subset of fibers to route to the high resolution spectrograph (in blue), as assumed in the FS. Shown in red is the fraction of astronomical targets successfully assigned to a fiber.	106
Figure 6-10: Signal to noise ratio (S/N) relative to peak S/N as function of fiber angular diameter, as measured in 0.72 arc sec seeing (i.e., close to the expected median seeing) with existing Subaru imaging data. Red points show curve-of-growth of flux for stellar objects. Green data points are S/N vs fiber diameter for bright stellar objects (i.e., negligible sky background), while black data points are for objects with similar mag to sky brightness per sq arcsec. Blue points show S/N for objects 3–4 mags fainter than sky.	107
Figure 6-11: The red curve shows a histogram of the completeness of our survey fields. We have assumed that 80% of the fields are observed once (which gives the leftmost bump in the red curve), and 20% of the fields with poor initial completeness are reobserved, yielding higher completeness (rightmost bump in red curve). Shown in blue is the tail of the distribution that would have remained if these 20% were not re-observed.	109
Figure 9-1: Use Case Diagrams Key	123
Figure 9-2: Use Cases for WF MOS Observation Preparation	124
Figure 9-3: Use Cases for WF MOS Observation Execution	126
Figure 9-4: Use Cases for WF MOS Engineering	127

List of Tables

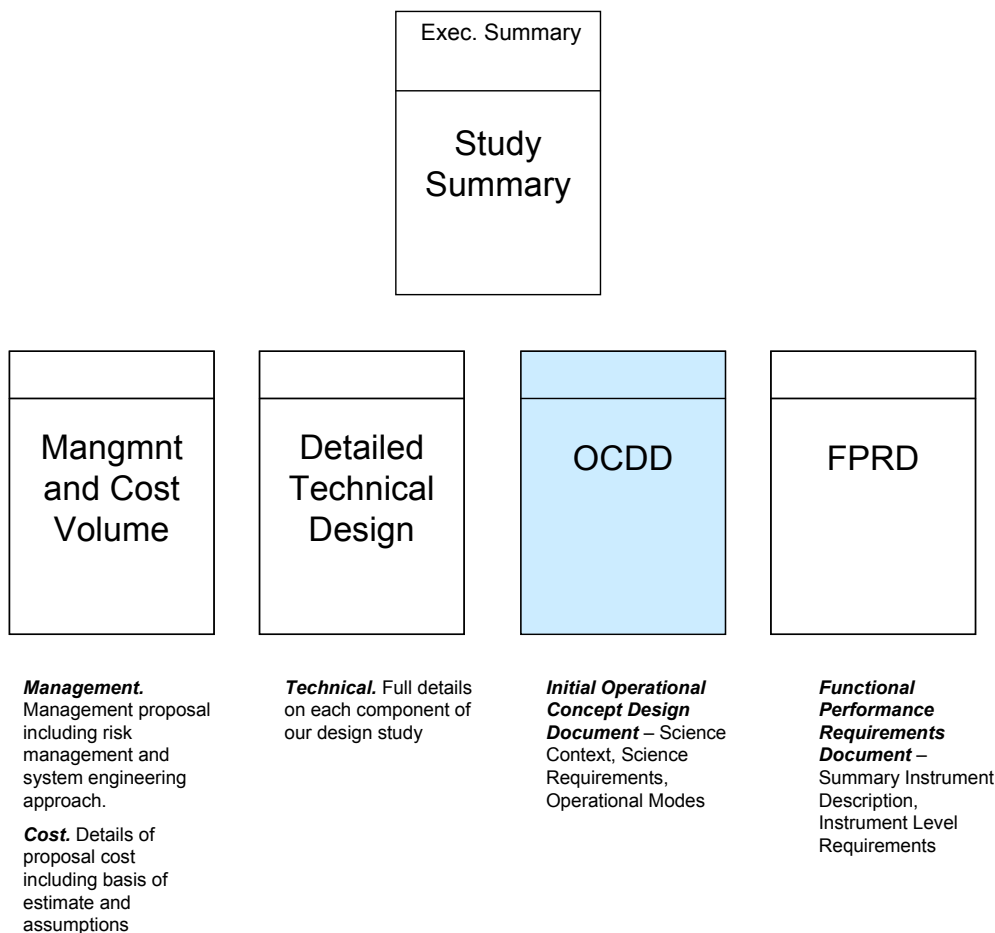
Table 3-1: DEEP2 Galaxy Number Counts	42
Table 4-1: FLAMES-GIRAFFE R=20000 EWs compared to UVES R=50000	54
Table 4-2: Summary of the Galactic Archaeology Requirements	55
Table 4-3: Summary of results of our analysis for block surveys	70
Table 4-4: Galactic Archaeology Spectroscopic Requirements Summary	78
Table 5-1: The Range of Survey Areas and Potential Applications	88
Table 6-1: Planned imaging surveys: AB magnitude limits per SDSS-like filter. Depths are taken from various survey websites. HSC depths follow a private communication (Takada)	94

Table 6-2. Estimated V-band stellar density (per square degree) as a function of galactic latitude and magnitude limit.....	106
Table 6-3: Number of fields required for low redshift dark energy survey. We adopt a two-tier strategy where most (80%) of fields are observed once. The 20% of fields with the worst completeness are re-observed, yielding higher average completeness with minimal additional survey time.....	108
Table 6-4: Required density of galaxies for the low redshift dark energy survey. The required surface density of successful redshifts is $1245/\text{deg}^2$. To achieve this density, we must start with a catalog of galaxies that reaches $R_{AB} = 23.0$	108
Table 6-5: Survey time requirements for the dark energy surveys.....	109
Table 6-6: Number of required fields for the high redshift dark energy survey.....	109
Table 6-7: Galactic Archaeology survey time requirements.	110

Organization of Documents

The **Study Summary** summarizes the concept study and includes an overview of the scientific motivation and survey strategy (section 2), an instrument overview (sections 3–5), operations description (section 6), and the management and system engineering approach including total cost (section 7). The **Management and Cost Volume** provides project organization, cost and schedule estimates, management techniques, and contract structure. The **Detailed Technical Design** document is a detailed description of the instrument that supplements the instrument description in the Study Summary. The **Operation Concept and Design Document** presents detailed scientific context, science requirements, and operational mode and the Level 1 requirements. The **Functional/Performance Requirements Document** lists the instrument Level 2 and Level 3 requirements.

The following diagram shows an outline of the document tree with the current document shaded in blue.



1 INTRODUCTION

1.1 Purpose of Document

The purpose of the Operational Concept Design Document (OCDD) is to provide a vital insight into how the Wide Field Fiber-Fed Multi-Object Spectrometer (WF MOS) will be deployed and used. The document has two aims:

1. The scientific motivation and context leading to a full statement of the science requirements
2. A description of the instrument and its operational modes

The first aim of the document will be used as a key input into the derivation of sub-system requirements and any subsequent design trade-offs. The second will evolve during the concept design and implementation phases to finally become the instrument's Operational Manual. The full complement of instrument requirements as derived from the science requirements and other programmatic requirements will not be described here, but is documented in the associated Functional Performance Requirements Document (FPRD). Although it is undesirable to repeat information contained in both documents, for clarity the science requirements are summarized in Section 7 followed by a description of the initial instrument concept design.

1.2 Background

The Gemini Observatory initiated the "Aspen Process" to define science missions for their second-generation instrumentation. Through that process, the initial requirements for a Wide-Field Multi-Object Spectrometer (WF MOS) were identified. In the period to 2005, a consortium led by the Anglo-Australian Observatory prepared a Feasibility Study (FS) of such an instrument. Gemini, Subaru, and the Gemini board concluded that WF MOS should be installed on the Subaru telescope where it could share the optics destined for the proposed prime focus Camera, HyperSuprimeCam (HSC). The Gemini Project's Instrument procurement process stipulates the preference for a competitive Conceptual Design Study to confirm the technical and financial viability of the chosen Instrument and to allow the project to choose a team to complete the Design and Build Phase.

WF MOS represents an ambitious venture for the Gemini partners. The design and eventual construction of this instrument is motivated by the need to address several outstanding questions in cosmology and Galactic history through comprehensive spectroscopic surveys of galaxies in various redshift ranges and stellar abundance and dynamical studies in the Galactic disk and halo.

The rationale for an in-depth independent study of WF MOS is manifold. Foremost, the scope of the extragalactic and Galactic surveys necessary to deliver breakthrough science results needs serious updating and rebalancing. For the cosmological applications, the situation has developed significantly since 2005. A number of new experiments are now funded or proposed for the study of dark energy and it is critical to better understand the unique role that WF MOS might play. The science return in the Galactic

component needs to be more quantitatively developed in the context of surveys with a broader range of options. Conceivably, more modest, strategically engineered surveys can be as effective as the very ambitious ones proposed in the Feasibility Study. Additionally, the survey design should take into account constraints provided from other facilities, particularly those defining the HSC imaging campaign that can generate spectroscopic targets and utilize weak gravitational lensing in a complementary manner to constrain dark energy. All of the above leads to a new set of science requirements with consequent impact on the instrument design and operation.

Although the Aspen process and the subsequent WF MOS Feasibility Study focused on implementing two large surveys (dark energy and galactic archaeology), it is clear that a panoramic multi-object spectrograph such as WF MOS also has the potential for significant discoveries over a much broader area of astronomy. Earlier equivalent survey spectrographs, the 2-degree field facility and the Sloan Digital Sky Survey, have readily demonstrated that such carefully planned facilities have an impact far beyond the science goals which originally motivated their funding and construction.

Our team's participation in two successive conferences involving substantial attendance from the Japanese community—*Panoramic Views of Galaxy Formation and Evolution* (Hayama, Japan, December 2007) and *Cosmology Near and Far – Science with WF MOS* (Kona, HI, May 2008)—has brought this point into sharp focus. Japanese astronomers (and Japanese members of our team) see WF MOS as a facility whose impact is likely to extend well beyond that originally envisaged by the Aspen vision. Accordingly, we have gathered Japanese input on this topic and herein examine, to the extent possible, whether our design (driven solely by the cosmological and Galactic surveys) is compliant with other applications of interest to the Japanese community. This will, we believe, lead to an improvement in Japanese support for WF MOS on Subaru.

1.3 Instrument Identification

The instrument described in this OCDD shall be identified as WF MOS, a Wide-Field, Fiber-Fed Multi-Object Spectrograph designed to allow both Dark Energy and Galactic Archaeology observations as identified and described in the WF MOS Science Case.

1.4 Document Layout

In this section we define the purpose of the OCDD, provide some background information about the project and identify the product. The detailed science cases with justify the surveys are presented in Sections 3, 4, and 5. Although these are self-contained proposals, more detailed technical descriptions of the associated target imaging, exposure times, fiber assignment efficiencies and data extraction are collated in Section 6. Section 7 summarizes the requirements, Section 8 gives an overview of the instrument by subsystem, and Section 9 describes the use cases and modes of the instrument. The primary operational scenarios are identified and detailed with an emphasis on how WF MOS interfaces with the Subaru telescope.

2 DOCUMENTS

2.1 Applicable Documents

Document Title	Issue	Date
WF MOS Feasibility Study Report	1.0	07/03/05
WF MOS Feasibility Study Operational Concept Definition Document	1.0	06/24/05
WF MOS Conceptual Design Study RFP		2007 May 08
Draft Initial OCDD	1.0	2008 Sept 19

3 WFMOS, DARK ENERGY, AND MODIFIED GRAVITY

3.1 The Challenge of Cosmic Acceleration

The most radical conclusion of cosmological research in the late 20th Century was that the expansion of the universe has not decelerated as expected from the gravitational effect of the matter it contains. The most direct evidence for this statement emerged from studies of SNe Ia treated as standard candles (Riess et al. 1998; Perlmutter et al. 1999), although studies of standard rulers in structure formation had yielded the same conclusion somewhat earlier (Efstathiou, Sutherland & Maddox 1990). The initial reaction to these observations has been to assume that the universe contains a cosmological constant, Λ , and this is a natural path to follow given that Λ has been a potential feature of cosmological models from the start of the subject. With this addition, the Λ plus cold dark matter (Λ CDM) model of structure formation accounts extremely well for a range of data, and has survived the astonishing advances in Cosmic Microwave Background (CMB) data from the *Wilkinson Microwave Anisotropy Probe* (WMAP) and other experiments (e.g., Spergel et al. 2003; 2006; Komatsu et al. 2008).

Nevertheless, this is not a satisfactory state of affairs. Following Zeldovich, modern practice is to place the term Λ on the right hand side of Einstein's field equations and to interpret it as the energy density of the vacuum. Discovering the physical origin of such a density is challenging because the value is extremely small compared to any natural particle physics scale. As a result, the term 'dark energy' is often used to encapsulate our ignorance of the detailed physics that is being probed.

Alternatively, it is possible that the phenomenon of dark energy is entirely illusory. The necessity for this constituent arises from using the Friedmann equation to describe the evolution of the cosmic expansion; if this equation is incorrect, it would require the replacement of Einstein's relativistic theory of gravity with some new alternative. Either of these alternatives offers an exciting door to new possibilities in physics, and current cosmological research is absorbed with exploring techniques that can play a decisive role.

3.1.1 Dark Energy Observables

Dark Energy can differ from a classical cosmological constant in being a dynamical phenomenon. Empirically, this means that it is endowed with two thermodynamic properties that astronomers can try to measure: the bulk equation of state and the sound speed. If the sound speed is close to the speed of light, the effect of this property is confined to very large scales, and mainly manifests itself in the large-angle multipoles of the CMB anisotropies (DeDeo, Caldwell & Steinhardt 2003). The equation of state, however, is more readily probed. This is quantified via the *equation of state* parameter $w \equiv P / \rho c^2$, which can in principle be an evolving function of scale factor, $w(a)$.

For adiabatic expansion, we should in general regard $-3(w+1)$ as giving the logarithmic rate of change of the dark-energy density, $d \ln \rho / d \ln a$, so the Friedmann equation gives the epoch-dependent Hubble parameter as

$$H^2(a) = H_0^2 \left[\Omega_v e^{\int -3(w(a)+1) d \ln a} + \Omega_m a^{-3} + \Omega_r a^{-4} - (\Omega - 1) a^{-2} \right], \quad (1)$$

where $a = 1/(1+z)$ is the dimensionless scale factor. This change in expansion rate is observable in two ways: via the geometry of the universe and via the growth of density perturbations.

The comoving distance-redshift relation is one of the chief diagnostics of w . The general definition of comoving distance $D(z)$ is

$$D(z) = R_0 S_k(r), \text{ where } R_0 dr / dz = c / H(z) \text{ and } R_0 = |1 - \Omega_{total}|^{-1/2} c / H_0, \quad (2)$$

and the function $S_k(r)$ is sin or sinh depending on whether the universe is positively or negatively curved. Any standard length in the universe, such as those defined by the pattern of large-scale structure, thus subtends an angle involving $D(z)$ if seen transverse to the line of sight, or a redshift increment involving $H(z)$ if seen radially. In detail, these aspects can be separated, although it is frequently convenient to introduce $D_V(z) = [D(z)^2 (c / H(z))]^{1/3}$ (Eisenstein et al. 2005) to approximate what is measured if we have datasets that average over radial and transverse orientations.

Density fluctuations $\delta = \delta\rho / \rho$ (denoting the fractional density perturbation) grow as a function of scale factor as $\delta(a) \propto a$ at early times, while the universe is matter dominated and curvature can be neglected. But when dark energy becomes important at late times, this growth is reduced, in a way that depends on the amount of dark energy, and also on its equation of state. We incorporate this into a growth suppression factor, $\delta(a) \propto g(a)a$, where $g(a)$ carries the information about the dark sector. As we will show, $g(a)$ can be probed in a number of ways, either by estimating the mass fluctuations directly, or by measuring the peculiar velocities associated with their growth. The principal tools for achieving this are galaxy clustering and 3-D Weak Lensing; both of these are fields where data from WF MOS can have a major impact.

The three key quantities H , D & g are all sensitive to dark energy, but how strongly? Figure 3-1 shows what happens when we perturb these quantities about a fiducial $\Omega_m = 0.25$, $w = -1$ model. In general, the observables respond rather slowly to changes in w . showing a sensitivity multiplier of about 5 (e.g., Peacock et al. 2006), so that a measurement of w to 1% precision requires knowing D to 0.2%. Furthermore, there is substantial degeneracy with Ω_m , so that the matter density has to be known well in order to detect the redshift-dependent effect of a change in w on any of the observables. But the good news is that the degree of degeneracy is different for different observables, especially the growth rate. There is therefore a good prospect for attaining a robust measurement of the equation of state of dark energy if all the observable signatures can be accessed.

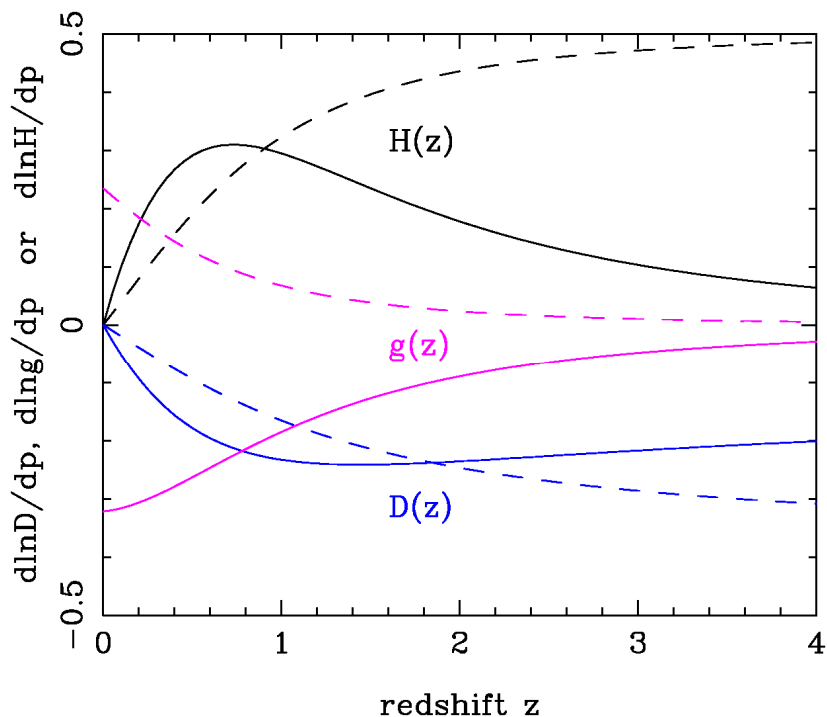


Figure 3-1: Perturbation around $\Omega_m = 0.25$ and $w = -1$ of the dependence on redshift of the Hubble parameter H , the distance D and density growth factor g . The parameter p refers to either w or $\ln \Omega_m$; solid lines shows the effect of an increase in w , dashed lines the effect of an increase in Ω_m .

3.1.2 The Evolution of Dark Energy

Early studies of dark energy tended to treat w as a constant, but physical models for dark energy tend to be dynamical, so the equation of state is almost certain to evolve. Given the lack of a unique model, the simplest non-trivial parameterization is (Chevallier & Polarski 2001; Linder 2003);

$$w(a) = w_0 + w_a(1 - a). \quad (3)$$

When the evolving $w(a) = w_0 + w_a(1 - a)$ model is matched to data, typically a strong correlation is seen between the inferred values of w_0 and w_a . This correlation is readily understandable: the bulk of the sensitivity comes from data at non-zero redshifts, so the $z = 0$ value is an unobserved extrapolation. It is better to assume that we are observing the value at some intermediate *pivot redshift*:

$$w(a) = w_{\text{pivot}} + w_a(a_{\text{pivot}} - a). \quad (4)$$

The pivot redshift is defined so that w_{pivot} and w_a are uncorrelated; in effect rotating the goodness of fit contours on the $w_0 - w_a$ plane. If we do not want to assume the linear model for $w(a)$, a more general approach is given by Simpson & Bridle (2006), who express the effective value of w (treated as constant) as an average over its redshift dependence, with some redshift-dependent weight. Both these weights and

the simple pivot redshifts depend on the choice of some fiducial model. With reasonable justification (both from existing data, and also because it is the fiducial model that we seek to disprove), this is generally taken to be the cosmological constant case.

As will be seen below, the pivot redshift for most experiments tends to be close to $z = 0.6$, reflecting the fact that (a) w manifests itself in an integrated signal that builds up from $z = 0$; (b) if dark energy is close to Λ in its behavior, the contribution becomes subdominant and hard to measure for $z \geq 1$. Thus, a first order view of the situation is that different experiments will measure $w(z = 0.6)$ and an uncorrelated estimate of how rapidly it evolves at that time, w_a . The Albrecht et al. (2006) US Dark Energy Task Force (DETF) advocated a *figure of merit*, which is the reciprocal product of these two uncertainties, i.e., reciprocal of the area of the error ellipse in the $w_0 - w_a$ plane. However, it is not clear that this is the best choice: as long as Λ matches the data, the initial challenge is to rule out this $w = -1$ model, so there could be a case for trying to optimize the accuracy of measuring w_{pivot} , independent of evolution. But one could also envisage models that have $w_{\text{pivot}} = -1$ and yet show $w_a \neq 0$; it really depends on one's prejudice on how realistic models might occupy the $w_0 - w_a$ plane. In practice, the axial ratio of the confidence ellipse is large, so that errors in w_a are around 10 times those in w_{pivot} . Thus, if plausible models occupy a small region near $(w_0, w_a) = (-1, 0)$, they are much more likely to be detected via their effect on w_{pivot} than via w_a .

But adopting the assumption that Λ will eventually be rejected, measuring evolution would then be the next goal. For this reason, steps have already been taken to go beyond the simple figure of merit, and the Figure of Merit Science Working Group (FoMSWG) has produced a more elaborate proposal (Albrecht et al. 2009). This concentrates on how many independent modes in $w(a)$ a given experiment can measure, and is certainly an attractive approach once we are sure that a cosmological constant is rejected.

3.1.3 Modified Gravity

Current inferences concerning the presence of dark energy rest on the assumption of the Friedmann equation, based on Einstein's gravitational field equations. Independent of this, there has been growing emphasis in the community on the idea of testing Einstein's General Relativity. In fact, we have little idea how to approach cosmology without retaining much of the structure of the standard relativistic treatment. Thus, there is still a metric, within which scalar-mode perturbations can be described in terms of two potentials:

$$d\tau^2 = (1 + \Phi)^2 dt^2 + (1 - \Psi)^2 d\sigma^2 \quad (5)$$

Here, τ is proper time, t is cosmological time and $d\sigma^2$ is the spatial part of the metric; this must still be of the standard Robertson–Walker form, since this is dictated only by symmetry. Observational cosmology survives unchanged, since photon trajectories are still null. The redshift is still such that $1 + z$

gives the factor by which the universe has expanded since the light we now see was emitted, and the normal relation between comoving distance and redshift still applies: $D(z) = \int cdz / H(z)$

This exact degeneracy between dark energy and modified gravity is broken when we consider a perturbed universe and look at the relation between matter and the potentials. This is simplified in Einstein gravity because the potentials Φ and Ψ are both equal to the Newtonian potential, which satisfies the Poisson equation (when nonrelativistic matter dominates). As a result, the growth law for fractional density fluctuations is rather simple, and can be represented accurately by Peebles' approximation for the logarithmic growth rate: $f_g(a) \equiv d \ln \delta / d \ln a \approx \Omega_m(a)^{0.55}$. Linder (2005) suggested that a similar representation might capture the main behavior in modified gravity models:

$$f_g(a) \equiv \frac{d \ln \delta}{d \ln a} \approx \Omega_m(a)^\gamma. \quad (6)$$

In Einstein gravity, the approximation $\gamma = 0.55 + 0.05[1 + w(z=1)]$ works very well, so the growth rate is roughly universal for a given expansion history in conventional gravity theories. But for modified gravity, this need not be so: the number γ emerges as an important additional parameter in testing the consistency of the standard framework.

Within this framework, the freedom to depart from Einstein gravity lies in the relation between matter and spacetime curvature. This is described by the field equations that result from adding a gravitational action to the matter action, and the Einstein–Hilbert action is as simple as possible: proportional to the Ricci scalar R . A natural line of attack is then to replace this by something more complicated: e.g., $R \rightarrow R + f(R)$, where $f(R)$ is some function that becomes negligible at large R so that local tests of gravity are not affected (Hu & Sawicki 2007). There is enough freedom in this framework to account for any expansion history of the universe without dark energy, simply by choosing an appropriate $f(R)$. This means that there is a modified Friedmann equation; it contains familiar elements such as the density parameter, since $H(z)$ and $\rho(z)$ still define a density parameter in the usual way, but now $\Omega = 1$ is no longer required in order for the universe to be flat.

The most interesting possibilities of this sort to emerge from recent work are modifications motivated by the predictions from string theory of the existence of higher dimensions. The hidden scale associated with these dimensions allows a scale dependence of the strength of gravity, which can mimic cosmic acceleration. For example, in the DGP model (Dvali, Gabadadze & Porrati 2000), we have the relation

$$H^2(z) = H_0^2 \left(\frac{1 - \Omega_m}{2} + \sqrt{\left(\frac{1 - \Omega_m}{2} \right)^2 + \Omega_m a^{-3}} \right)^2 \quad (7)$$

(neglecting radiation), so that the universe tends to a de Sitter model with constant H even without an explicit vacuum energy. This model provides a direct demonstration that an accelerating universe need

not require the existence of a physical dark-energy component. The growth of perturbations in the DGP model can be accurately described by Linder's model with $\gamma \approx 0.68$; this is almost 25% larger than the value in a Λ -dominated universe, and we show below that relatively modest surveys using WF MOS would be capable of detecting this difference. The specific DGP model is probably already ruled out using supernova data (e.g., Sawicki & Carroll 2005; Fairbairn & Goobar 2006); but it has played an important role in persuading the community that the density growth rate should be treated as a key cosmological diagnostic.

A key requirement arising from our study is the need for WF MOS to address more advanced models of this general type. *Specifically we wish to both improve our understanding of dark energy along the conventional route of measuring w and its possible evolution, as well as to test whether dark energy might arise from inadequacies in General Relativity.*

3.2 Baryon Acoustic Oscillations

3.2.1 Standard Rulers

The geometrical effect of dark energy can be observed because the pattern of density inhomogeneities in the universe contains preferred lengths. These are related to the horizon lengths at certain key times, i.e., to the distance over which causal influences can propagate. There are two main lengths of interest: the particle horizon at matter-radiation equality (D_{EQ}) and the acoustic horizon at last scattering (D_{LS}). The former governs the general break scale in the matter power spectrum, and the latter determines the *Baryon Acoustic Oscillations* (BAO) by which the power is modulated:

$$\begin{aligned} D_{EQ} &\approx 123(\Omega_m h^2 / 0.13)^{-1} \text{ Mpc}, \\ D_{LS} &\approx 147(\Omega_m h^2 / 0.13)^{-0.25} (\Omega_b h^2 / 0.023)^{-0.08} \text{ Mpc}. \end{aligned} \quad (8)$$

Note that the acoustic horizon is smaller than the particle horizon, since it depends on the speed of sound, which is at most $c_s = c/\sqrt{3}$, and in practice somewhat less owing to the inertia of the baryonic component. These scales can be seen projected on the sky via the CMB power spectrum, and also in the matter power spectrum (see Figure 3-2). Following the important WMAP results, the detailed shape of the CMB power spectrum breaks the degeneracies implicit in the above scaling formulae, so that the individual parameters and thus the key horizon lengths are known virtually exactly. Datasets at lower redshifts probe the same parameters in a different way, which also depends on the assumed value of w : either directly from $D(z)$ as in SNe, or via the horizon scales as in LSS. Consistency is only obtained for a range of values of w , and the full CMB+LSS+SNe combination already yields impressive accuracy (e.g., Spergel et al. 2006):

$$w = -0.926^{+0.051}_{-0.075} \quad (9)$$

(for a spatially flat model). The confidence contours are plotted in detail in Figure 3-3. Any future experiment must aim for a substantial improvement on this baseline figure.

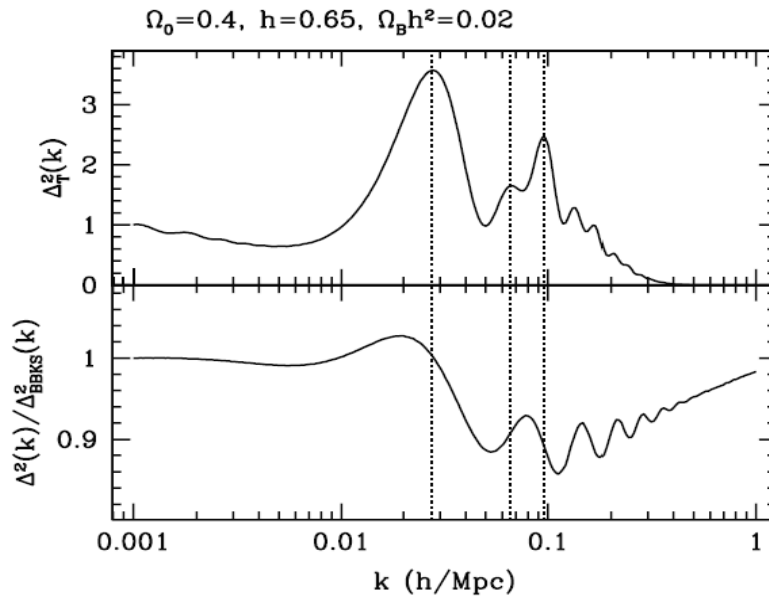


Figure 3-2: Acoustic oscillations in the radiation-baryon fluid imprint a pattern in the Fourier spectrum of both CMB (top) and density (bottom) fluctuations (e.g., Meiksin, White & Peacock 1999). In the latter case the effect is much smaller, because the dominant dark matter has no intrinsic oscillations. Nevertheless, the same acoustic scale can be picked out at low and high redshift, opening the way to a relatively clean geometrical tool in cosmology

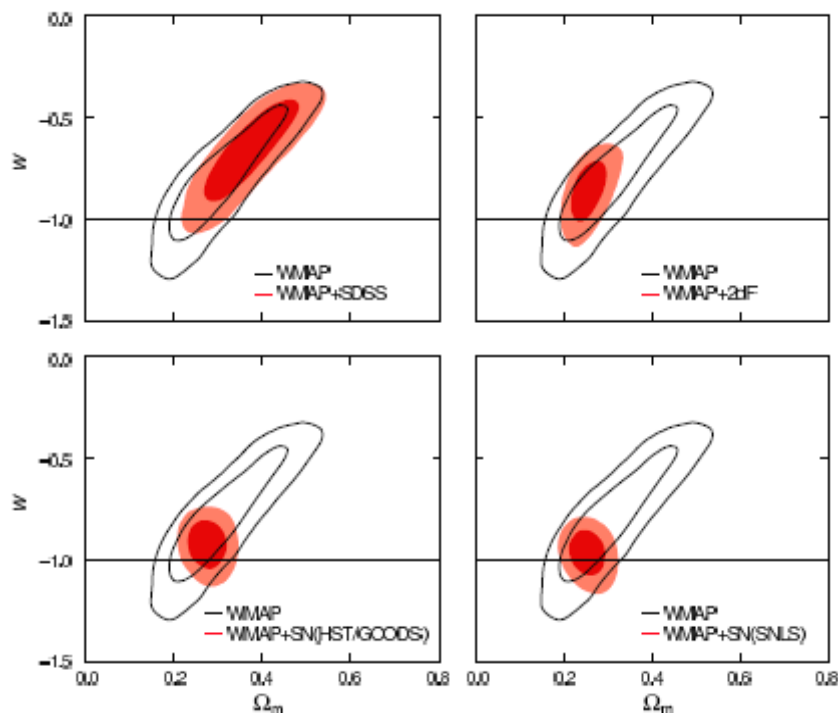


Figure 3-3: Confidence contours on the plane of w versus Ω_m from the WMAP year-3 data (Spergel et al. 2006). It is assumed that w does not evolve, and also that the universe is spatially flat, although this latter assumption is not critical.

3.2.2 Precision of BAO Measurement

One of the main recommendations of the Feasibility Study was the use of the BAO signature as a standard ruler in order to measure w based on two ambitious surveys undertaken at redshifts $z = 1$ and $z = 3$. This strategy has already been extensively discussed in the literature (e.g., Blake & Glazebrook 2003; Glazebrook & Blake 2005; Seo & Eisenstein 2003; 2005; 2007). Here we summarise the main factors that govern the precision of such a cosmological experiment.

The limitation on an experiment of this sort is simply the fractional error in the galaxy power spectrum, $P(k)$, which depends on the number density of galaxies, n , and the range of wavenumber, k , as follows:

$$\sigma_{\ln P} = \frac{2\pi}{(Vk^2 \Delta k)^{1/2}} \left(\frac{1+nP}{nP} \right) \quad (10)$$

(Feldman, Kaiser & Peacock 1994). Provided nP is greater than of order unity, this represents largely a cosmic (or sample)-variance limited measurement. At the wavenumber of the main acoustic feature the observed galaxy power spectrum displays rather little evolution. We adopt a canonical power value of $P \simeq 2500(h^{-1}\text{Mpc})^3$ at wavenumber $k = 0.1h\text{Mpc}^{-1}$, motivated by a correlation function scale-length of

$2.5 h^{-1}$ Mpc and slope $\gamma = 1.9$ as measured by the VVDS survey (Meneux et al. 2006; Guzzo et al. 2008). Rather similar parameters apply for $z = 3$ Lyman-break galaxies (e.g., Hildebrandt et al. 2005).

Assuming that there are more targets than fibers, the volume covered in a fixed time scales as $1/n$, so that the overall power error is minimized at $nP = 1$ (Kaiser 1986). For the canonical power, this suggests a target density of $n = 4 \times 10^{-4} h^3 \text{Mpc}^{-3}$ to $nP = 1$. This can be reduced somewhat with only moderate penalty, and an absolute minimum figure is perhaps as low as $n = 10^{-4} h^3 \text{Mpc}^{-3}$, at which point the error is 25% larger than in the optimal case. Because of the asymmetric nature of the S/N function, only a small penalty is paid for exceeding the optimum density compared to the relatively abrupt dominance of shot noise if the density is too low. The noise penalty as a function of galaxy density is shown in Figure 3-4. As a result of these considerations, we shall generally adopt a slightly more conservatively high target density:

$$\text{Maximum target density} = 0.001 h^3 \text{Mpc}^{-3} \quad (11)$$

although bearing in mind that this can be reduced by up to a factor 2 at relatively little cost in S/N . Using these concepts, we can develop the following useful rule of thumb for the accuracy with which $D(z)$ can be measured by picking out the acoustic scale:

$$\% \text{ error in } D(z) = (V/5 h^{-3} \text{Gpc})^{-1/2} (k_{\text{max}}/0.2 h \text{Mpc}^{-1})^{-1/2} \quad (12)$$

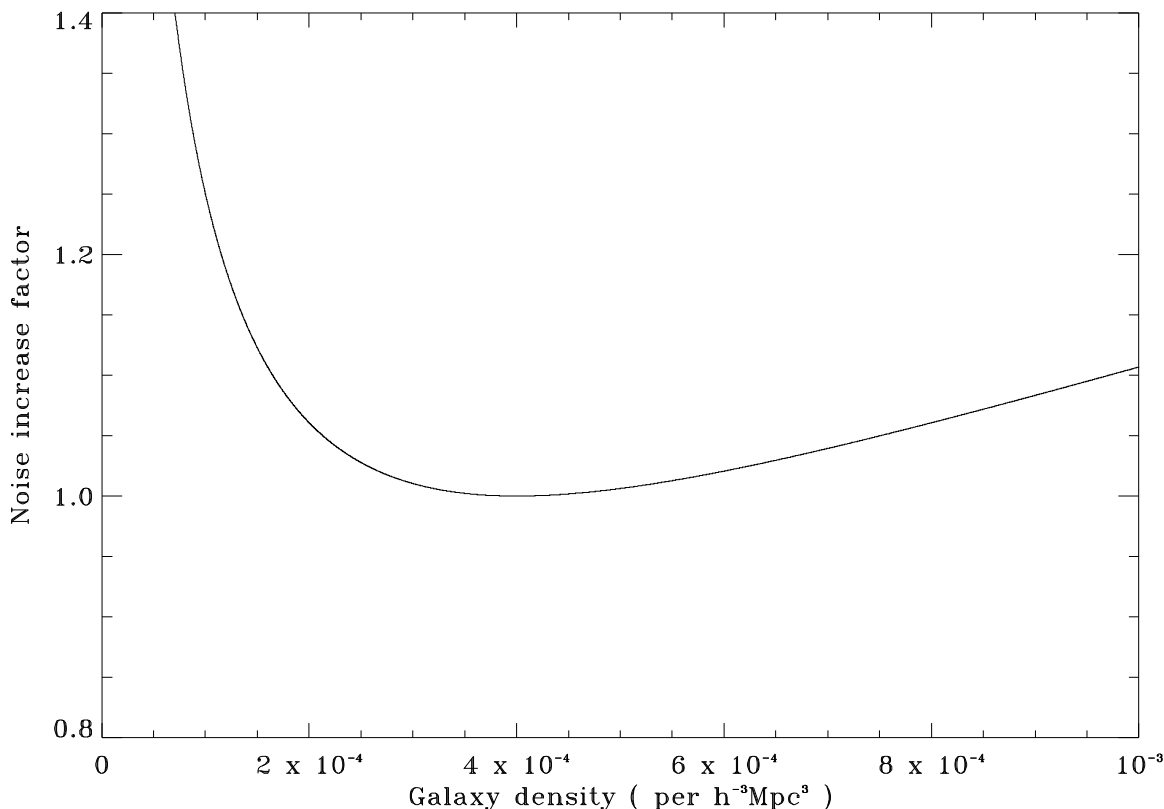


Figure 3-4: Increase in the power spectrum noise as a function of survey galaxy density. For a canonical value of the power spectrum of $2500 (h^{-1} \text{Mpc})^3$, and assuming more targets than fibers, a target density of $4 \times 10^{-4} h^3 \text{Mpc}^{-3}$ optimizes survey efficiency. At lower densities, shot noise dominates the error on the power spectrum. Higher target density produces somewhat improved estimates, but such surveys are less efficient, leading to an overall noise increase if the survey is constrained to fixed total time.

Here, we have supplemented the obvious scalings with depth and k -space volume with a detailed practical calculation of magnitude of the precision, as discussed in section 3.3.

We can consider this formula in the context of the two baseline surveys suggested by the Feasibility Study, at $z \sim 1$ and $z \sim 3$ and later we will recommend significantly different survey areas. In practice, our proposal will increase the redshift bounds of the $z \sim 1$ survey to exploit new-generation red-sensitive CCDs:

$$\begin{aligned} 0.7 < z < 1.6: A_1 &= 322 \text{ deg}^2 \\ 2.5 < z < 3.3: A_1 &= 254 \text{ deg}^2 \end{aligned} \tag{13}$$

where A_1 is the area required for a $1 (h^{-1} \text{Gpc})^3$ volume in these redshift bands. Bearing in mind the precision multiplier factor of 5, we see that a useful advance in precision on w compared to the current roughly 6% measurement requires a volume in excess of $5 (h^{-1} \text{Gpc})^3$, or areas of 1610 and 1270 deg^2 at

$z \sim 1$ and $z \sim 3$ respectively. At our minimum density of $n = 10^{-4} h^3 \text{ Mpc}^{-3}$, this requires 500,000 galaxies, rising to 2,000,000 at the optimal density with $nP = 1$.

One point that requires care is that the expression given earlier for the fractional error on the power assumes that the galaxy number density is a constant. In reality, no observational technique will assure this. At $z = 1$, we will be interested in flux-limited catalogues with depths similar to that of the DEEP2 survey (e.g., Coil et al. 2004), where the number density falls exponentially at high z , declining by at least a factor of 10 between $z = 0.7$ and $z = 1.6$. Similarly, for Lyman-Break galaxies, the standard color selection is most efficient at $z = 3$, and the redshift histogram tends to be approximately Gaussian with a FWHM in redshift of about 0.6. To see how this affects things, consider the full expression for the error on $P(k)$, assuming that galaxies are given the optimal weight $w = 1/(1 + nP)$ (Feldman, Kaiser & Peacock 1994):

$$\sigma_{\ln P} = \frac{(2\pi)^{3/2} / V_k^{1/2}}{\left(\int \frac{(nP)^2}{(1+nP)^2} dV \right)^{1/2}}, \quad (14)$$

where V_k is the volume in k space considered. We have computed this exact expression, setting the mean number density over the redshift band to be the optimal value, i.e., $\langle n \rangle = 1/P$. In practice, the fractional power error is within a few % of what would be predicted for a constant density at this level. Therefore, accurate predictions of surface densities of targets can be made using the simple constant-density error formula.

One critical issue to be faced when measuring cosmological parameters with the galaxy power spectrum is whether to use the full information available in the power spectrum, including the horizon-scale break, or whether to concentrate on the BAO signal alone. As with current CMB data, use of the full spectrum places greater weight on the correctness of the CDM model, whereas the relatively compact BAO signature can be used to pick out as an empirical length scale in a model-independent way (as done in the state-of-the-art BAO analysis of Percival et al. 2007). The full approach can increase the figure of merit by a factor 3 to 5, but we will generally take the more conservative approach of using only the robust BAO effect.

Finally we mention a recent analysis by MacDonald & Seljak (2008) which shows that the cosmic variance limit assumed here is not always the ultimate constraint in studies of galaxy clustering, because there can be multiple galaxy types that trace the underlying density field in different ways. This insight does not appear to have any impact on BAO measurement, but it does influence redshift-space distortions, as we discuss below.

3.2.3 *Non-linear Effects on BAOs*

As with any high-precision statistical experiment, we need to be sure that the value of small $1/N^{1/2}$ is not dissipated by errors from systematics. Since we aim to locate the BAO scale to a fraction of 1%, we need to understand distortions in the power spectrum at this level. Such distortions do exist on the scales of interest. At the simplest level, the matter power spectrum has a non-negligible degree of nonlinearity at the scale of the principal acoustic peak ($k = 0.07h \text{ Mpc}^{-1}$), where the power is suppressed by around 20%. Such overall matter nonlinearities inevitably lead to shifts in the scale of spectral features. This can be seen intuitively via the Zeldovich approximation, in which we think of the growth of structure not simply as a linear increase in density, but as an actual collapse that transfers power from one scale to another. In quantitative detail, this can be simulated readily—at least, in the case of dark matter only. The following plots (Lynn & Peacock, in preparation) show the effect of varying the main parameters that govern the power spectrum: the zero-redshift normalization (σ_8), the shape parameter ($\Omega_m h$) and the baryon fraction, (Ω_b / Ω_m). We show both the variation in power spectra in single simulations, and also the shift in the location of the principal acoustic peak averaged over a number of simulations.

The plots in Figures 3-5 and 3-6 show that the acoustic scale can shift by several percent from its ideal linear-theory location—and moreover that the amount of the shift depends on the details of the model. In principle, this is a concern: recall that we need to be able to predict the scale location to a small fraction of 1%. However, given the increasing precision on the ancillary parameters delivered by WMAP (and soon Planck), we consider this not to be an issue.

These nonlinear modifications of the intrinsic acoustic scale can be looked at in a different way, as proposed by Eisenstein et al. (2007). In configuration space, the effect of interest is the alteration of the separation of pairs of galaxies separated by the acoustic scale of around 150 Mpc, compared to their location according to linear theory. Eisenstein et al. argue that this can be understood as a convolution by the displacement field. Furthermore, since this is an effect arising from relatively large-scale modes (similar to peculiar velocities), it can at least in part be predicted from the map of the density field and removed. This ‘acoustic peak reconstruction’ has the potential to make the S/N of the BAO measurement closer to the simple predictions of linear theory, which are what we have presented in earlier sections. How much difference this makes depends on how far into the nonlinear regime the analysis is pushed. This can be controlled more easily in Fourier space, where a number of acoustic harmonics are accessible, whereas these combine in configuration space to yield a single peak at ~ 150 Mpc separation in the correlation function. At redshifts of a few tenths, the principal acoustic peak at $k = 0.06 h \text{ Mpc}^{-1}$ is slightly affected, but the acoustic signal in higher harmonics is largely erased by $k = 0.2 h \text{ Mpc}^{-1}$. Eisenstein et al. (2007) argue that this effect can be largely undone by predicting the displacement field from our map of large-scale structure, and correcting the galaxy positions. The claim is that a loss of a factor 4 in S/N can certainly be reduced to a factor 2, and possibly eliminated altogether.

Such issues are less important for the WF MOS projects, for two reasons. First, we will work at higher redshifts than in the study of Eisenstein et al. (2007). The rms displacement field amplitude should scale accurately with linear-theory growth, thus being down by a factor 0.75 at $z = 1$ and 0.56 at $z = 3$. This increases the maximum wavenumber at which the acoustic signal survives. Also, as we now explain, a wavenumber of $k = 0.2 \text{ hMpc}^{-1}$ is in any case dangerously high for other reasons. In short, we do not feel the successful application of acoustic peak reconstruction is a critical issue.

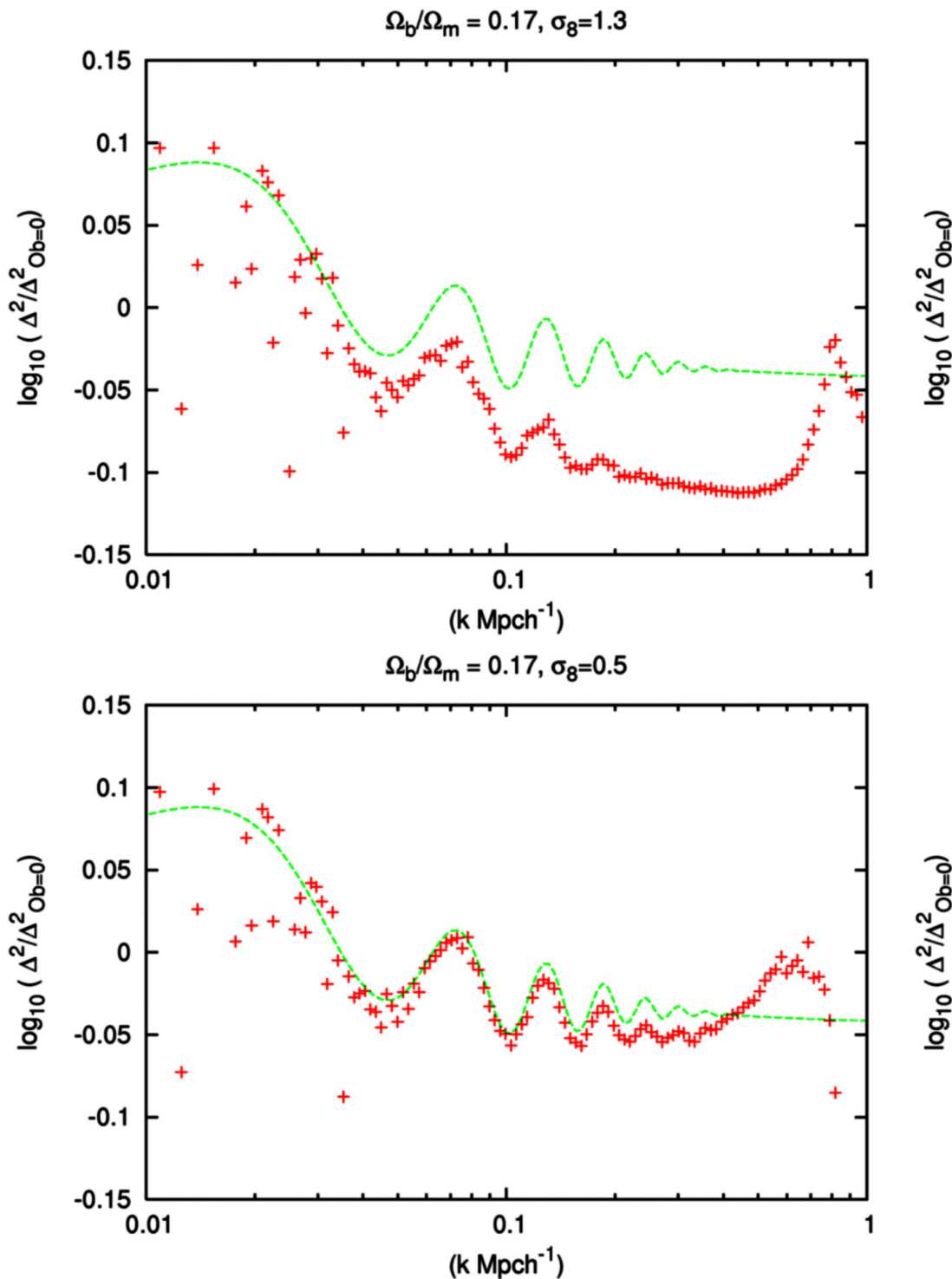


Figure 3-5: The matter power spectrum at $z = 1$ from an N-body simulation of a cube of side $2000 h^{-1}$ Mpc. Linear theory (green line) is compared with nonlinear results, varying the spectrum normalization (zero-redshift σ_8). Note the suppression in power for wavenumbers beyond the principal peak at $k \approx 0.06 h\text{Mpc}^{-1}$, and the visible shift in peak location in the high-normalization case.

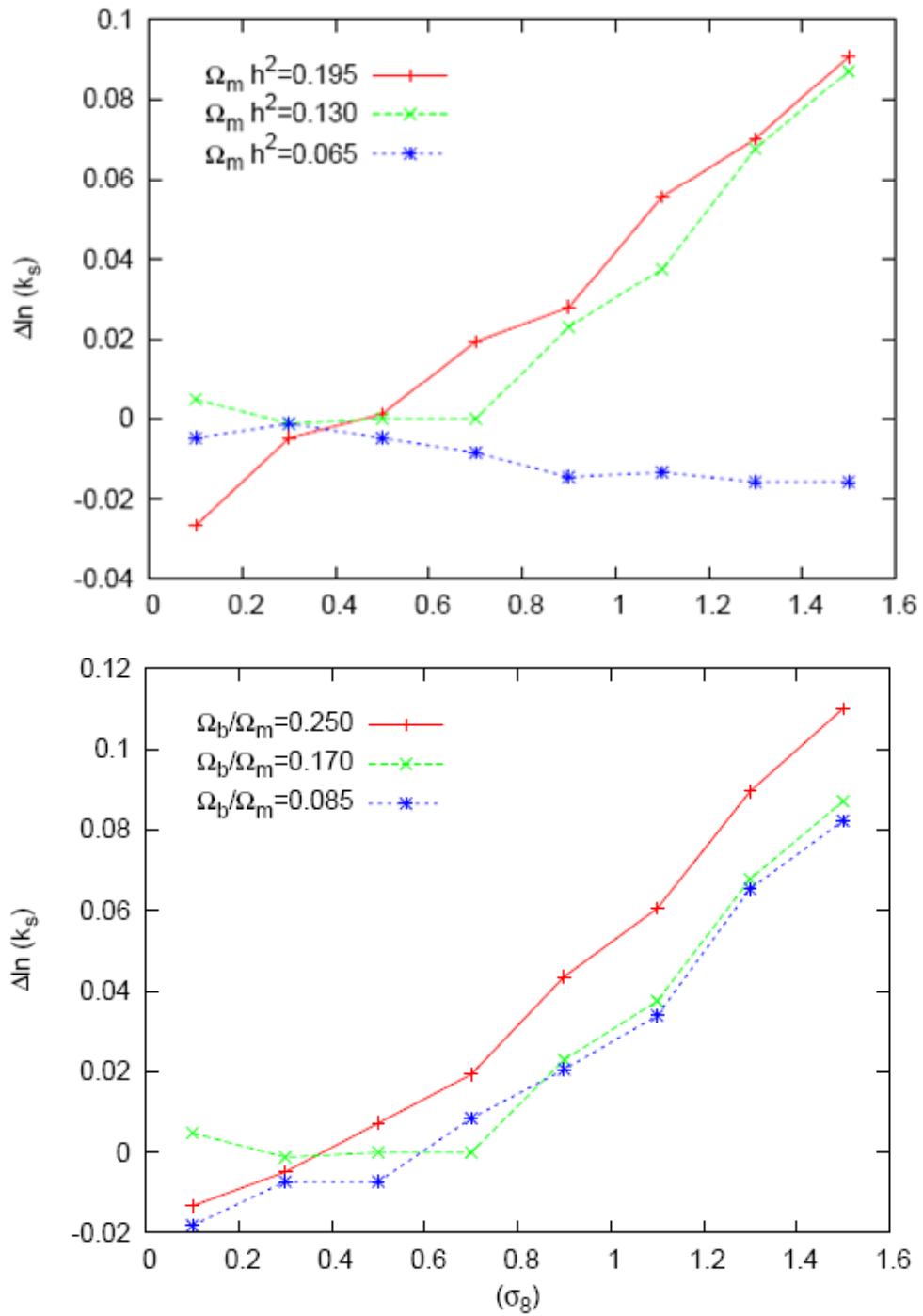


Figure 3-6: The fractional shift in the location of the principal acoustic peak owing to large-scale quasilinear effects. These plots consider the mass distribution at $z = 1$ and varies the zero-redshift normalization, σ_8 , together with the spectral shape parameter, $\Omega_m h$ (first panel), and the baryon fraction, Ω_b/Ω_m (second panel).

3.2.4 *Scale-Dependent Bias*

The more difficult issue of how galaxies relate to the mass requires detailed simulation, although the results can be incorporated into the ‘halo model’ formalism (Seljak 2000; Peacock & Smith 2000), and we intend to use this to perform larger galaxy simulations. In the meantime, we can study the results from the Millennium Simulation (Springel et al. 2005), which has a simulation volume $500 h^{-1}$ on a side. The semianalytic apparatus yields a galaxy population that should be our best current guide as to what systematics to expect.

Figure 3-7 contrasts the mass and galaxy power spectra at various epochs. To some extent, this is encouraging for $z = 3$: the nonlinear mass spectrum clearly shows a third peak at $k \approx 0.2 h \text{ Mpc}^{-1}$, which is not really apparent at either $z = 0$ or $z = 1$. On the other hand, the shapes of the galaxy and mass power spectra start to diverge at smaller k at $z = 3$ than at $z = 1$, reflecting the larger degree of bias for galaxies at that redshift – and indeed the galaxy spectrum shows no more evidence for a third peak at $z = 3$ than it does at $z = 1$. This indicates that one should be extremely cautious about expecting to use galaxy data beyond the second peak at any redshift. We have therefore generally assumed a conservative limit of $k < 0.15 h \text{ Mpc}^{-1}$ in most analyses.

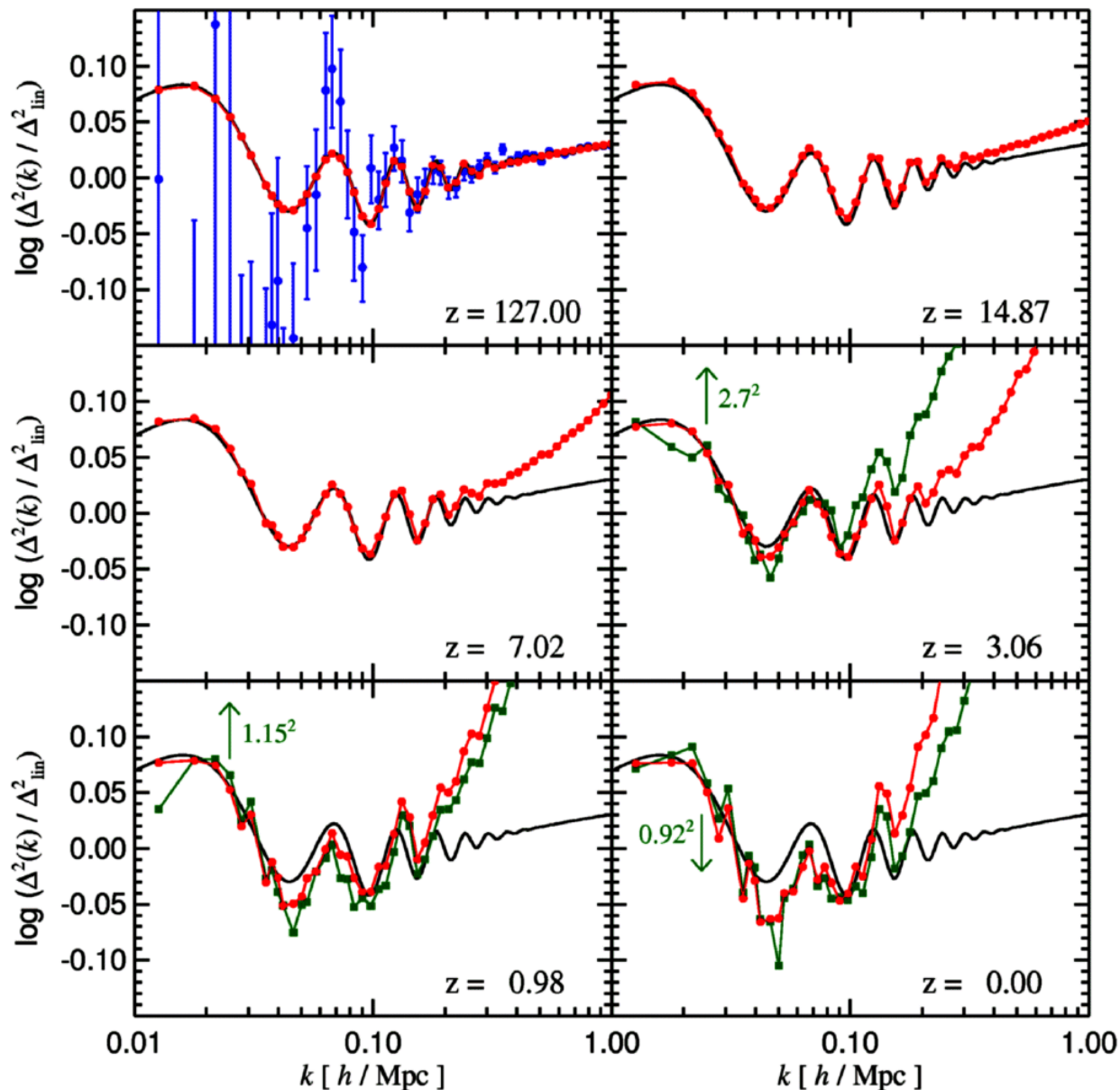


Figure 3-7: The power spectrum from the Millennium Simulation (Springel et al. 2005). The plot shows the linear power spectrum ratioed to a smooth model (black), the nonlinear mass power spectrum (red), and the galaxies (green), scaled to allow for bias.

3.3 Expected Performance of WF MOS in Measuring the BAO Signature

We now look in more detail at the precision we can expect from the BAO test in the context of the surveys we will justify in more detail in Section 3.7. It is helpful to begin our discussion with forecasting the expected power of WF MOS to carry out the *pure* geometrical measurement of $H(z)$ and $D_A(z)$, before relating these to inferences on dark energy. To be more precise, the galaxy power spectrum is modeled as a set of parameters p_α :

$$p_{\alpha} = [\Omega_m, \omega_m, \omega_b, n_s, \delta_R, D_A(z_1), \dots, D_A(z_{N_s}), H(z_1), \dots, H(z_{N_s}), b_1(z_1), \dots, \beta(z_1), \dots]. \quad (15)$$

This is not the only possible parameterization. For example, the Hubble parameter does not appear, being implicit in $\omega_m \equiv \Omega_m h^2$ etc. Similarly, the normalization is given as a curvature fluctuation δ_R , rather than the more down-to-earth σ_8 . These different choices have no significant effect on our conclusions. The fiducial parameters are chosen to match a flat CDM model with a cosmological constant, consistent with the WMAP results. Using this parameter set and combined with expected CMB constraints, we can convert measurement errors on the galaxy power spectrum into errors on the $H(z_i)$ and $D_A(z_i)$ determination at each redshift, marginalized over other parameters ($w_m, w_b, n_s, \dots, \beta$). Hence, ignoring the shape information in the galaxy power spectrum gives us a conservative estimate of the parameter forecasts. In addition we include only power spectrum information up to some maximum wavenumber k_{\max} in order to restrict our parameter forecasts to the linear or quasi-nonlinear regime, where k_{\max} for each redshift slice is set following Seo & Eisenstein (2003).

We apply this method to WF MOS in Figure 3-8. Anticipating the final results of our study, we show the predictions for the areas we propose in Section 3.7: 3000 deg² at $z \sim 1$ and only 100 deg² at $z \sim 3$. WF MOS allows a precise determination of $H(z)$ and $D_A(z)$ to a few % accuracy for each redshift slice. In other words, the locations of baryon peaks in $P(k)$ are measured to a precision of 1–2% level for each slice. Bearing in mind the w multiplier ‘rule of 5’, this shows that such surveys can be expected to measure a constant w to a precision of 5–10%. It is also clear from this plot that any systematics leading to a shift in the baryon peaks needs to be controlled to well under 1% precision in scale in order to achieve the full potential of WF MOS.

As is apparent from the basic $P(k)$ S/N formula, the precision of the BAO experiment depends quite strongly on the range of wavenumber k considered. Figure 3-8 makes the most optimistic assumption, which is that a higher redshift slice allows use of the power spectrum to a larger maximum wavenumber k_{\max} due to the weaker non-linearities in structure formation. In this case, for a given volume and sample size, $H(z)$ and $D_A(z)$ are more precisely measured by a $z \sim 3$ survey than a $z \sim 1$ survey. Therefore, if the dark energy density is strongly evolving toward higher redshifts, albeit unlikely, the $z \sim 3$ survey could offer a unique window for probing such a dark energy model. We discuss below whether the assumption of a wider k range at high redshift is realistic. If it is not, then we should consider the alternative possibility of a fixed k range – for which the $z \sim 3$ experiment is much less impressive, since it inevitably maps volume at a slower rate than at $z \sim 1$. Henceforth, we take this more conservative approach adopting a maximum $k = 0.15 h \text{ Mpc}^{-1}$

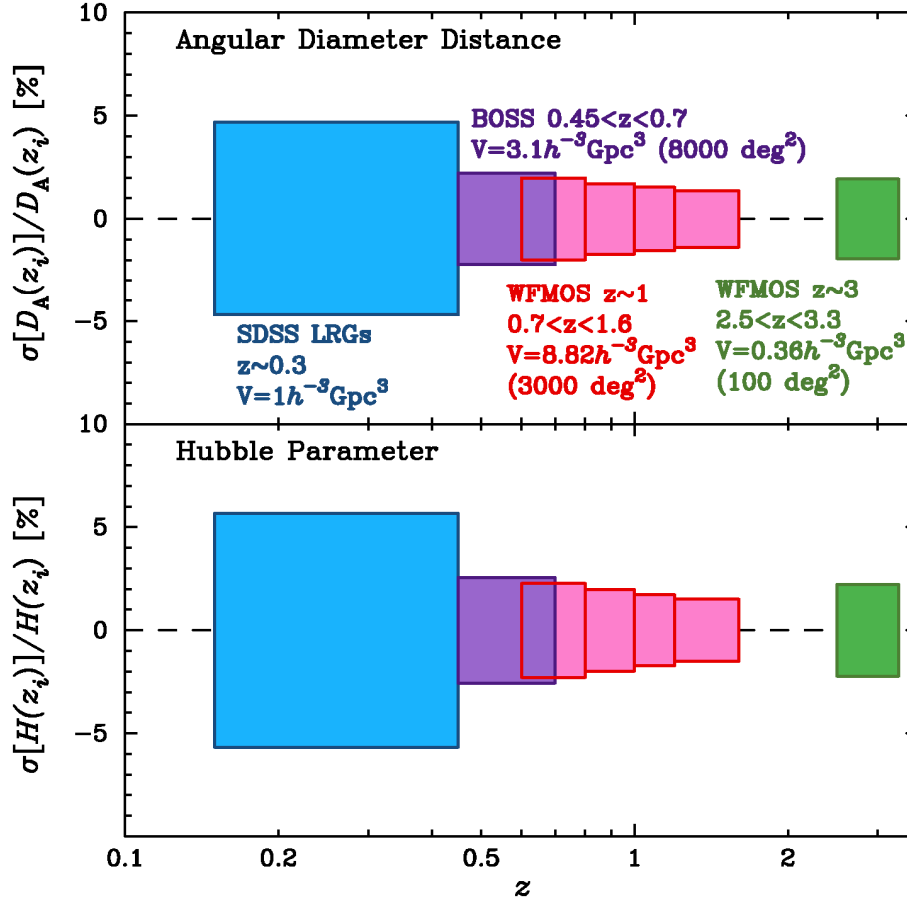


Figure 3-8: Expected performance of WF MOS for determining $D_A(z)$ and $H(z)$ at each redshift of the surveyed redshift slices based on the BAO geometrical test. The accuracy shown here is relative to the fiducial model with cosmological constant. We have assumed WF MOS surveys that differ from the feasibility survey, consistent with our final proposals.

3.3.1 Contrasting High and Low Redshift Surveys

Given the estimated accuracies of $H(z)$ and $D_A(z)$, we can derive the expected performance of WF MOS for constraining a specific dark energy model. We employ the model in which the evolution of dark energy as a function of scale factor is specified by the equation of state parameters w_0 and w_a :

$$w(a) = w_0 + w_a(1 - a). \quad (16)$$

Following the DETF report, we express this in terms of w at the pivot redshift, where the parameters are then uncorrelated. The error on w_{pivot} tells us that a given dataset can provide the tightest constraint on the constant equation of state effectively at the pivot redshift z_{pivot} .

Figure 3-9 shows the marginalized error on w_p as a function of z_p expected from WF MOS combined with Planck and SDSS, *assuming in the first instance a flat universe*, which we emphasize is a significant

restriction, but useful for a first illustration. The three curves show the results obtained when either one of the $z \sim 1$ and $z \sim 3$ surveys is used or both are combined. As can be seen from each of the curves, the error on w_p is minimized at a particular redshift, the pivot redshift z_{pivot} , showing the best performance of a given data set to constraint on the constant equation of state parameter, w_{pivot} :

$$\begin{aligned}
 z = 1: & \quad z_{\text{pivot}} = 0.57, \quad \sigma(w_{\text{pivot}}) = 0.068, \quad \sigma(w_{\text{pivot}}) \times \sigma(w_a) = 0.082 \\
 z = 3: & \quad z_{\text{pivot}} = 0.78, \quad \sigma(w_{\text{pivot}}) = 0.110, \quad \sigma(w_{\text{pivot}}) \times \sigma(w_a) = 0.130 \\
 z = 1 + z = 3: & \quad z_{\text{pivot}} = 0.64, \quad \sigma(w_{\text{pivot}}) = 0.062, \quad \sigma(w_{\text{pivot}}) \times \sigma(w_a) = 0.046 \\
 BOSS: & \quad z_{\text{pivot}} = 0.52, \quad \sigma(w_{\text{pivot}}) = 0.115 \quad \sigma(w_{\text{pivot}}) \times \sigma(w_a) = 0.140
 \end{aligned} \tag{17}$$

The third quantity $\sigma(w_{\text{pivot}}) \times \sigma(w_a)$ gives an estimate of the area of the error ellipse in (w_0, w_a) plane, the reciprocal of which was advocated by the Dark Energy Task Force as the Figure of Merit (FoM) of a given data set for constraining the two parameters (w_0, w_a) simultaneously. Because the dark energy becomes subdominant beyond $z = 1$, adding the $z = 3$ survey improves the accuracy of w_{pivot} by only about 10%. On the other hand, the $z = 3$ survey modestly improves our ability to constrain a time variation of the dark energy equation of state: it increases the FoM by about 50% compared to the $z = 1$ survey alone. It should be noted that the width of the curves in Figure 3-9 provides a range of redshift where given data sets have sensitivity to constrain the dark energy equation of state. Adding the $z = 3$ survey broadens the sensitivity window; for example, for an accuracy of $\sigma(w_0) \leq 0.1$, the $z = 1$ plus $z = 3$ surveys yields a wide range of the sensitivity redshift, $0.3 \leq z \leq 1$.

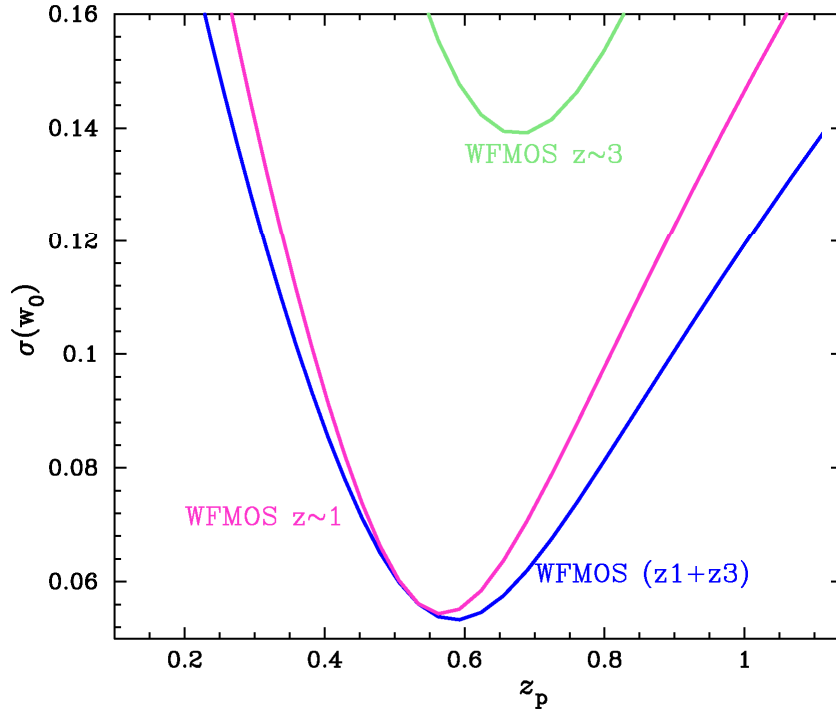


Figure 3-9: 68% error on w_p , marginalized over other parameter uncertainties, for the model $w(a) = w_p + w_a(a - a_p)$ with varying parameter a_p . The errors are for WF MOS combined with SDSS ($z < 0.3$) and Planck. The three curves correspond to the results expected when either alone of the $z = 1$ or $z = 3$ slices is used or the two surveys are combined.

In practice, the pivot redshifts turn out to be close to redshift 0.6 in most cases. For anything close to a cosmological constant, the vacuum becomes subdominant beyond $z = 1$. If we had a strong prejudice that the linear model for the evolution of $w(a)$ was correct, the conclusion from this would be that the extra baseline from $z \sim 1$ to $z \sim 3$ adds little to our knowledge of w at the pivot redshift. Since we will see that $z \sim 3$ surveys are much more expensive in terms of telescope time, this argues for learning from a well-defined $z \sim 1$ survey as an initial goal. Of course, we do not have perfect confidence in the linear model, so $z \sim 3$ should not be neglected entirely, and in any case we will see that there is a good case from the point of view of redshift-space distortions for including a modest amount of $z \sim 3$ data in our main goals.

3.3.2 Fisher Matrices and Figures of Merit

The above discussion has given a simple discussion of the precision that should be attainable with the BAO method in measuring the acoustic scale using a survey similar to WF MOS. We now go into more detail on what these measurements would imply for our knowledge of the cosmological model.

The standard methodology for forecasting errors in cosmological parameters is in terms of the Fisher Matrix, which is the expected curvature matrix of the likelihood of a given model in the face of data:

$$F_{ij} = -\left\langle \partial^2 \ln L / \partial p_i \partial p_j \right\rangle, \tag{18}$$

where the p_i are a set of parameters characterizing the model. The inverse of F_{ij} gives a pseudo-covariance matrix, such that the diagonal elements are lower limits to the true variance in a given parameter—although they are usually taken to be a reasonable estimate of the actual expected error. The Fisher matrix thus defines a multi-dimensional Gaussian ellipsoid that gives the joint confidence region for the parameters. It is straightforward to marginalize over unwanted parameters (i.e., integrating the likelihood over all values of the hidden parameters). This yields a lower-dimensional projected likelihood, which in 2D may be plotted as a confidence ellipse, as shown in several plots below. For the present purpose, the plane of interest is $w_{pivot} - w_a$, where these two parameters are uncorrelated, and the DETF Figure of Merit is constructed in terms of the rms errors on the two parameters:

$$FoM = [\sigma(w_{pivot})\sigma(w_a)]^{-1}, \quad (19)$$

The Fisher matrix formalism is described in detail in e.g., the DETF report (Albrecht et al. 2006), and is widely used. It is however surprisingly hard in practice to achieve a set of results that agree well between different workers. One of the main reasons for this is that Fisher matrices are often ill-conditioned, with a large dynamic range in their eigenvalues: the very small eigenvalues correspond to directions in parameter space that are poorly constrained. In this case, small numerical errors in calculating the Fisher matrix may result in large changes in the error in those directions. With dark energy, it is rare for the evolution parameter w_a to be accurately determined, so we are always at risk of encountering this problem. For more detail of how hard it can be to obtain robust BAO figures of merit, see Rassat et al. (2008).

For this reason, it is helpful to give some explicit examples, based on Fisher matrices provided as part of the DETF work, via the DETFast package. We emphasize that, unlike our simplified example above, *we now allow the curvature of the universe to be a free parameter*, consistent with the choice of other comparable studies. As a baseline, we normally choose to present all accuracy forecasts assuming Planck data: CMB information constrains many cosmological parameters extremely well, so we have to ask what the added value of WF MOS will be. But, as shown in Rassat et al. (2008), BAO plus CMB only yields very weak constraints on dark energy, and it must be supplemented by further information. We take this to be provided by ‘stage II’ supernova data. Here then are Fisher errors and the FoM for these assumptions. For BAO data, we consider in turn the DETF ‘stage III’ BAO, which is in effect an early version of WF MOS surveys as envisaged in the feasibility study. To be absolutely explicit, the DETF Fisher matrix files involved are `planckfish.fisher`, `SN-II.fisher` and `BAO-IIIs-o.fisher`. These all work with an eight-dimensional parameter space, corresponding to a scalar CDM model with arbitrary tilt and arbitrary spatial curvature. We then consider replacing the BAO information with our estimates for BOSS, WF MOS, and WF MOS+BOSS.

BAO dataset	$\sigma(w_{pivot})$	$\sigma(w_a)$	$FoM = [\sigma(w_{pivot})\sigma(w_a)]^{-1}$
DETF	0.040	0.447	56
BOSS	0.041	0.499	49
WF MOS	0.038	0.369	71
WF MOS + BOSS	0.036	0.334	81

Other calculations are possible, and we emphasize that the exact figure of merit depends on the detail of the information being combined with the BAO experiment, which is why we have been explicit on this point. However, our aim here is to demonstrate the increase in power arising from the WF MOS experiment, which is substantial. We emphasize that this is very much a conservative figure, which could plausibly be increased to several hundred if it is possible to overcome some of the uncertainties of bias and use the full power spectrum information.

3.4 Redshift-Space Distortions and Modified Gravity

We now turn to the issue of using redshift-space distortions to go beyond dark-energy models and test the nature of gravity. The anisotropy of the power spectrum in redshift space derives from the fact that the growth of density fluctuations must be accompanied by peculiar velocities, simply from the requirement of mass conservation. At the level of linear perturbations, the comoving peculiar velocity field, \mathbf{u} , is related to the fractional density perturbation via

$$\nabla \cdot \mathbf{u} = -\partial \delta / \partial t. \quad (20)$$

These velocities add to the Hubble motion and cause us to mis-locate particles in the radial direction. This leads to the characteristic Kaiser (1987) effect, in which the linear mass power spectrum is made anisotropic:

$$P_s(\mathbf{k}) = P_r(k)(1 + f_g \mu^2)^2, \quad (21)$$

where μ is the cosine of the angle between the wavevector and the line of sight and f_g is the linear growth factor introduced earlier: $f_g = \partial \ln \delta / \partial \ln a$.

The galaxy power spectrum quantifies how the clustering of galaxies varies as a function of 3-dimensional wavenumber, k . However, we cannot measure lengths in real space: rather, we measure (1) angular positions of galaxies on the sky, and (2) radial positions in redshift space. To convert these data to positions in 3-dimensional space, one needs to assume a reference cosmological model, which will differ from the underlying true cosmology. As a result, the inferred components of the wavenumber along and perpendicular to the line-of-sight are related to the true values via

$$\begin{aligned}
k_{\parallel\text{ref}} &= \frac{H(z)_{\text{ref}}}{H(z)} k_{\parallel}, \\
k_{\perp\text{ref}} &= \frac{D_A(z)}{D_A(z)_{\text{ref}}} k_{\perp},
\end{aligned}
\tag{22}$$

where the quantities with and without the subscript ‘ref’ denote the quantities in the reference and true cosmological models, respectively.

An incorrect mapping of the observed angular and redshift positions to 3-dimensional positions introduces a distortion in the measured power spectrum, known as the ‘geometrical distortion’ (Alcock & Paczynski 1979; Ballinger, Peacock & Heavens 1996; Matsubara & Suto 1996). Taking into account the geometrical distortion, redshift distortion (Kaiser 1987), and galaxy bias, the apparent galaxy power spectrum at redshift slice is related to the true linear mass power spectrum $P(k, z)$ as follows:

$$P_s(k_{\parallel\text{ref}}, k_{\perp\text{ref}}; z) = \frac{D_A(z)_{\text{ref}}^2 H(z)}{D_A(z)^2 H(z)_{\text{ref}}} \left[1 + \beta(z) \frac{k_{\parallel}^2}{k_{\perp}^2 + k_{\parallel}^2} \right]^2 b_1^2 P(k; z),
\tag{23}$$

where $k \equiv (k_{\parallel}^2 + k_{\perp}^2)^{1/2}$, b_1 denotes a linear bias parameter and the linear redshift distortion parameter is $\beta = (1/b_1) d \ln D / d \ln a \approx \Omega_m(a)^{0.6} / b_1$.

While the baryon acoustic oscillations, or general features such as the break due to matter-radiation equality, imprint circular modulated patterns onto the galaxy clustering strength in real space $k \equiv (k_{\perp}, k_{\parallel})$, an error in the assumed reference cosmology yields a departure of the rings from perfect circles. In principle, this allows us to measure both $H(z)$ and $D_A(z)$, yielding a double geometrical test of cosmology. Thus a notable property of the BAO technique is that we can directly measure the Hubble expansion $H(z)$ at a given redshift, compared to the SNe method that probes the luminosity distance to a SN at a redshift z , related to the integrated information on $H(z)$ over a range of redshifts $[0, z]$. One attraction of this contrast is that SNe measure luminosity distances, whereas BAO measure angular-diameter distances; thus we can test the fundamental prediction of general relativity that $D_L(z) = (1 + z)^2 D_A(z)$.

In practice, it is often convenient to measure redshift-space effects via the correlation function in redshift space $\xi(r_{\perp}, r_{\parallel})$, where r_{\perp} and r_{\parallel} are pair separations perpendicular to the line of sight and along it. In this form, the Kaiser anisotropy tends to produce flattening of the contours of ξ along the line of sight. Following a number of preliminary attempts, the Kaiser effect was first detected with high S/N by the 2dFGRS (Peacock et al. 2001), and now the first claims have been made of a high-redshift detection, using the VVDS at $z = 0.8$ (Guzzo et al. 2008). The VVDS sample uses only 6000 galaxies between $z = 0.6$ and $z = 1.2$ to $I_{AB} < 22.5$, and so hardly competes with the 220,000 redshifts of the 2dFGRS, but it has been accepted as a proof of concept for a larger survey (P.I. Guzzo; provisionally entitled VIPERS: VImos Public Extragalactic Redshift Survey), which has been allocated 50 VLT nights over the next 3

years in order to gather 100,000 redshifts using similar techniques to the VVDS. Figure 3-10 contrasts the current VVDS measurement with the predicted result from the new survey.

The complication in interpreting these results comes from galaxy bias. For a highly biased population, the offsets produced by peculiar velocities are relatively less significant and so the redshift-space distortions are less. This is why redshift surveys measure the combination $\beta \equiv f_g / b$, where b is the linear bias parameter of the population in question. This number has to be eliminated in order to derive f_g itself, which is the quantity that forms a test of modifications of gravity. Two approaches can be taken to this. The first is the one used by the 2dFGRS to argue that the absolute degree of bias in that survey was small (Verde et al. 2002): this used higher-order correlations (in practice, the bispectrum—which is the Fourier equivalent of the three-point correlation function). A simpler alternative is to measure the bias directly: the amplitude of galaxy clustering is observed, and the amplitude of mass fluctuations at intermediate redshifts can be predicted almost exactly using CMB and other constraints, so the ratio of galaxy and mass power spectra can be measured. Of course, this requires us to assume the standard Λ CDM model for structure growth, which is what we want to test. But taking this route provides a consistency test, since in effect the value of β can be predicted; if the measured value is different, this amounts to a rejection of Einstein gravity.

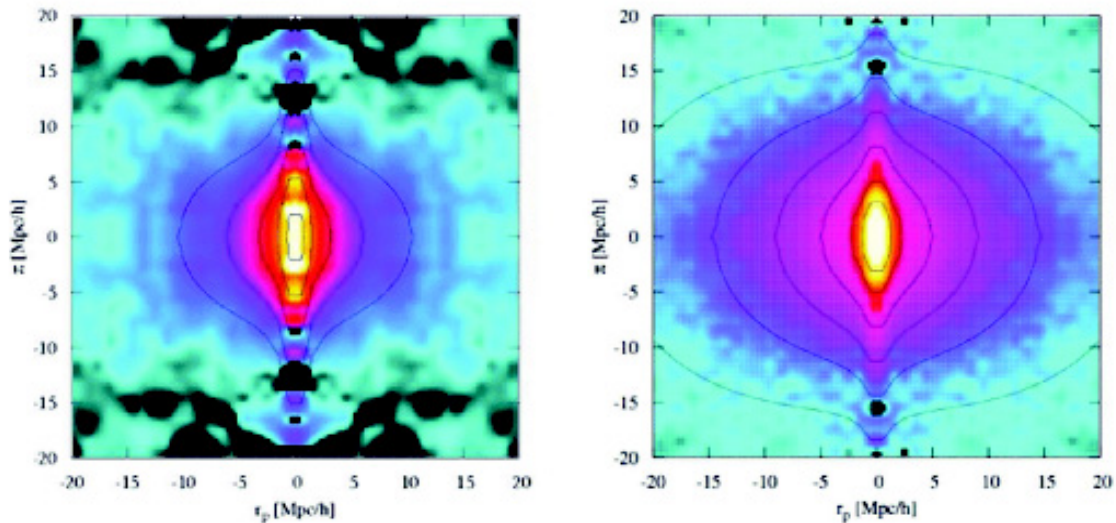


Figure 3-10: The redshift-space correlation function at $\langle z \rangle = 0.8$, shown in false color to emphasize the Kaiser flattening at amplitudes $\xi = 0.1$. Note the ‘finger-of-God’ radial stretching that arises from virialized random motions at separations of a few Mpc. The superimposed contours show the best-fitting model of a Kaiser flattening plus this small-scale elongation. The first panel shows the VVDS measurements with 6000 galaxies (Guzzo et al. 2008); the second panel is a simulation of the results expected from a forthcoming new VLT survey of 100,000 redshifts.

It is also necessary to worry about nonlinear effects. These are also visible in Figure 3-10 in the form of so-called Fingers of God, the radial stretching at small separations. This arises because the clustering

pattern is convolved by the distribution of random virialized velocities internal to dark-matter haloes. Techniques are well developed to model this distortion analytically, and these methods can be refined using N-body simulations. In one respect, this distortion is an advantage, since it means that our redshifts do not need to be of extreme accuracy: the one-galaxy rms line-of-sight velocity dispersion is 100–200 km/s, and our redshift accuracy only needs to be below about half this figure in order for spectroscopic measurement error to be relatively unimportant.

An attractive aspect of redshift-space distortions is that they yield a local measurement of f_g at the redshift of interest. This is cleaner than BAO measurements, where measuring the apparent BAO scale at a given redshift yields $D(z)$; because this is an integral, it is sensitive to the properties of dark energy at all redshifts up to z . As we have seen, this is why it is difficult to change the pivot redshift of dark energy very much even by going from a $z = 1$ survey to one at $z = 3$. The high-redshift surveys add power only in the case of models where there is rapid evolution in the properties of dark energy at high redshifts. Something similar still applies in this case, however. Redshift-space distortions arise from peculiar velocities, and it would be unphysical to expect these to undergo sudden jumps. The general equation for the comoving peculiar velocity is

$$\mathbf{u}(a) = a^{-2} \int \mathbf{a}g(a) dt, \quad (24)$$

where \mathbf{g} is the acceleration vector induced by density perturbations. But in this case, the integral over time refers to redshifts *higher* than the one where we make our survey. Since density fluctuations are expected to grow by a factor $\simeq 2$ between $z = 3$ and $z = 1$, there is a good degree of independence between the f_g information at these redshifts.

This fundamental cosmology application is very well suited to WF MOS, and offers the chance to achieve substantial gains over any likely competition at relatively modest cost. This is partly because it is a method that is unique to spectroscopic galaxy surveys, and partly for the reasons of redshift independence mentioned above. From this point of view, testing gravity via redshift-space distortions is at least as good a scientific fit for WF MOS as the measurement of $w(z)$ via the BAO signature. The combination is particularly powerful.

3.5 Further Applications and Challenges

We have so far only considered the application to dark-energy cosmology of the detailed measurements of galaxy clustering that will be forthcoming from WF MOS. But there are other important aspects that should not be neglected, and we discuss some of these here.

3.5.1 Neutrino Mass Constraints

A particularly exciting possibility is that WF MOS surveys may be used to measure the neutrino mass. Neutrinos are so far the only form of particle dark matter whose existence is definitely established. Solar, atmospheric, reactor and accelerator neutrino experiments have demonstrated that neutrinos have non-

zero mass, but their absolute masses are still unknown. The reason for this is that existing ‘neutrino oscillation’ experiments measure differences in the mass-squared between three neutrino mass states:

$$\begin{aligned}\Delta(m_{21})^2 &= 8.0 \times 10^{-5} \text{ eV}^2, \\ \Delta(m_{32})^2 &= 2.5 \times 10^{-3} \text{ eV}^2.\end{aligned}\tag{25}$$

where m_1 , m_2 and m_3 are the three mass eigenstates. This information does not give the absolute mass scale, nor does it tell us whether there is a normal hierarchy with $m_3 \gg m_2 \gg m_1$, or an inverted hierarchy in which states 1 & 2 are a close doublet lying well above state 3. Cosmology can settle both these issues by measuring the total mass density in neutrinos. The absolute minimum situation is a normal hierarchy with m_1 negligibly small, in which case the mass is dominated by m_3 , which would then be around 0.05 eV. The cosmological limits are already within a power of 10 of this interesting point.

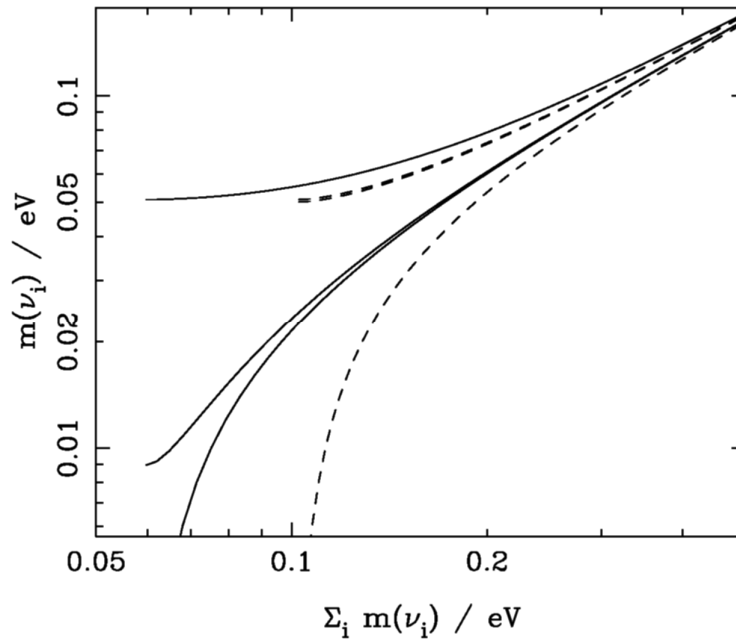


Figure 3-11: The masses of the individual neutrino mass eigenstates, as constrained by neutrino oscillation experiments, plotted against the total neutrino mass for a normal hierarchy (solid lines) and an inverted hierarchy (dashed lines). Current cosmological data set an upper limit on the total mass of light neutrinos of around 0.6 eV

Cosmology can provide an upper limit on the sum of neutrino masses (for a review see e.g., Elgaroy & Lahav 2005; Lesgourgues & Pastor 2006). The key point here is that the behaviour of the matter spectrum $P(k,z)$ with redshift z is sensitive to the total neutrino mass, in a way distinctly different from the cold dark matter component. This is implemented by measuring the suppression of the power spectrum due to the neutrino free streaming that takes place while the neutrinos are relativistic. The current mass upper limit, obtained using CMB WMAP data, SN Ia and the BAO from 2dFGRS and SDSS, is $m_{\text{tot}} < 0.61 \text{ eV}$ at 95% CL (Komatsu et al. 2008).

The challenge now is to bring down reliably the upper limits to the sub-eV level or even detect the neutrino mass. Conversely, if the sum of the neutrino masses were known from particle physics, cosmological probes could be used to place tighter constraints on cosmological parameters, e.g., dark energy parameters the amplitude of fluctuations and the primordial spectral index. We also note a degeneracy between the neutrino mass and the dark energy equation of state parameter w (Lesgourgues & Pastor 2006; Kiakotou, Elgaroy & Lahav 2008), so quantifying the neutrino mass is essential for accurate measurement of the Dark Energy.

WF MOS can play a key role in setting a tight upper limit on the neutrino mass, and possibly detect it if the true neutrino mass is sufficiently high. Saito, Takada & Taruya (2008) investigated the non-linear evolution of the density perturbation in the presence of massive neutrinos and pointed out that the matter power spectra at intermediate redshifts can be a promising tool for probing neutrino masses. They demonstrated that the non-linear correction would improve the neutrino mass constraint by a factor of two compared with assuming just linear theory (which under-predicts the suppression). WF MOS would enable us to control non-linearity more reliably and this in turn would allow us to use additional data at smaller scales. The latest calculations by our team members forecast a 1-sigma error of 0.097 eV on $m_{\nu, \text{tot}}$ from WF MOS. This means that if $m_{\nu, \text{tot}} = 0.1$ in nature, WF MOS results will be just at the point of a 1-sigma signal. On the other hand if the true neutrino mass is very close to zero, then we can obtain an upper limit of 0.19 eV (95% CL).

One source of uncertainty in constraining neutrino mass from galaxy surveys is galaxy biasing (e.g., Elgaroy & Lahav 2005). Fortunately there are several independent ways of controlling this systematic effect: (i) modelling the biasing via halo model or semi-analytic simulations and marginalising over the biasing parameters; (ii) estimating the neutrino mass from galaxy power-spectra derived for different galaxy types and checking for consistency; and (iii) estimating the biasing empirically from weak-lensing map to be produced e.g., from HSC.

The level of sensitivity for neutrino mass from WF MOS is of much relevance to the direct measurement of the neutrino mass from laboratory experiments, e.g., the KATRIN tritium beta decay experiment. Furthermore, the WF MOS measurements can be combined with laboratory experiment to derive more accurate neutrino masses (e.g., Host et al. 2007 who combined KATRIN with the CMB).

To summarize, if the total neutrino mass is 0.1 eV or so, we should actually detect it with WF MOS. This would be a development of profound importance for fundamental physics.

3.5.2 *Galaxy Biasing*

An a-priori understanding of bias may seem an unrealistic assumption, but empirical progress is possible by using redshift-space distortions. Measuring the redshift distortion parameter

$$\beta = \Omega_m^\gamma / b_1. \quad (26)$$

allows us to measure the galaxy bias b_1 because $\Omega_m(a)$ is well constrained by other information. In turn, a precise determination of b_1 permits a direct determination of the matter power spectrum amplitude, providing vital information on the growth rate when combined with CMB data. Note that the linear distortion effect above ceases to be accurate enough for the precision of WF MOS even on the large spatial scales of our interest, and an issue is how a more sophisticated model of the distortion effect including the non-linear correction can be developed analytically as well as based on N-body simulations (e.g., Scoccimarro 2004). Depending on the extent to which this problem can be overcome, the following two cases might be feasible as possible extensions of the WF MOS experiment from the pure geometrical test.

(1) In addition to the baryon peak locations, the shape information of the galaxy power spectrum in redshift space may be included for the cosmological interpretation, but b_1 and β are treated as free (nuisance) parameters, corresponding to the case where systematics in b_1 and β cannot be well controlled. To be more precise, we deal with a set of parameters

$$p_\alpha = [\Omega_m, \omega_m, \omega_b, n_s, \delta_R, w_0, w_a, b_1(z_1), \dots, b_1(z_{N_s}), \beta(z_1), \dots, \beta(z_{N_s})] \quad (27)$$

in the Fisher matrix analysis. The angular diameter distance and Hubble function in the redshift-space power spectrum are both specified by cosmological parameters, and therefore the parameter set above is more restrictive compared to the full set. This corresponds to a case where we include the shape and amplitude of the redshift-space power spectrum in order to constrain cosmological parameters, but we allow the linear bias and redshift distortion parameters, b_1 and β , to vary freely in the model fitting.

(2) Being more ambitious, the redshift distortion effect on the galaxy power spectrum can be used based on a reliable model, but without assuming that the bias b_1 can be measured. The parameter set becomes a minimal one

$$p_\alpha = [\Omega_m, \omega_m, \omega_b, n_s, \delta_R, w_0, w_a, b_1(z_1), \dots, b_1(z_{N_s})]. \quad (28)$$

Figure 3-12 shows the expected improvement in the projected error ellipses in the (w_0, w_a) sub-space when the shape of the galaxy power spectrum is included (intermediate contour) and the redshift distortion effect is further included (innermost contour). It is interesting to find that the areas of error ellipses significantly shrink when either or both of the power spectrum shape and the redshift distortion can be used, compared to the conservative estimate of the pure geometrical test. The pivot redshift, the minimum error on the constant equation of state parameter, and the FoM are as follows, for (1) geometrical test only; (2) including growth; (3) including growth plus redshift-space distortions:

$$\begin{aligned} (1) \quad & z_{\text{pivot}} = 0.64, \quad \sigma(w_{\text{pivot}}) = 0.062, \quad \sigma(w_{\text{pivot}}) \times \sigma(w_a) = 0.0460 \\ (2) \quad & z_{\text{pivot}} = 0.36, \quad \sigma(w_{\text{pivot}}) = 0.044, \quad \sigma(w_{\text{pivot}}) \times \sigma(w_a) = 0.0130 \\ (3) \quad & z_{\text{pivot}} = 0.26, \quad \sigma(w_{\text{pivot}}) = 0.025, \quad \sigma(w_{\text{pivot}}) \times \sigma(w_a) = 0.0037 \end{aligned} \quad (29)$$

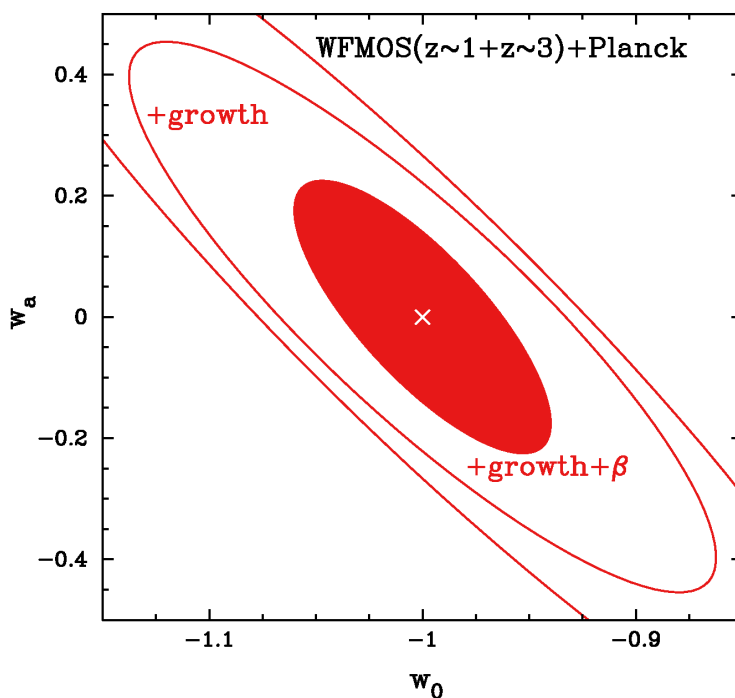


Figure 3-12: A potential improvement in the projected 2-parameter 68% C.L. errors in (w_0, w_a) subspace, expected for an extensive use of the WF MOS galaxy power spectrum. The outermost contour shows the forecast when the pure geometrical test of BAO experiment is used. The middle and innermost contours show the improvements when the growth rate information is included or the redshift distortion is further included.

Interestingly, $\sigma(w_{\text{pivot}})$ and the joint constraints on w_0 and w_a are improved by a factor of 2.5 and 10, respectively, with the WF MOS survey alone, if correct models for the power spectrum shape and the redshift distortion are available. Also note that the pivot redshift z_{pivot} becomes close to the present day by adding the information on the growth rate, because the sensitivity of growth rate to dark energy is greater at lower redshifts.

Finally, an aside on the CMB. We have so far combined predicted Planck temperature correlations with WF MOS data. It is important to ask how the forecasted errors would degrade if the Planck information were not available. The corresponding error estimates are

$$\begin{aligned} \text{Planck: } \sigma(w_{\text{pivot}}) &= 0.062 \text{ (GT)}, & \sigma(w_{\text{pivot}}) &= 0.025 \text{ (GT+Growth+}\beta) \\ \text{WMAP: } \sigma(w_{\text{pivot}}) &= 0.083 \text{ (GT)}, & \sigma(w_{\text{pivot}}) &= 0.031 \text{ (GT+Growth+}\beta) \end{aligned} \quad (30)$$

Thus, reassuringly, WMAP is approaching an adequate level of precision for the present purpose – and will certainly become closely comparable to Planck if extended to 8 years as planned.

3.6 Lensing Synergy

A major strategic driver for WF MOS is the fact that a comparably ambitious instrument, HyperSuprimeCam (HSC), is now under construction which will utilize the same panoramic prime focus corrector. We now consider the implications of using WF MOS to perform spectroscopy in areas of the sky that will have been previously imaged by HyperSuprimeCam (HSC). The synergy relates to how HSC can assist WF MOS (in the provision of targets) and how WF MOS can assist HSC (in calibrating photometric redshifts). The over-arching factor is the promise of HSC in constraining cosmology through the application of weak gravitational lensing.

Weak gravitational lensing distorts, or shears, the images of distant galaxies by deflecting their emitted light as it travels across the Universe. This deflection is due to the gravitational field of intervening matter. Gravitational lensing probes the intervening mass distribution independent of its dynamical and thermodynamic state and independently of galaxy bias. The analysis of weak lensing signals as a function of the photometric redshifts of the background galaxies is termed 3-D weak lensing.

3-D weak lensing is sensitive to both the growth of structure and the geometry of the Universe. Both effects can be probed by taking examining shear power spectra or correlation functions of distant galaxy images as a function of redshift. In addition, the geometry of the Universe can be isolated by taking the ratio of the image shear behind dark matter haloes at different redshifts, thereby removing the dependence on the amplitude and growth of structure.

3.6.1 Strategic Considerations

Conducting a HSC weak lensing survey in the same area as a WF MOS BAO survey would be highly beneficial. Naturally the magnitude limits are very different; the weak lensing survey must optimize for a very faint limit and high surface density, well beyond reach of WF MOS spectroscopy. Nonetheless, BAO survey galaxies must be selected from a pre-existing photometric redshift catalogue and a 3-D weak lensing survey requires photometric redshifts that must be extremely accurately calibrated from a substantial spectroscopic survey. In addition to these technical synergies, the scientific value of combining 3-D weak lensing with a BAO survey is also substantial, particularly in breaking degeneracies in the parameters which improve our understanding of dark energy.

When considering dark energy constraints, imaging and spectroscopic surveys involve very different systematics. BAO surveys suffer from uncertainties arising from galaxy bias, nonlinearity of the galaxy distribution, and redshift-space distortions. Weak lensing surveys suffer from the need for high image quality, accurately calibrated photometric redshifts, and uncertainty in the theoretical nonlinear mass distribution.

3.6.2 Benefits of Combining a BAO and 3-D Weak Lensing Survey

In the following, we quantify the scientific benefits of acquiring weak lensing and WF MOS data in the same survey areas. We stress that our discussion is schematic as plans for HyperSuprimeCam imaging

surveys have not yet been agreed. Moreover, as the imaging performance of HSC is not yet verified, we have not yet incorporated estimates of instrumental systematics in our weak lensing calculations. Such detailed calculations are beyond the scope of the current study. As an illustration we assume a common survey area of 2000 sq deg. for both the imaging and spectroscopic surveys.

Probing dark energy: Figure 3-13 shows the $w_0 - w_a$ plane for our combined 2000 sq. deg. WF MOS and HSC surveys where we have assumed the latter achieves a surface density of 30 galaxies arcmin⁻² and median redshift of $z = 1$. The 3D Weak Lensing survey is used to estimate the 3-D shear power spectrum and a shear ratio analysis provides a geometrical constraint, in conjunction with Planck. Assuming an 11-parameter cosmological model with spatial curvature, $(\Omega_m, \Omega_\nu, \Omega_b, \Omega_{tot}, \sigma_8, h, \tau, n_s, r, w_0, w_a)$, we have marginalized over all other parameters. Contours are two-parameter, one-sigma (68%) confidence contours, while the marginalized one-parameter, one-sigma error is quoted.

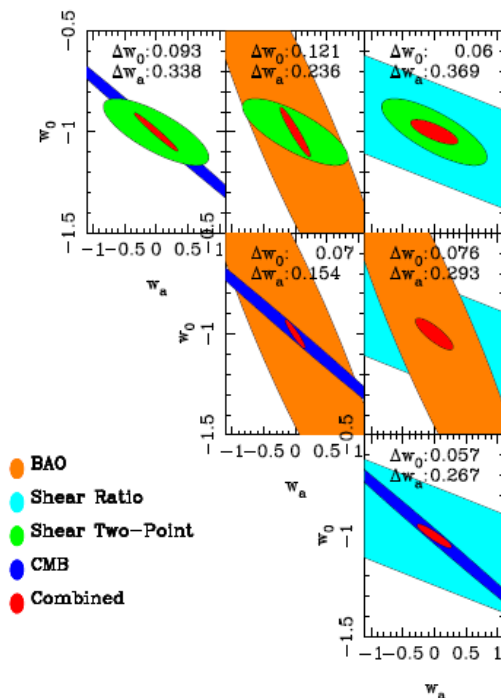


Figure 3-13: Dark energy parameters for a WF MOS BAO survey with a HyperSuprimeCam (HSC) 3-D Weak Lensing survey and the Planck Surveyor CMB experiment. From top left to right and top to bottom are shown (i) HSC shear power and Planck CMB, (ii) HSC shear power and WF MOS BAO, (iii) HSC shear power and shear ratios, (iv) WF MOS BAO and Planck CMB, (v) HSC shear ratios and WF MOS BAO, (vi) shear ratios and Planck CMB.

Weak Lensing alone: On its own our assumed HSC weak lensing survey, combining dark energy estimates from shear power and shear ratios, can achieve $\delta w_0 = 0.06$ and $\delta w_a = 0.37$.

Combining two probes: The HSC shear power analysis alone, combined with either Planck or with the WF MOS BAO survey, will yield around $\delta w_0 = 0.10$ and $\delta w_a = 0.25$. The HSC shear-ratio test alone, combined with Planck, will yield $\delta w_0 = 0.06$ and $\delta w_a = 0.27$, while combining it with WF MOS BAO's will yield $\delta w_0 = 0.08$ and $\delta w_a = 0.29$. This can be compared with the WF MOS BAO experiment, which can be combined with Planck to yield $\delta w_0 = 0.07$ and $\delta w_a = 0.15$. While these estimates of the dark energy parameters are not strictly independent, since we only have three probes, they can be compared as a check for consistency. Any notable deviation may indicate the presence of an unaccounted systematic, or effect from modified gravity.

Combining three probes: Figure 3-14 shows the results of combining three of the four experiments: WF MOS BAO, HSC shear power and shear ratios, and Planck CMB. In all cases, the combinations can yield around $\delta w_0 = 0.035$ and $\delta w_a = 0.10$, and again provided a series of consistency checks.

All four probes: Combining all four methods yields an accuracy of $\delta w_0 = 0.027$ and $\delta w_a = 0.082$

Galaxy bias: As well as directly measuring dark energy properties, weak lensing can also probe the dependence between mass and galaxies. In particular weak lensing can study the possibility of scale-dependent galaxy bias on large scales, which could affect the BAO measurement. Since the effects of galaxy bias are perhaps the largest uncertainty for the BAO method, a direct test of this with lensing would significantly improve the fidelity of the BAO results.

3-D mass mapping: With a well-calibrated 3-D photometric redshift weak lensing survey, the 3-dimensional mass distribution can be mapped. This can be used to study both the cluster-scale dark matter haloes, and the evolution of dark matter perturbations with redshift.

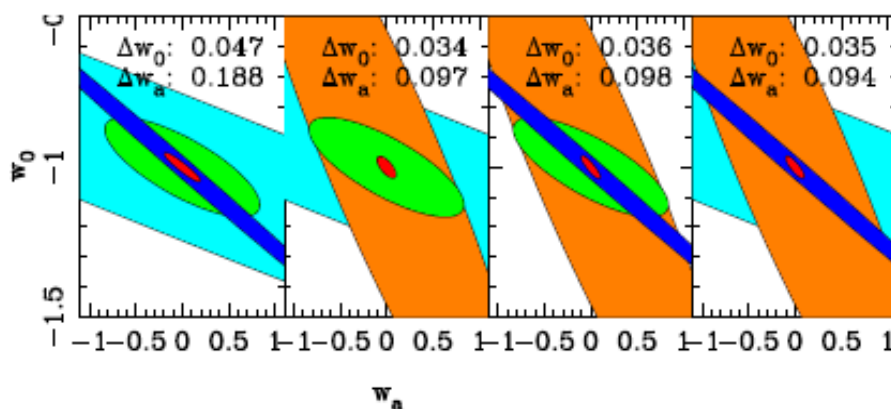


Figure 3-14: Combining three independent experiments. Left to right: (i) Planck CMB, HSC shear power and shear ratios, (ii) WF MOS BAO, HSC shear power and shear ratios, (iii) WF MOS BAO, HSC shear power and Planck CMB, and (iv) WF MOS BAO, HSC shear power and Planck CMB.

In summary, by coordinating HSC and WF MOS surveys:

1. The shear power spectra and shear-ratio geometric tests of weak lensing can be used to break the $w_0 - w_a$ parameter degeneracy present in WF MOS BAO results.
2. We can examine how well light (as delineated by the galaxy distribution) traces dark matter (as revealed by weak lensing). This can be used to probe systematic effects in BAO by measuring galaxy bias as a function of scale.
3. Weak lensing can deliver 3-D mass maps and evolution of dark matter perturbations with redshift up to $z = 1$.

3.6.3 Broader Synergy between WF MOS and HSC

Weak lensing with HSC will achieve the ultimate cosmological accuracy in the next decade by using photometric redshifts for a telescope widely considered to offer the best ground-based image quality. However, this goal will only be achieved if biases in the photo- z 's can be very accurately characterized. Following Huterer et al. (2006), the mean redshift in each photometric redshift bin needs to be known with $\sim 1\%$ accuracy in order to avoid a significant bias in dark energy parameter constraints. The statistical random errors on photo- z 's are not problematic, because the errors are expected to be typically $\delta z \sim 0.1$ for individual galaxies and $\sim 10^8$ galaxies are available in each redshift bin to average down this scatter. The major issue is to remove contamination caused by catastrophic photo- z outliers. A training spectroscopic galaxy sample is essential. We note that likely HSC surveys will not be shot noise limited, so that a significant fraction of galaxies can be discarded if their redshifts are ill-defined without severely degrading parameter accuracy (see e.g., Jain, Connolly & Takada 2007).

Clearly WF MOS can offer an ideal training spectroscopic dataset. Following Huterer et al. (2006) and Ma, Hu & Huterer (2006), a spectroscopic sample of $\sim 10^6$ galaxies with redshift coverage $0.7 < z < 1.6$ is sufficient to reduce the photo- z bias down to $\delta z \sim 10^{-3.5}$, well below the required 1% accuracy. However, this calibration is valid only if the WF MOS spectroscopic galaxies are a representative fair sample of the HSC weak lensing imaging galaxies. This is unlikely because WF MOS will target particular types of galaxies such as emission-line galaxies. Therefore the new method recently proposed by Newman (2008) will need to be used to further calibrate the residual photo- z errors. Here, the angular cross-correlations between the HSC photo- z galaxies and WF MOS spectroscopic galaxies as a function of redshift, in combination with the auto correlation functions, are used to reconstruct the true redshift distribution of the photometric galaxy sample. Crucially, this test will only be possible if the imaging and spectroscopic fields overlap. According to Newman (2008), the photo- z bias can be reduced in this way to $\delta z \sim 10^{-4}$ over the redshift range where the WF MOS galaxies overlap with the HSC sample. Provided the photometry can be obtained in a uniform way, calibration obtained in the WF MOS region can then be extrapolated to a larger area. Thus, the overlapping in survey sky with HSC and WF MOS brings a huge benefit for improving dark energy constraints and calibrating the photo- z error contamination in HSC and other weak lensing surveys.

3.7 Proposed WMOS Surveys

3.7.1 *The International Perspective*

The outlook for cosmology has naturally been much debated throughout the global community in the subject. For the present purpose, the USA's DoE/NASA/NSF interagency task force on Dark Energy (Albrecht et al. 2006), Europe's ESA-ESO Report on Fundamental Cosmology (Peacock et al. 2006), and also the UK PPARC Dark-Energy Review (Trotta & Bower 2006) are especially important in setting the context. In general, these documents agree on the power of the BAO technique, and on the need to pursue a number of independent methods.

The Dark Energy Task Force (DETF) takes the standard approach of parameterizing the dark energy equation of state as $w(a) = w_0 + w_a(1 - a)$ and advocates a figure of merit for any given experiment that is the reciprocal area of the error ellipse in the $w_0 + w_a$ plane. This is not an unreasonable choice, but it does presume that nontrivial DE dynamics will be detected in due course, whereas the greatest immediate advance one could imagine in the field is to rule out the cosmological constant model. Until or unless this is achieved, it arguably makes sense to optimize the error on a constant w , independent of evolution. This difference in emphasis does not matter hugely in practice. Albrecht et al. define a number of stages for DE probes:

- Stage I: Current knowledge.
- Stage II: Ongoing projects.
- Stage III: Near-term, medium-cost projects, which should deliver a factor of 3 improvement in figure of merit over stage II.
- Stage IV: Long-term, high-cost projects, which should deliver a factor of 10 improvement in figure of merit over stage II. These are taken to be LSST, SKA, plus one space mission expected to emerge from the NASA/DoE JDEM process.

In the DETF lexicon, WMOS would be a stage III project, in competition with cluster surveys, supernova surveys and weak lensing surveys. The DETF and ESA-ESO reports argue that all these four principal techniques should be pursued, since one method in isolation may be limited by unforeseen systematics, thus failing to deliver the required accuracy. We agree with this multi-pronged strategy: this is one reason why it is attractive to consider both the BAO and redshift-distortion signatures as independent probes of dark energy that can be derived from redshift surveys carried out with WMOS.

Considering the years prior to the commissioning of WMOS, there will be three ground-based surveys that are capable of making interesting advances in this area:

1. The AAT WiggleZ survey, which aims to measure 140,000 redshifts over 1000 deg² between 2006 and 2010. Their redshift distribution is sharply peaked around $z = 0.6$, with a FWHM in redshift of about 0.4.
2. The VIPERS Survey of 10⁵ redshifts over $0.6 < z < 1.2$ between 2009 and 2012. This will use VIMOS to cover an area of 24 deg² to $I_{AB} < 22.5$.

3. BOSS, which is the SDSS-III campaign to measure 10^6 LRG redshifts at $z < 0.8$ over $10,000 \text{ deg}^2$ between 2009 and 2014.

The WiggleZ survey is of similar size to the VLT survey, but is more sparsely sampled; it will therefore not yield a very strong result for redshift-space distortions. Increasing the space density would push the magnitude limit beyond what is feasible with the 4-m AAOmega instrument. Conversely, the VLT survey covers too small a volume to be powerful for BAO. Large-area VLT surveys are limited by the $4 \times 7' \times 8'$ field of VIMOS, so WF MOS would have no competition in high-density surveys to 8-m depth over areas above 100 deg^2 . Of the existing ground-based projects, however, BOSS will still be extremely impressive, despite being performed with a 2.5-m telescope, on account of its huge area; BOSS will define the landscape for studies of BAO and redshift-space distortions at the time of WF MOS commissioning. WF MOS should certainly aim for a substantial improvement over what is likely to emerge from BOSS, and this can be done in two ways: size and redshift coverage, as discussed below.

In the longer term, dark energy experiments may be performed from space. Both NASA and ESA are considering projects that will yield large spectroscopic samples ($>10^8$ redshifts). At the time of writing the NASA/DoE Joint Dark Energy Mission will provide relatively low-resolution grism coverage of $20,000 \text{ deg}^2$. Likewise, ESA has under study the ambitious EUCLID project, which aims to achieve near-IR slit spectra to $H_{AB}=23$ over $20,000 \text{ deg}^2$ between 0.8 and 1.8 microns ($1.1 < z < 3.8$ for [OII] 3727 \AA emission). Most likely the ESA and NASA/DoE missions will merge in which case a 2017 launch is almost certainly optimistic. We can therefore say with some confidence that a clear competitive niche exists for spectroscopic dark-energy studies using WF MOS, provided the instrument can be constructed by 2014–2015 and its survey program completed by no later than 2018–2020.

3.7.2 Low-Redshift Survey

Summary

This survey will measure 4,000,000 galaxies within a redshift range of $0.7 < z < 1.6$ over about $3,200 \text{ deg}^2$, to a limit of $R_{AB} < 23.0$. The required time is approximately 832 hours or about 83 clear nights.

Although the section below can be read as a self-contained proposal, more technical details covering the necessary imaging for target selection, exposure times, fiber assignment statistics, sky subtraction etc., are presented in Section 6.

Performance as a BAO Experiment

The principal driver for the size of this survey is the desire to design an experiment that will constitute a significant advance in terms of BAO measurement on BOSS, which will measure redshifts for $\approx 1,000,000$ LRGs at $z < 0.8$ between 2009 and 2014. In the earlier discussion of BAO statistics, we have adopted a fiducial accuracy of 1% precision in measuring the BAO scale, i.e., an uncertainty of 5% in w

at the pivot redshift. This is the level of accuracy that BOSS is expected to deliver. A WF MOS survey can be complementary in its redshift coverage, and this motivates us to extend the spectral coverage well into the red, reaching to $z = 1.6$ for galaxies where the principal means of detection is via the [OII] 3727 Å emission line. As discussed in §6, color-based selection will enable us to cut the survey off in an efficient way at $z = 0.7$, thus probing a redshift band completely independent of BOSS. Because the distance-redshift relation is an integrated quantity, the impact of high-redshift data depends very much on the speed of evolution in $w(z)$: high-redshift measurements are important if the evolution is strong, but conversely the pivot redshift is not strongly sensitive to the upper redshift probed in cases where the dark energy is closer to a cosmological constant. A comprehensive WF MOS survey should therefore also be large enough to constitute a significant advance in the precision with which a constant w could be measured, while remaining realistic in terms of its total time requirements. We propose to set the size of the $z = 1$ survey at a total of 4,000,000 galaxies, which would push the precision on constant w down to 3%. This opens the chance of being the first to detect a discrepancy with the basic cosmological constant model. The total time requirement of under 100 nights should be attainable as a large Subaru project over 3 years, and is certainly an investment that is justified by the fundamental importance of the problem. WF MOS is a large and expensive instrument, and a BAO survey will be one of its flagship projects., being sure to retain coverage up to $z = 1.6$ to maximize complementarity with BOSS.

Performance as a Redshift Distortion Experiment

A survey of this size will also take the growth rate of fluctuations, f_g at $z=1$ into a completely new regime of precision. Present data from the VVDS (Guzzo et al. 2008) barely suffice to show that f_g is non-zero, but this is based on only 6,000 redshifts. The next step will be the 100,000 redshifts of the VIPERS project, which works to the same limit as the VVDS, $I_{AB} < 22.5$, which is very close to the limit required for the $z=1$ WF MOS BAO survey. The high surface density of these fully sampled surveys makes them especially suitable for measuring redshift-space distortions: here, the clustering anisotropy signal is strongest at small scales, and is best measured at around 20 Mpc separation, where the results are robust with respect to nonlinear effects from small-scale peculiar velocities. This contrasts with the 100-Mpc BAO feature in the correlation function, where a sparse-sampling strategy would be worth considering if we were only interested in the BAO signature. But in order to make a good job of measuring the two distinct fundamental-cosmology signatures, the number density should be kept high.

It is also important to achieve a redshift accuracy for which the radial stretching associated with measurement errors does not swamp the large-scale cosmological clustering anisotropy. At low redshift, the pairwise velocity dispersions of galaxies are about 400 kms^{-1} for blue galaxies, or 600 kms^{-1} for red galaxies (Madgwick et al. 2003). These figures are expected theoretically to show only a modest decline with redshift, and Guzzo et al. (2008) measure about 400 kms^{-1} at $\langle z \rangle = 0.8$. The equivalent 1-galaxy redshift error is $\Delta z / (1+z) = 0.0007$. Ideally, the fractional error with which we can measure the wavelength of emission lines would be smaller than this, but this is not essential. The reason for this is

that the physical peculiar velocities cannot be predicted exactly from theory in any case: they have to be treated as a nuisance parameter, to be estimated empirically. If the total effective pairwise dispersion is increased by redshift errors, then this has little impact on the overall S/N with which f_g can be measured, as long as the change in effective total velocity dispersion is not gross. The empirical accuracy of VVDS redshifts is an rms $\Delta z = 0.0012$ between repeated measurements, and we would expect WF MOS surveys to do rather better than this, because the spectral resolution will be about 10 times better than that of VVDS. The rms wavelength error with which it is possible to centroid a spectral line of rms width σ is just $\Delta\lambda = 2^{1/2} \sigma / \text{SNR}$, thus depending on the signal-to-noise with which the line is detected. This will be a minimum of about 5 for a secure detection, and so the fractional precision in wavelength should be 0.0001 or better, adopting our default resolution of $R = 3500$. This minimal figure can be increased by calibration errors, of course, but in practice keeping these to the $\Delta z = 0.001$ level should not be difficult.

Overall, then, we can predict the precision in f_g that is expected from the WF MOS $z = 1$ survey straightforwardly by scaling from the projected performance of VIPERS, which in turn is based on simulations grounded in the VVDS experience. The error in f_g scales as $V^{-0.5} n^{-0.44}$ in terms of the survey volume V and number density n . The VLT work will cover $0.5 < z < 1.2$ with 100,000 galaxies over 24 deg^2 , and is predicted to yield an error of 0.07 in f_g . A WF MOS survey of 4,000,000 galaxies covering $0.7 < z < 1.6$ should thus improve this by a factor 5, yielding an expected precision on f_g of about 0.02 in 2 independent redshift bins around $z = 1$ (see Figure 3-17).

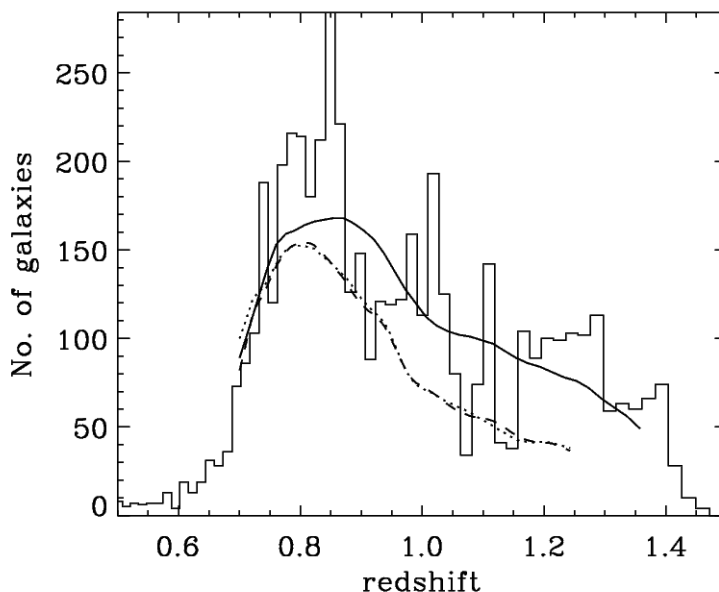


Figure 3-15: The redshift distribution of DEEP2 galaxies derived via multicolor selection in BRI space (Coil et al. 2004). The cutoff at $z = 0.7$ results from the photometric preselection, whereas that at $z = 1.4$ reflects the red limit of DEEP2 spectroscopy. The two lines are alternative models for the selection function.

Practical Issues of Sample Selection

We begin by recapitulating the arguments that specify the depth of the sample in order to attain good BAO performance:

1. Volume density. $nP = 1$ is optimal for power spectrum measurement. We adopt a canonical $P = 2500 \text{ h}^{-3} \text{ Mpc}^3$ at wavenumber $k = 0.1 \text{ h Mpc}^{-1}$, motivated by a correlation function scale-length of $3.5 \text{ h}^{-1} \text{ Mpc}$ and slope $\gamma = 1.9$ as measured for VVDS. Very similar parameters apply for $z = 3$ Lyman-break galaxies. This specifies a target number density of $n = 0.0004 \text{ h}^3 \text{ Mpc}^{-3}$. At face value, a larger figure is required in order to achieve accurate measurement of power at larger wavenumbers; even though the BAO signal is concentrated at $k < 0.1$, understanding of nonlinear systematics will be critical, and we wish to retain the ability to measure the power in this regime accurately. However, the degradation in performance at a factor 2 below optimum density is minor, and so we believe that $n = 0.0004 \text{ h}^3 \text{ Mpc}^{-3}$ is a sensible target.
2. With a default $\Omega_m = 0.25$ flat cosmology, this corresponds to a desired surface density of galaxies in the range $0.7 < z < 1.6$ of 1245 deg^{-2} . We emphasize that this should be the density of *actually achieved* redshifts in this range. For a survey size of 4,000,000 galaxies, this corresponds to a total area of 3200 deg^2 .
3. Since our simulations (Section 6) show that the best attainable fiber allocation completeness figures in practice will be about 80%, the surface density of required targets rises accordingly. We show below that a further 20% of targets will probably have too weak lines to yield a redshift. Allowing for these two inefficiencies, we require an input surface density of galaxies in the range $0.7 < z < 1.6$ of 2132 deg^{-2} .

The $z = 1$ band is has been thoroughly explored to the depth of interest by the DEEP2 survey, and it seems sensible to build on the experience of the DEEP2 team with color-based selection of a redshift band at the depths of interest. As described earlier, the low redshift survey will cover the redshift range of $0.7 < z < 1.6$, and the bulk of our survey will consist of emission line galaxies.

Figure 3-16 shows the redshift distribution of DEEP2 galaxies derived to a limit of $R_{AB} < 24.1$ (Coil et al. 2004). Multicolor selection in BRI space was applied, and a sharp cutoff at $z = 0.7$ was achieved, such that about 95% of selected galaxies did in fact exceed that desired threshold. The DEEP2 number counts are given in Table 3-1 (all mags are AB). We choose to select in R both because this is near the center of the spectral range, and also to exploit the DEEP2 experience.

Table 3-1: DEEP2 Galaxy Number Counts

R mag range	R_{lim}	N/deg^{-2}	$N(21 < R < R_{lim})$
24.0–24.5	24.5	25,700	70,700
23.5–24.0	24.0	17,000	45,000
23.0–23.5	23.5	11,200	28,000
22.5–23.0	23.0	7,100	16,000
22.0–22.5	22.5	4,600	9,700
21.5–22.0	22.0	3,100	5,100
21.0–21.5	21.5	2,050	2,050

The surface density of galaxies that satisfy $z > 0.7$ according to the DEEP2 color cuts is approximately $15,000 \text{ deg}^{-2}$ to $R_{AB} < 24$, declining to about 900 deg^{-2} for $R_{AB} < 22.5$. Our desired density of 2132 deg^{-2} thus requires a limit of

$$R_{AB} < 23.0 \quad (28)$$

Although we have deduced this figure from first principles, it is rather close to the limit suggested for the $z = 1$ survey in the feasibility study.

To a given magnitude limit, the majority of the selected galaxies are blue emission-line objects. The alternative class is the Luminous Red Galaxies (LRGs), but these are much rarer. Again based on the DEEP2 results, a surface density of LRGs comparable to that of blue galaxies at $R_{AB} < 22.7$ requires $R_{AB} < 23.6$. These objects will be more strongly clustered than the blue population, but not by as much as one might first think. Local studies (e.g., Norberg et al. 2002) indicate that clustering increases both with color and with luminosity, and we are already selecting the relatively rare luminous subset of the blue population. Probably the additional color selection would amount to a further relative bias factor of approximately 1.5, which does not have a large impact on SNR if we are near $nP = 1$. As seen below, the extra integration time needed to access the LRG population means that they are not competitive probes.

Over a 1.5-degree field, the range of densities discussed here corresponds to 3400 targettable objects per field. The number of required positioner elements depends on the number of multiple visits per field. The most efficient way of covering area is with a single visit, so that more than 3400 would never be required. For a single visit, the completeness would be lower than the canonical 80%—more like 50%. But most of the efficiency gains come when going from single to double coverage per pointing. Thus, at minimum there should be sufficient fibers to match the target number in two visits, i.e., 1700. To secure our final observing requirement we adopt a strategy of re-observing 20% of the fields, selecting those with the worst completeness. This boosts the average completeness and has the benefit of allowing repeated fields to be useful as a check on systematics. To reach our goal of 4 million galaxies, assuming a 80% successful redshift fraction, we need 2380 fields of which 473 are measured twice. Further details supporting this strategy are presented in Section 6.

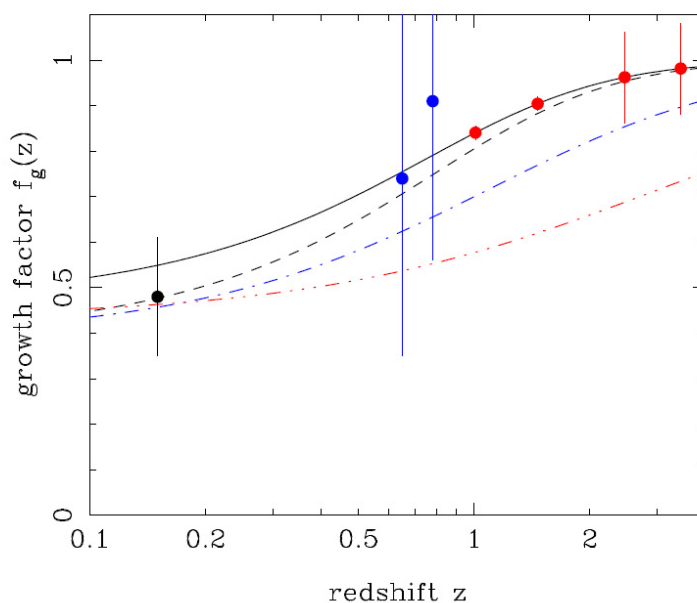


Figure 3-16: A plot of the growth factor $f_g(z) \equiv d \ln \delta / d \ln a$ against redshift for various models. The solid black line shows the standard $\Omega_m = 0.25$ Λ -dominated model, and the dashed black line shows the same expansion history but with the stronger DGP-style dependence of growth on $\Omega_m(a)$: $f_g(a) = \Omega_m(a)^{0.68}$. The blue dot-dashed line shows the DGP model itself (with $\Omega_m = 0.25$ today) and the red treble-dot-dashed line shows the behavior for a standard open $\Omega_m = 0.25$ model without dark energy. The three points at $z < 1$ are (in order of increasing z): 2dFGRS (E. Hawkins et al., 2003, MNRAS 346, 78); 2SLAQ LRGs (N. Ross et al., 2007, MNRAS 381, 573); VVDS (Guzzo et al. 2008). The points at higher redshift show the predicted performance from our proposed WF MOS surveys: 4×10^6 galaxies at redshift $z \sim 1$ and 10^5 LBGs at $z \sim 3$ (each split into two redshift bins).

3.7.3 High-Redshift Survey

A high-volume, high-redshift (i.e., $z = 3$) BAO survey, such as that proposed in the Feasibility Study, would offer an important complement to the $z = 1$ survey, improving constraints on evolution of dark energy to high redshift. We have concluded, however, that because of the observing time expense and for sound strategic reasons related to the unknown nature of dark energy, it is premature to define a required high-redshift survey. In lieu of this, we will make it a requirement that the instrument be designed to be capable of such a survey. We describe such a survey below. As before, details on target imaging and exposure times are available in Section 6.

A high-redshift survey would use Lyman-break galaxies, chosen using a Steidel-like *UGR* selection. In the redshift band $2.5 < z < 3.3$, the volume per unit area is somewhat larger than the figure for the low-redshift band, so the optimal target density is approximately 1600 deg^{-2} , or 2800 objects per 1.5-degree field. This density of targets corresponds to a magnitude limit of $R_{AB} < 25$. The number of fibers required follows the same logic as the $z = 1$ survey: one might contemplate strategies between double visits for a low density to single visits at the maximum density. This suggests a compromise figure for the total

number of positioner elements near the $z = 3$ minimum. A total of 1400 would allow the $z = 1$ survey to be executed very well – and we shall argue below that this is probably the more important redshift band.

How large a $z = 3$ survey would be required? We have been using the current precision on constant w of 5% as a target, which implies a volume of $5 (h^{-1} \text{ Gpc})^3$. Thus the natural figure is 2,000,000 galaxies, or an area of 1570 deg^2 . Here, the agreement with the Feasibility Study is not so good. Their proposal was for a survey of 600,000 galaxies, using a slightly brighter limit: $R_{\text{AB}} < 24.5$. The claim for this survey was an accuracy of 1.5% in $D(z)$, or 7.5% in w . The difference is that we prefer to make the more conservative assumption that one cannot work to higher k_{max} at higher redshift, which is how the Feasibility Study was able to obtain such a good accuracy for a relatively small sample. The results from the Millennium Simulation shown above certainly cast doubt on this optimistic approach: although the nonlinearities in the mass distribution are lower at $z = 3$, the nonlinearities in the *galaxy* distribution seem to be higher.

Our main issue with the $z = 3$ survey proposed in the FS is that it is much more expensive in terms of time than the $z = 1$ survey for the same precision on w , and that it does not deliver a large increase in pivot redshift (as discussed earlier). We therefore envisage a staged approach consisting of an initial redshift-distortion survey of 100,000 galaxies to constrain the growth of structure. Only 35 nights would be needed for a survey of 100,000 Lyman-break galaxies at $z = 3$. Although redshifts of galaxies at this distance are slow and expensive to obtain relative to the $z = 1$ band, in terms of redshift space distortions this will be unexplored territory, and so even 10^5 galaxies in 35 nights would transform the observational situation regarding constraints on f_g in this regime. Scaling from the projections of VLT VIPERS project, this would yield an expected precision on f_g of about 0.1 in 2 independent redshift bins around $z = 3$, as compared to errors of about 0.02 for the larger $z = 1$ survey (see Figure 3-17). Depending on progress in our collective understanding of dark energy, this could be extended subsequently for a more ambitious $z = 3$ BAO project.

The high redshift survey target allocation efficiency will be similar to the low redshift survey. Angular clustering will be less, however, so we dispense with the two-tier observing strategy and instead rely on a single observation per field at an average completeness of 67%. The result is that 69 fields must be observed to reach 10^5 galaxies.

3.7.4 Requested Time

We now review the observing time required for the proposed surveys. Much of the technical discussion essential to understanding our conclusions is deferred to Section 6. Therein we find an integration time of 15 minutes is sufficient to locate and recognize [O II] emission in the $z \sim 1$ survey. This has the benefit that overheads for acquisition and readout are negligible in comparison, so that one could access four fields per hour. For the $z \sim 3$ survey, the associated integration time is 4 hours, so one can access two fields per night.

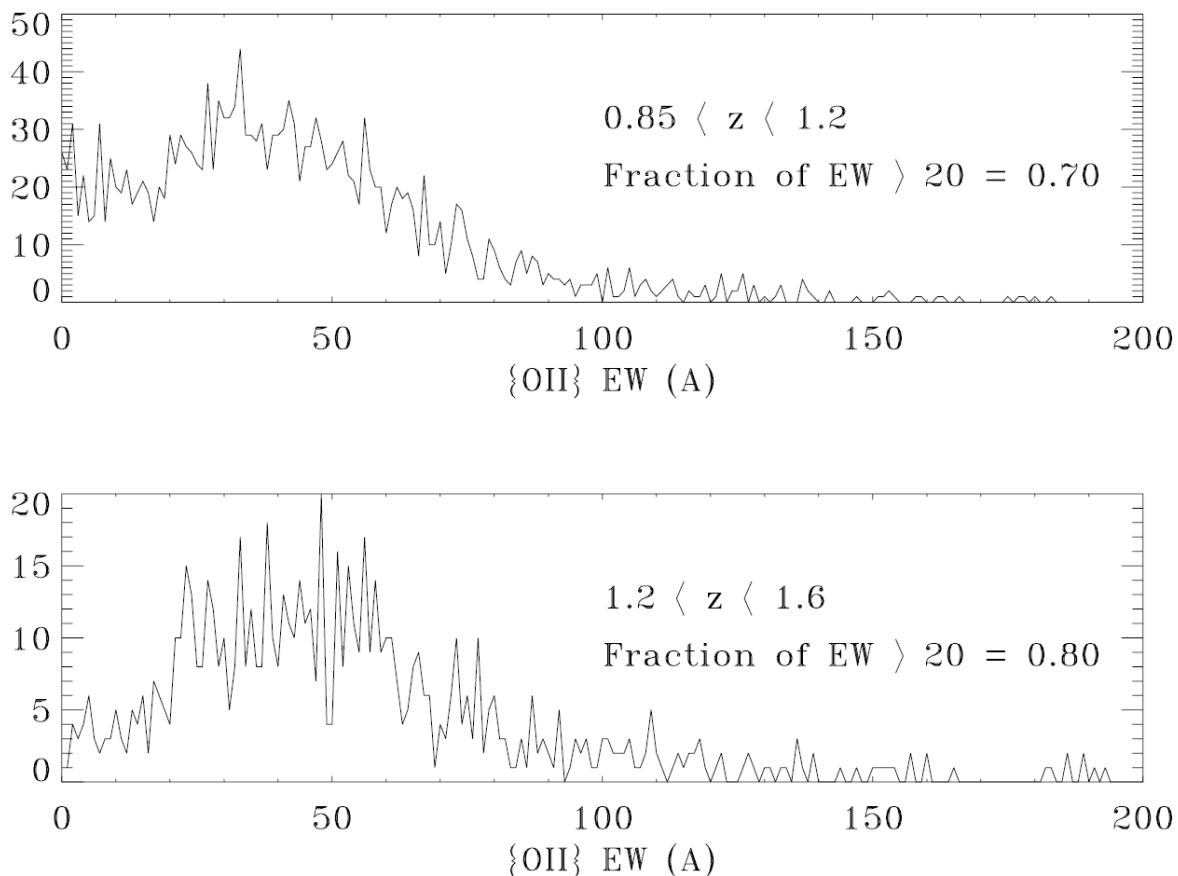


Figure 3-17: Histograms of the equivalent width of [O II] 3737 emission line derived from DEEP2 galaxies in two different redshift bins. This indicates that an 80% redshift success rate will be achieved for the $z = 1$ survey provided a line of equivalent width as small as 20\AA can be reliably detected.

Spectroscopic redshift determination for the low redshift survey will be provided by the [OII] 3727\AA doublet, demanding an observed wavelength range of approximately $6330\text{--}9700\text{\AA}$. The use of broadband color information to predict [OII] equivalent widths ahead of spectroscopic observations is discussed in Section 6. There are no strong constraints on completeness other than what is necessary to maximize survey efficiency. A resolution of $R \sim 3500$ allows identification of the [OII] doublet and sufficient velocity precision for both BAO and RSD applications. In Section 6 we show that a signal to noise ratio greater than 7 on the emission line is achievable for blue galaxies with $R_{AB} = 23.0$ in our planned exposure times and will reduce the fraction of incorrectly determined redshifts to less than 1%. Similarly, for the $z = 3$ LBG objects, $S/N = 4$ can be obtained for $R_{AB} = 25$ in 4 hours. Given the strength of spectral features in these objects, simulations discussed in §6 suggest this is adequate. For LRGs with $R(AB) < 23.6$, however, we only obtain $S/N = 3$. This is insufficient for absorption-line redshifts; the feasibility study set a target of $S/N = 10$, which seems realistic, and this would surely not be attained in 4 hours integration. Thus targeting this population seems inefficient.

These figures yield the following requirements in terms of clear 10-hour nights in order to execute the surveys we have described, assuming 1400 fibers per field:

- $z = 1$: 832 hours / 83 nights (4,000,000 redshifts)
- $z = 3$: 286 hours / 29 nights (100,000 redshifts)

Of course, for faint objects, spectroscopic quality is more often limited by fidelity of sky subtraction. The ‘nod-and-shuffle’ technique was developed at the AAO to improve the normal indifferent performance of subtraction when using fibers, and it works very well. However, this improvement comes at the cost of a factor 4 in integration time for a given S/N: this factor is not included in the above time estimates. Given that the required exposure times are already long, it is clear that nod-and-shuffle has to be considered unacceptably expensive for the surveys under discussion here. In Section 6, we show, via simulations, that the principal component technique introduced by Wild & Hewett (2005) can dispose of sky residuals in SDSS spectra, given a large enough library of sky spectra. We thus propose to dispense with the inefficient ‘nod and shuffle’ technique.

Even given clean spectra of the desired S/N, one problem that will be faced by WF MOS surveys (and all competing spectroscopic dark-energy probes) is achieving high fidelity in assigning correct redshifts. The problem of emission-line identification in the context of the DEEP2 project is described by Kirby et al. (2008). There are four principal lines visible in galaxy spectra at intermediate redshift: $H\alpha$ (6563), [O III] 5007, $H\beta$ 4861, [OII] 3727. For the spectral setup proposed here, these are visible in the redshift ranges 0–0.5, 0.27–0.94, 0.30–0.99, 0.7–1.6. For $z > 1$, therefore, we will rely on [OII] 3727 to determine redshifts; at lower redshifts, some cases will show several lines, but only one may be detected at lower signal-to-noise. It is clearly essential that the line be correctly identified, since otherwise there is the potential for systematically transcribing a copy of the density field to an incorrect distance. Such “line-locking” could have potentially serious consequences for the BAO test, since it would alter the estimated acoustic scale in a systematic way. As an illustrative example, suppose we had a shell of galaxies at $z = 0.8$ emitting in $H\beta$; if the line is misidentified as [OII] 3727 at $z = 1.35$, this raises the inferred comoving distance by nearly 50%. Making this error in only 2% of cases then holds the potential (depending on the exact method used) of perturbing the acoustic scale by 1%, which is the signal of cosmological interest. The correct line identification can be derived via a combination of resolving the OII doublet (required resolution $R > 1340$) and using photometric redshifts to reject incorrect candidate redshifts. In DEEP2, the failure rate in this process is at the dangerous 2% level, and WF MOS surveys will need to do better. This is not a severe challenge, since DEEP2 worked with BRI photometry, and we can expect to have superior photometric data (Section 6).

3.8 Summary of Survey Strategy for Dark Energy and Modified Gravity

In the foregoing sections, we have discussed the two main signatures of fundamental cosmological importance that one can expect to detect in large galaxy redshift surveys using WF MOS: Baryon Acoustic Oscillations as a standard ruler, and Redshift Space Distortions as a measure of the growth rate of density

fluctuations. In both cases, the optimal kind of survey to perform depends on exactly what kind of deviation from orthodoxy we think is most likely, but some useful general points have emerged. The case for a high-redshift survey seems stronger from the point of view of redshift-space distortions, where the independence of data at $z = 1$ and $z = 3$ is substantial. Conversely, the BAO constraints from a $z = 3$ survey are only substantially different from those of a survey at $z = 1$ in the case of dark energy whose properties evolve strongly at high redshift. Until we are able to reject the simple $w = -1$ cosmological constant, the high expense of a $>1,000,000$ -redshift survey at $z = 3$ seems difficult to justify.

Based on these considerations, plus the need to deliver a substantial advance on datasets likely to be available at the time of WF MOS commissioning (principally the 1,000,000 LRG redshifts at $z < 0.8$ expected from BOSS), we have evolved a strategy that proposes two surveys of rather different size and cost:

1. 4,000,000 galaxies at $0.7 < z < 1.6$ over about 3200 deg².
2. 100,000 galaxies at $2.5 < z < 3.3$ over about 100 deg².

The first survey should require about 83 nights; the second about 29. The cosmological constraints from the high-redshift survey will be less strong, but will represent a step into novel territory as far as growth-rate measurements from redshift-space distortions are concerned. The larger $z = 1$ survey will measure growth rates much more accurately, and will also deliver dark energy constraints from the BAO method that will be at least a factor 2 better than any competition, especially at the upper end of its redshift range. Both these datasets will have substantial applications in astrophysical aspects of galaxy clustering. At a cost of 30–40 nights per year over 3 years, these surveys seem realistic as major flagship projects for WF MOS and Subaru.

4 STELLAR ARCHAEOLOGY AND GALAXY GENESIS

4.1 Science Case

4.1.1 Overview

The origin and evolution of galaxies like the Milky Way and M31 remain among the key unanswered questions in astrophysics. The galaxies we see within the Local Group are valuable representatives of the extragalactic population and have been evolving for the majority of cosmic time. As our nearest neighbors they can be studied in far more detail than their distant counterparts, and hence provide our best hope for understanding star formation and prototypical galaxy evolution (Freeman & Bland-Hawthorn 2002). Although significant observational progress has been made, we are still a long way from understanding the details. Detailed large area spatial, kinematic and chemical surveys of nearby stellar systems will provide the essential link with results from the high redshift Universe. Λ CDM cosmologies predict that hierarchical merging of dark matter haloes is the main driver in galaxy formation and evolution; indeed the discovery of the tidally-disrupted Sagittarius dwarf (Ibata et al. 1994) provided the first compelling nearby evidence. However, the detailed process by which large galaxies such as the Milky Way arrive at their current state is still largely speculative (e.g., Abadi et al. 2003, 2006; Bullock and Johnston 2005; Font et al. 2006).

Current large scale spectroscopic surveys such as RAVE (Steinmetz 2003) and the M31 kinematic surveys on Keck (Ibata et al. 2005; Guhathakurta et al. 2005) highlight the potential of multi-object spectroscopy to probe the structure and properties of the Galaxy and M31 at modest resolution, while FLAMES on the VLT provides a compelling argument for the multiplexed use of mid- to high-resolution spectroscopy, particularly in understanding nearby dwarf galaxies (Tolstoy et al. 2004). However, although FLAMES is producing exquisite spectra of hundreds of objects, its surveys are still at least an order of magnitude short of the requirements necessary for a complete analysis of the Galaxy and M31.

Each of the above efforts is necessarily limited in either coverage or depth. While future proposed Galactic surveys such as the Bulge with AAOmega (PI Freeman: proposed) and the ESA cornerstone space mission Gaia (Perryman et al. 2001) will go some way to alleviate this problem for the Galaxy, they still leave unexplored a huge volume of parameter space that holds the key to full understanding of Galactic evolution.

The diversity of current and planned surveys illustrates the scientific importance and community interest in this field and WF MOS presents a unique opportunity for a major advance in our understanding of the origin, chemical evolution and mass assembly of nearby galaxies. The key advantages of WF MOS over existing 8m-class facilities are the greater multiplexing and wavelength coverage together with the much larger field-of-view. This provides enormous leverage in Galactic studies by enabling a range of structural probes in multi-parameter space sensitive to both dynamical and chemical properties.

Two of the key challenges facing modern astrophysics are our understanding of the fundamental *nature and properties of dark matter*, and of the inter-related *complex baryonic processes* that led to the formation of galaxies like the Milky Way. Although dark matter likely guides the gaseous matter into proto-galactic environments, baryonic physics governs processes on small scales, through cooling, collapse and star formation. The role of both the dark and baryonic components can be simultaneously addressed with large-scale WF MOS surveys of the stellar components of the Milky Way and companion galaxies. In addition to providing tests of cosmological models on low mass scales, such surveys will also unravel the complex process of hierarchical formation wrapped within various Galactic structures. These studies directly complement the dark energy aspects of this document, and taken as a whole WF MOS will provide a new window on all three major energy constituents of the Universe.

Galaxies are dynamically and chemically inhomogeneous; only by using the higher dimensionality afforded by combining kinematic and chemical measures can a full understanding of their constituent parts be achieved. The fossil record of past events is recorded in the spatial distribution, kinematics and chemical fingerprint of individual stars. As an illustration of the complexity of the Milky Way, Figure 4-1 shows the state of the art in tracing substructure in the Galactic Halo from large area photometric surveys. Several giant streams (up to ~ 60 degrees long) from disrupting globular clusters and satellite dwarf galaxies criss-cross the halo providing valuable probes of both the nature of dark matter and the gravitational potential of the Galaxy.

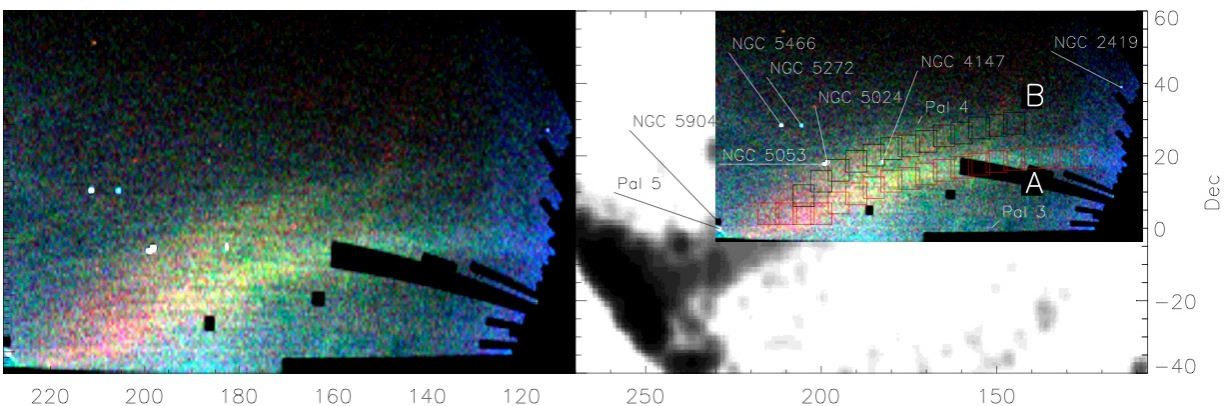


Figure 4-1: The field of Streams from Belokurov et al. (2006) showing SDSS stars having $(g-r) < 0.4$ for a region around the North Galactic Cap. Colors denote depth along the line-of-sight with red being the most distant objects at $d \sim 50$ kpc and blue the nearest at $d \sim 10$ kpc. The right-hand panel shows a composite including the 2MASS M-giant distribution from Majewski et al. (2003). Several streams are readily visible.

4.1.2 Redesigning the Galactic Archaeology (GA Surveys)

To address the nature of dark matter and the baryonic processes we must obtain both kinematic and chemical signatures of large populations of stars. A low resolution survey will yield the kinematics and

chemical abundances of stars over a large volume, and an overlapping higher resolution study will uncover more detailed patterns in their stellar chemistry¹. The synergy of two such Galactic surveys will provide the most detailed picture of the processes that formed our Galaxy and of the nature of its constituents.

Although the Feasibility Study provided an excellent starting point in highlighting the huge potential gains available for Galactic science, the ambitious nature of that program led to a rather imbalanced set of proposed surveys. After independently reassessing the science goals and the technical requirements needed to meet them, we have concluded that the approach adopted in the Feasibility Study is not optimal.

The science drivers for Galactic Archaeology (GA) with WF MOS still naturally split into two components:

- Low resolution (LR) kinematic and general abundance analyses of Galactic dynamical structure;
- Detailed high resolution (HR) analyses of constituent populations to trace temporal chemical development;

but the detailed strategy within each is somewhat different.

4.1.2.1 LR Survey

The LR mode will focus upon obtaining accurate kinematics and metallicity measures for a large stellar sample. In this mode, the main Galactic survey science for WF MOS ($15 < V < 20$) is complementary to the Gaia ($V < 15-17$) and RAVE ($V < 12$) large area surveys. Gaia synergy is especially important since for both full kinematic and HR abundance analyses, good distances and accurate proper motions are required. Matching the LR survey depth to that of Gaia, i.e., to $V \sim 20$, is thus a sensible approach.

Good velocity accuracy is essential for identifying streams and substructure against the Galactic background population. As an example, the required velocity errors for 3-sigma detection of streams for an n-dimensional kinematic survey are:

$$\epsilon = \frac{\sigma}{3} \times \frac{1}{N^{1/n}}$$

where σ is the dispersion of the background population, and N is the number of streams (e.g., Helmi & White 1999). For a survey limited to radial velocity information this implies that errors of ≈ 0.1 km/s are required to locate halo streams in the Solar neighborhood (assuming $\sigma = 100$ km/s and $N = 500$; Wilkinson et al. 2005). Adding proper motions improves this dramatically, implying required errors of about ≈ 4 km/s for Halo substructure. For disk streams the radial velocity error would need to be ≈ 2 km/s.

¹ It should be noted that while Gaia will revolutionise this field, it will not provide detailed abundances and accurate radial velocities to fully explore Galactic history. WF MOS will thus fully complement the Gaia and significantly enhance its scientific impact.

Satellite galaxies have velocity dispersions in the range 6–12 km/s whilst star clusters range from 1 km/s (open clusters) to 10–20 km/s (massive globulars). As the velocity dispersion of tidal tails of disrupting systems reflects that of the progenitor, detecting and analyzing dissolving clusters therefore also requires errors of a few km/s. Additional complications arise from the smooth foreground population (e.g., Brown, Velazquez & Aguilar 2005) against which it is harder to pick out substructure. Abundance measures will help differentiate substructure and again velocity errors of ~ 2 km/s are necessary.

An efficient mid-resolution ($R=5000$) spectroscopic survey, comparable to FLAMES in LR mode, will deliver velocities to the required ~ 2 km/s precision and also provide proxy $[\text{Fe}/\text{H}]$ measurements to 0.1 dex via the Mgb and Calcium triplet (CaT) diagnostics. Although data of this resolution will not provide accurate evidence of more exotic α -, r- and s-process element measures for individual stars, it alleviates the need for an unfeasibly large HR sample. It would also enable the tracing of the dissolution and tidal debris from clusters (where km/s precision is needed) and detailed studies of halo substructure and the nature of dark matter.

Similar reasoning holds for surveys of the M31 and M33 galaxies. The current ongoing surveys sensibly make use of modest resolution spectrographs to derive both kinematic and population-averaged overall metallicity measures. It is now well known (e.g., Tolstoy et al. 2004) that individual velocity and $[\text{Fe}/\text{H}]$ parameters are required to unravel the complex star formation histories in dwarf galaxies. The same will inevitably be true for their giant neighbors. A further possibility, as evidenced by Kirby et al. (2008), is that by combining spectra from similar kinematic components, modest $R=5000$ resolution spectra, but at high signal:to:noise, could be used to extract additional chemical information, such as α -element ratios, by being more creative with analysis tools such as ICAs or specifically trained ANNs (e.g., using currently available FLAMES spectra) to extract this information.

In contrast to the above, the LR survey proposed in the Feasibility Study case offered a velocity precision of ~ 10 km/s which we believe is too coarse to detect tidal streams and accurately assign population membership. At the low resolution proposed, accurate equivalent width (EW) estimation is also impractical. In our case, a resolution of $R=5000$ in the Mgb and CaT regions opens up the parameter space significantly given spectra of reasonable signal/noise. We will achieve a velocity precision of a few km/s, $[\text{Fe}/\text{H}]$ estimation to 0.1 dex and constraints on α -element ratios. This is a much better match to the impressive Gaia datasets about to be delivered.

4.1.2.2 HR Survey

While the original Feasibility Study proposed a HR mode with $R = 40,000$ - $50,000$ with very limited wavelength coverage, we are proposing a much larger simultaneous wavelength coverage but at a resolution of $R = 20,000$. We have arrived at this conclusion by examining the extraction of chemical abundances from degraded high resolution spectra (Irwin and Lewis 2009; in prep.), and studies with VLT FLAMES, Keck HIRES and MIKE Magellan. These collectively demonstrate that `chemical

tagging' at $R = 20,000$ is feasible and by focusing on redder wavelengths (4800--6800 Å) than those highlighted in the Feasibility Study, studying a million stars is a practical proposition.

Our proposed HR surveys will yield data similar to the VLT FLAMES/GIRAFFE instrument operating in its in HR mode (where we already have built up a lot of experience), but with the considerable advantage of covering the full wavelength region of interest (4800–6800 Å) in a single exposure. By working in the “visible” regime, line blending is lessened. A good example is provided by the forbidden oxygen line $[OI]_{6300.3}$, shown in Figure 4-2 from a 5400s VLT-FLAMES $R=20,000$ spectrum of a metal-rich Bulge giant. Although the $[OI]$ line is half-blended with $ScII_{6300.7}$, it is still sufficiently distinct to quantify using multi-component profile fitting.

The advantage of contiguous wavelength coverage over 4800–6800 Å is access to a dozen FeII lines and more than a hundred FeI lines from which accurate stellar atmosphere parameters can be determined: effective temperature; surface gravity; metallicity and microturbulent velocity; using excitation and ionization equilibrium and known curves-of-growth. The most important elements for chemical tagging all have measurable lines in this region. The availability of parallaxes from Gaia and broadband optical and near-infrared photometry will also play a significant role in this detailed stellar atmosphere modelling.

Combined with the 5- to 10-fold increase in target allocation this produces a 25- to 50-fold increase in survey efficiency over the VLT, enabling a range of GA projects that would be impractical with current instruments.

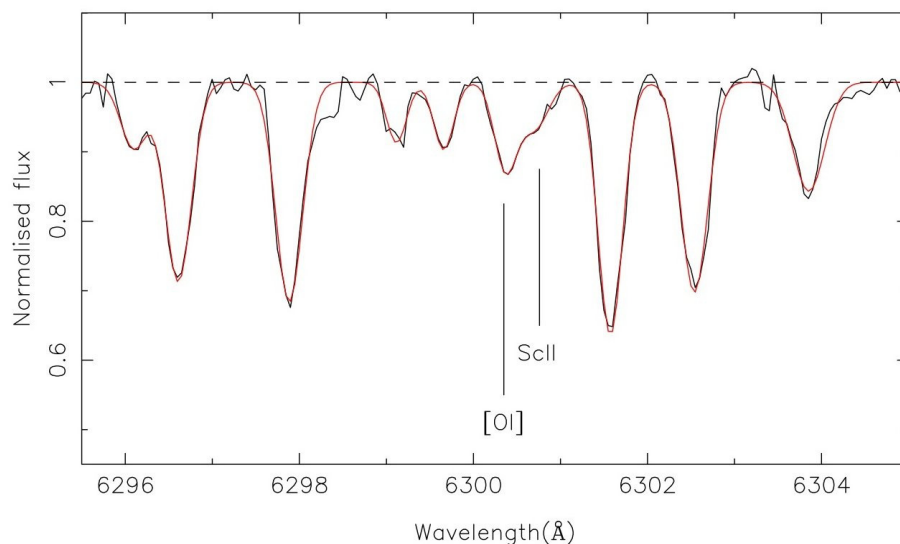


Figure 4-2: The region around the $[OI]_{6300}$ line from a 5400s VLT-FLAMES exposure at $R=20,000$ of a metal-rich, $[Fe/H] = -0.41$ Bulge giant with $S:N \sim 200/\text{Å}$. An unconstrained multi-component Gaussian model fit of the most prominent lines is shown overlaid in red.

As an illustration of why $R = 20,000$ is sufficient for our purposes, we compare the model fit secured using the data shown in Figure 4-2, with that obtained at a similar signal/noise at $R = 50,000$ using the red arm of VLT-UVES and the same overall exposure time. A comparison of the unconstrained model fit parameters with the visually measured and identified lines, shown in Table 4-1, demonstrates that automatic model fitting at $R = 20,000$ can give comparable results to visual interpretation of a much higher resolution spectrum and that EWs to better than $5\text{m}\text{\AA}$ precision can be obtained. The main limitation for such metal-rich stars is not partially unresolved lines but the continuum placement. Here the error in continuum placement is about ~ 0.01 in normalized units leading to a typical EW error due to this alone of about $3\text{m}\text{\AA}$. Further improvements in the model fitting are also possible by constraining the relative wavelengths, particularly of blended lines.

A further significant advantage of a resolution of $R = 20,000$ is that by adopting a low order cross-dispersed spectrograph design it is feasible to do quantitative spectrophotometry over large extended spectral regions. This is difficult in conventional echelle-mode instruments and can be used, for example, to tie in measurements of spectral indices (often all that is available for distant galaxies) with detailed line analysis. As an example, the Lick indices of Mg2, Fe₅₂₇₀, Fe₅₃₃₅ are widely used in extragalactic work (e.g., Worthy et al. 1994) and require fluxed spectra covering a wide spectral range. To measure the Mg2 index at $5156\text{--}5197\text{ \AA}$ requires continua defined at $4897\text{--}4958\text{ \AA}$ and $5300\text{--}5366\text{ \AA}$ therefore requiring contiguous coverage from 4897 \AA to 5366 \AA . A large spectral coverage also makes it feasible to analyze the extended wings of the Balmer lines to derive more accurate effective temperatures and surface gravities.

Table 4-1: FLAMES-GIRAFFE $R=20000$ EWs compared to UVES $R=50000$

	λ	FLAMES		UVES
		EW(m \AA)	FWHM (\AA)	EW(m \AA)
Fel	6297.84	122.19	0.36	123.2
OI	6300.32	39.99	0.30	41.4
ScII	6300.65	26.80	0.38	25.4
Fel	6301.53	128.92	0.33	126.9
Fel	6302.49	117.73	0.36	101.0
TiI	6303.81	72.33	0.43	79.5

We also note that absolute flux calibration is not necessary since it is straightforward to use extant photometry to provide the conversion from relative to absolute fluxes and thence spectrophotometry.

4.1.2.3 Summary of GA Survey Requirements

The above considerations lead to a well-defined set of technical requirements for the GA science goals. Noting the kinematic synergies with Gaia, these are summarized in Table 4-2.

Table 4-2: Summary of the Galactic Archaeology Requirements

LR survey to $V = 20$ (distances, proper motion, radial velocity, [Fe/H])	
HR survey to $V = 17$ (uniqueness of abundance analysis for chemical tagging)	
LR	(Extent of halo, ancient streams, disk structure, Fe/H) Velocities to ~ 2 -3 km/s, [Fe/H] to ~ 0.1 dex, ~ 2400 fibres R = 5000, Call triplet 700\AA from 8150 - 8850\AA & Mgb region 4800 - 5500\AA Npix = 2×2000 , $V < 20$, 0.5hr exposures 2000 deg^2 , $\sim 3 \times 10^6$ stars, 765 hours
HR	(Chemical tagging of elements, IMF, SF history) R = 20000, covering 4800 - 6800\AA , Npix = 20000 $V < 17$, 1hr exposures 2000 deg^2 , $\sim 10^6$ stars, 1125 hours FWHM 3 pixels, pitch ~ 8 pixels, ~ 600 fibres

4.1.3 Addressing the Big Questions

We now develop a fuller account of the science case for our two surveys.

Low Resolution (LR) Survey: This will result in a detailed kinematic and general abundance map of the Galaxy for which WF MOS depth and areal coverage are crucial. The major scientific goals for this survey are:

What is the nature of dark matter?

While our understanding of dark matter appears to be adequate on cosmological scales, its application is being challenged on the scale of individual galaxies. The WF MOS survey will focus on several crucial galactic-scale properties of dark matter. These are:

- The mass and extent of the MW dark matter halo:

The shape of the dark matter halo of the Galaxy is a consequence both of its formation history and the very nature of dark matter itself, and the Milky Way is the one massive spiral galaxy in which we can hope to map out the distribution of dark matter in fine detail. However, the majority of kinematic tracers currently available are tied to the Galactic disk, and the shape of the overall potential is very poorly constrained. Recent advances using tidal streams have met with some success (e.g., Fellhauer et al. 2006), although the paucity of data has ensured that arguments over the shape of the dark matter distribution in the Milky Way persist. Little progress will be possible until after Gaia as beyond 50 kpc there are currently only a few tens of tracers (dwarf galaxies, globular clusters, halo stars; e.g., Wilkinson & Evans 1999; Battaglia et al. 2005). Gaia will provide a few thousand objects out to 60kpc, but WF MOS will push the radial velocities much further out (to $V = 20$ where there will still be proper motion constraints from Gaia); WF MOS will also measure velocities for high luminosity carbon stars, AGB stars and TRGB

stars to distances to 250 kpc, with several tens of objects expected in a 1000 deg² survey - Gaia will provide proper motions for these stars out to 60–80kpc. These new tracers will make it possible to place significantly stronger constraints on the mass and extent of the Milky Way halo, as well as enabling a detailed study of the velocity distribution of halo stars. Furthermore, WF MOS observations of the disk of the Milky Way will provide a detailed characterization of the mass distribution close to the Galactic Plane, and it will be possible to investigate whether the Galaxy has a central cusp or core in its dark matter distribution. Since cusps are a generic prediction of galaxy formation in Λ CDM cosmologies, the existence (or lack thereof) of dark matter cores is a fundamental probe of our underlying cosmological ideas. Current data on the Galactic rotation curve and microlensing optical depth suggest that cusped models cannot reproduce the observations (Binney & Evans 2001). However, the detailed stellar kinematics provided by WF MOS will provide an essential probe of the dark halo profile in the central regions as they are implicitly dependent upon the form of the dark matter profile.

- The lumpiness of dark matter from tidal stream properties:
As globular clusters dissolve in the tidal fields of massive galaxies, the stripped material forms into extended, cold stellar streams. Such cold streams are very sensitive to kinematic heating and dispersal through interaction with \sim kpc substructure within the dark matter halo, while the hotter streams of dwarf galaxies are significantly more robust. Recently, extended tidal tails have been found associated with globular clusters, including Pal5 and NGC5466, and more examples are coming to light in extensive imaging surveys (e.g., Belukorov et al. 2006; Grillmair & Dionatos 2006). As cold young tails may morphologically resemble older, disrupting streams, it is vital to determine the heating of streams along their length, as this reveals their true nature and the interaction rate with any dark matter substructure. The WF MOS LR survey provides an ideal opportunity to kinematically map satellite tidal streams and hence constrain the dark matter substructure of the Milky Way halo, and hence the nature and number of dark satellites (Gilmore et al. 2007).
- The missing satellite problem - dark satellites:
The dwarf spheroidal galaxies (dSphs) of the Local Group are valuable laboratories in which to test the properties of the dark matter, as they are extremely dark matter dominated in their inner regions (e.g., Kleya et al. 2001, Wilkinson et al. 2004, Mateo et al. 1998) and appear to be the smallest stellar systems that contain dark matter in dynamically significant quantities. The number of low mass dark matter haloes in the vicinity of a Milky Way-type Galaxy is a strong function of the nature of the dark matter - cold dark matter (CDM) simulations typically over-predict the numbers of dSphs around the Milky Way by at least an order of magnitude (e.g., Moore et al. 1999) while warm dark matter models contain significantly fewer low-mass haloes (e.g., Bode, Ostriker & Turok 2001); this is known as the “CDM satellite crisis.” The recent

discovery of the extremely low luminosity Ursa Major dSph (Willman et al. 200, Kleyna et al. 2005), Boötes (Belokurov et al. 2006) and Canes Venatici (Zucker et al. 2006) satellites raises the interesting possibility that a number of dSphs containing very small stellar populations might have evaded discovery in previous surveys. However, only kinematic measurements can establish definitively whether an object is a dSph or a star cluster. WFMOS will be the ideal instrument for spectroscopic follow-up of new dSph candidates as wide-area surveys of stars to faint magnitudes ($V = 20\text{--}21$) are required to map the entire system and to provide spatially resolved velocity dispersions and abundance distributions. A candidate dSph with a low-luminosity ($M_V \sim -5$) and a large half-light radius ($\sim 200\text{pc}$) would have a velocity dispersion of $< 1\text{km/s}$ if it were a self-gravitating system containing no dark matter, while all dSphs observed to date have velocity dispersions in excess of 6 km/s . The existence of a previously unknown population of dSphs would be a major victory for CDM hierarchical structure models. For the nearer satellites, Gaia will provide proper motion measurements of the brighter member stars. This will enable direct measurement of the velocity ellipsoids throughout the system and thereby break the mass distribution-velocity dispersion anisotropy degeneracy.

- The nature of dark matter “particles” from satellite profiles:

The masses of dark haloes of dSphs can be used to constrain the properties of the dark matter, with the mass spectra of subhalos dependent upon its temperature. Furthermore, the density profile of the subhalos is also temperature dependent, with warm dark matter haloes typically of lower concentration than those found in CDM simulations (Bode et al. 2001). Hence it is essential to obtain a robust estimate of the total masses and densities of the known dSphs. Significant observational effort over the past decade has produced large kinematic data sets in dSphs which are being used to constrain the mass distribution within the main body of each system - the shape of the density profile can be used to constrain the physical properties of the dark matter particles. However, to complete the picture, we must also determine whether the dark matter haloes of dSphs extend beyond the edge of their main stellar distributions, in a similar manner to the halo of the Milky Way and other massive galaxies. The outer parts of most, if not all, dSphs exhibit signs of tidal disturbance in their stellar distributions (e.g., Carina: Majewski et al. 2005). However, the stellar kinematics in the outer regions remain controversial (see Wilkinson et al. 2004, Muñoz et al. 2005 for the case of Ursa Minor). Wide-area surveys of the outer regions of all dSphs are beginning (e.g., Walker et al. 2008), but achieving deep, wide-field spectroscopy is a task well-suited to WFMOS, allowing us to trace dwarf stellar kinematics well beyond their nominal tidal radii. If the apparent disturbance of their outer stellar distributions is indeed due to the tidal effects of the Milky Way (which could be confirmed, for example, by the detection of photometric *and* kinematic tidal tails) then their total masses cannot be much larger than a few $10^8 M_\odot$. On the other hand, if they are found not to exhibit evidence of tidal perturbation this

would argue strongly that their masses are in excess of $10^9 M_{\odot}$, in which case the “CDM satellite crisis” may well be resolved.

The mass and extent of the MW stellar populations

One of the primary goals of the WF MOS LR survey will be to dissect the Galaxy into its fundamental components, delineating structures based upon kinematics and metallicities. Without this deconstruction, understanding the detailed formation of the Milky Way is intractable. Such a survey will also reveal the presence of substructure, especially in the form of old, in-plane accretions. Furthermore, we only know the velocity distribution in the disk in the Solar neighborhood, although a global understanding of disk kinematics is required to understand its origins. A combination of Gaia and WF MOS will extend kinematic knowledge out to the edge of the disk in the Galactic anti-centre direction; Gaia alone cannot do this as the radial velocities do not probe far enough out. The resulting dataset will, for the first time, provide answers to the major questions about the Milky Way, including; what features in the velocity distribution are resonances due to the bar (Dehnen and others have claimed some of the local features are bar-related - if they are resonances we should not see them at other radii)? How much substructure is in the disk? Can we see the effects of transient spiral arm passages through the disk? What is the variation of the velocity ellipsoid as a function of position in the disk? These will provide the important clues to the formation of the Galactic components.

The current generation of bulge surveys, such as those using the AAOmega spectrograph (PI Freeman) and the Bulge Radial Velocity Assay (BRAVA) with HYDRA on the CTIO 4 m (Howard et al. 2008), will provide first order maps of the kinematics of the bulge (velocity dispersion and mean velocity as a function of position through the bulge), as well as detailed metallicity distribution function. However, the much larger samples provided by WF MOS will make it possible to investigate in detail the second-order kinematic structure seen in simulations of the Galactic bulge (e.g., Figs. 10 and 16 of Fux 1997). These velocity features depend on the details of the stellar structure through the bulge. The large samples will also make it straightforward to detect the signatures of the resonances that may have produced the peanut-shaped bulge of the Milky Way (Quillen 2002) as well as other resonant features.

Is the Milky Way Representative?

Is the Milky Way representative in its history and overall properties? To answer this question, any survey of the kinematic and chemical abundances of the Galaxy needs to be compared to similar studies of other spirals. In practice, this is impossible for all but the nearest spirals, M31 and M33. WF MOS offers the only realistic prospect of a panoramic spectroscopic survey of the stellar populations of our nearest large galaxies.

- Large area M31/M33 velocity and abundance survey—e.g., outer halo M31:

While M33 is distinctly different to the Milky Way, being an order of magnitude less massive and apparently undergoing a more quiescent assembly, the similarity and differences between M31 and the Galaxy have long been debated. With 8–10 m class telescopes, the ability to target the kinematics and chemistry of individual populations of stars, has led to a revolution in Galactic archaeology. Both galaxies appear to possess similar overall structures, in the form of metal poor stellar halos and complex extended stellar disks. By the time WF MOS is built, it is envisaged that dedicated surveys by DEIMOS/GMOS-class instruments will have provided detailed kinematic and chemical maps of the bulge and disk structures in these galaxies, revealing details of the underlying stellar halo that will contaminate any study. Furthermore, current studies are already targeting significant substructures that are readily apparent in photometric maps of the outer disk of M31. As with the Milky Way, the halos of M31 and M33 hold great promise for unraveling the accretion history through the identification of extremely low contrast tidal streams in kinematic and chemical space. Again, such studies will also probe the underlying dark matter potential of these galaxies, providing further clues as to whether the Local Group dark matter distribution matches expectations from Λ CDM cosmological models.

However, given their small field of view, it is impractical for DEIMOS/GMOS-class instruments to efficiently survey the sparse halo regions and this is clearly a region where the capabilities of WF MOS will provide a unique probe. Deep photometry (currently $\sim 80 \text{ deg}^2$ from the INT/WFC and CFHT/MegaCam; Ibata et al. 2007; Figure 4-3) of the extended halos of both M31 and M33, is steadily accumulating, and down the SE minor axis of M31 already extends along the entire line-of-sight to the centre of M33, a distance of $\sim 220 \text{ kpc}$ (15 degrees on the sky). These surveys are revealing an astonishing wealth of substructure, even in the outer halo. When complete coverage, $\sim 500 \text{ deg}^2$, is obtained in the next few years this unprecedented dataset will enable direct testing, via targeted efficient spectroscopic kinematic and metallicity follow-up surveys, of the predictions of Λ CDM cosmologies. Are fainter more diffuse tidal streams and relict debris dominant throughout the halo? What is the shape and total mass of the dark matter halos of M31 and M33? Will this explain the puzzling apparently quiescent history of M33? WF MOS will be the only instrument that can tackle these important questions within realistic time allocations.

populations and allows a detailed analysis of the physical processes governing star formation and evolution. Whereas the metallicity distribution of stars samples the chemical enrichment history of the galaxy, age estimates for individual stars provides information on the evolution with time of the abundances for a range of chemical elements. This impacts a wide area of astrophysics since the detailed progression of different species is directly affected by initial mass functions, star formation rates, infall and outflow of gas, nucleosynthesis pathways and stellar lifetimes.

- The role of star clusters in structure formation:

All stars form in clusters or associations. If we can reconstruct these using chemical tagging, that will be a valuable piece of information for star formation models used in cosmological simulations and will have relevance for feedback, galactic winds, etc. By reconstructing recently disrupted clusters we can determine current and recent cluster mass functions by combining kinematics and abundances. In addition, distances from Gaia combined with photometric information from wide field optical and near-infrared surveys hold out the tantalizing prospect of age dating stars in groups and thereby linking coeval star clusters over the entire history of the Galaxy.

Kroupa & Boily (2002) have emphasized the role that gas expulsion has on young cluster disruption and hence on the mass function of clusters that survive beyond star formation. This can be tested by looking for haloes of loosely bound or unbound stars near open clusters.

- Constraining nucleosynthetic pathways, sites, and stellar yields:

For most elements uncertainties remain about their formation sites, the nucleosynthetic pathways from which they are produced, and the yields from a given site. The detailed abundance ratios of stellar populations of different environments impose very strong constraints on the different processes that produce elements in stars (e.g., the IMF and SFH), improving our analytical power on the chemical evolution of the galaxies.

- Signatures of ancient accretions:

The importance of combining kinematic and abundance information for tracing the members of disrupted systems has long been recognized. Stars now distributed far from their birthplace can be identified by tracking their location in a combined chemo-dynamic phase space. An excellent example of this is provided by the detective work of Helmi et al. (2006) in unraveling the chemo-dynamical signature of the dispersed members of several groups in the Galactic disk. With detailed chemical abundance ratios, many of the ambiguities and degeneracies present in kinematic signatures can be resolved, enabling detailed allocation of various stellar components thereby allowing traceback to a common formation sites. Stars from common progenitors show distinct correlations between their orbital parameters, their abundance ratios and evolution with age, and can be directly used to probe evidence of the hierarchical formation of the Milky Way.

- The properties of extreme metal poor Pop III stars:

During the gaseous collapse of the Milky Way, the first generation of stars was left in a roughly spherical halo surrounding the newly formed disk, and this population of extremely metal poor stars are being uncovered today; although current measurements are limited mainly to stars passing through the Solar neighborhood, Christlieb et al. (2003) report the identification of a number of ultra-low metallicity stars associated with the Galactic halo. These stars provide a direct link to the conditions in the protocloud from which our Galaxy was formed. The sparseness of the halo population, however, ensures the progress in the discovery of this population is very slow. Intriguingly, simulations of Galaxy formation suggest that the earliest pre-galactic stars will be concentrated in the central regions of the Galaxy at the present time. The photometric metallicity distribution function (MDF) in the Zoccali et al. (2003) Bulge field shows a peak at $[\text{Fe}/\text{H}] \sim 0$ but with a long tail extending to $[\text{Fe}/\text{H}] \sim -2$, and a survey of the Galactic Bulge for very metal-poor stars should therefore yield a larger sample of such objects than the studies of the halo. Ongoing surveys, including the Sloan Extension for Galactic Understanding and Exploration (SEGUE/SDSSII; Lee et al. 2008) and the AAOmega/AAT Bulge survey (PI Freeman) will begin this important work.

However, the vital key to the earliest epochs lies with the distribution, kinematics and chemical properties of the rarest, ultra-low metallicity stars. Here only a combined LR/HR large scale survey by WF MOS can obtain the spectra of sufficient numbers of stars to obtain a statistically useful sample. The LR survey necessarily acts as a first cut at locating extreme metal poor whereas the HR counterpart is required to guarantee the nature of the stars and to provide the detailed abundance ratios needed for atmospheric analysis. Extremely metal-poor stars are fossils of the first stellar formation and metal enrichment processes. As such there is immense interest in answering questions relating to the initial mass function of the first stars and the subsequent mechanisms for early chemical enrichment in the Universe.

- Linking the Bulge to the high Z universe:

The Galactic bulge provides many clues to the nature of our galaxy. Laid down in the initial phases of the birth of the Milky Way, the bulge is related to spheroidal components of other galaxies and so establishing how it formed (collapse, accretion, disk instability) has a much broader significance in theories of galaxy formation. In addition, the interplay between the various processes involved will advance our knowledge of the stellar dynamics of galaxies more generally. The integrated spectra of Galactic Bulge fields and of Galactic globular clusters are directly comparable to those of distant ellipticals and the bulges of spirals as shown in Bica (1988). Spectral indices indicating abundances of alpha-elements such as Ca and Mg can be accurately calibrated from the HR spectra and allow a direct comparison between the Galactic Bulge and distant galaxies (e.g., Worthey et al. 1994). Another link with the high-z universe comes

from the measurement of Zn abundances. These are measurable in QSO absorption lines and probably reflect bulge formation at high- z that can be directly compared to the spatial and temporal distribution of Zn in Galactic Bulge giants covering a range of metallicities and ages.

4.2 Detailed Survey Design

While a Galactic archaeology survey with WF MOS encompasses a broad spectrum of goals, it is essential that the survey is undertaken to provide maximum scientific return within a realistic time allocation. Given the complexity of the various goals, no single, efficient survey strategy suffices. In the following sections we investigate the survey requirements needed to meet the science goals set out previously, based on current knowledge of the Galactic populations and some numerical simulations. The overall survey will be broken down into distinct components; The Galactic Bulge, The Outer Disk and the Galactic Halo. These will be supplemented with a targeted survey of known streams and other substructures, nearby dwarfs and a panoramic survey of our nearest large companions, M31 and M33. The general strategy will be to undertake a LR survey, followed by a HR survey to obtain detailed abundances on specific targets e.g., LR to identify metal poor bulge stars, then a HR follow-up and analysis of pop-III candidates.

4.2.1 *The Galactic Bulge*

The Galactic bulge provides many clues to the nature of our galaxy. Laid down in the initial phases of the birth of the Milky Way, it is expected that the bulge is home to a large population of the first stars that formed from the proto-galactic cloud. Furthermore, the present spatial and kinematic structure of the bulge, specifically the presence of the bar, has a long-range influence on the stellar structure of the Milky Way. Unfortunately, most of the stars, gas and dust in the Milky Way are confined to the bulge and plane, where extinction and crowding making it difficult to unveil the inner structure. Previous surveys have concentrated in clear “windows,” where optical surveys can be carried out (MACHO, OGLE, etc), although success has been varied. Current surveys, including AAOmega Bulge survey (PI Freeman) and BRAVA on CTIO (Howard et al. 2008), are beginning to obtain a more global picture of the kinematic and chemical properties of the Bulge.

Large scale photometric surveys in the near-IR will soon be able to penetrate gas and dust towards the Galactic centre. Covering a total of 360 deg^2 , a VISTA survey will identify a $\sim 5 \times 10^8$ point sources, with roughly a million variable stars providing distance estimators. While such a photometric dataset will provide a wealth of information on the bulge, including the 3-D structure, the identification of the earliest stars and understanding the bulge’s dynamical influence will require detailed spectroscopic follow-up.

It is currently unclear whether the inner Galaxy contains a single bulge component formed via the buckling and thickening of a bar (Kormendy & Kennicutt 2004) or whether there is an additional, distinct spheroidal component which built up through accretion (Freeman & Hawthorn 2002). WF MOS can provide a definitive answer to this question by establishing the dynamical state of the bulge using a large

sample of bulge stellar velocities and metallicities. By comparing the observed kinematics with the predictions of dynamical bulge models, (including both descriptive Schwarzschild orbit synthesis models, and fully evolutionary N-body models which track the formation of the bar/bulge via disk instabilities), it will be possible to understand the detailed properties of the stellar bar/bulge and learn which processes were dominant in the evolution of this region. Currently available kinematical data are totally inadequate for this purpose, and a WF MOS survey will provide the first sample large enough to probe the full kinematic structure of the inner Galaxy.

In order to estimate the number of stars necessary to distinguish different bulge models, the kinematical predictions of an N-body stellar bar (Athanasoula 2005) and an axisymmetric bulge model (Dwek et al. 1995) can be compared. Allowing for foreground contamination, ~ 1000 bulge stars are needed to resolve the systematic ~ 10 km/s differences in dispersion between the models over distances of about 1 kpc along a single sightline. The limited size of previous surveys has prevented discussion of kinematic variations along the line-of-sight. As an example, Figure 4-4 show how the models differ in the variation of projected velocity dispersion at low Galactic longitude. Because the kinematics vary on scales of a few degrees, we require the good areal coverage of the region $|\ell| < 15^\circ$ provided by our proposed sightlines. Further, although the location of the ends of the photometric bar are known from star counts, models of the resonant thickening of bars into peanut bulges predict the presence of resonances located within the bar (e.g., Quillen 2002); our goal is to map out these resonances through their velocity signatures.

Clump giants will be used for much of the main bulge survey, because they are numerous in most stellar populations older than about 2 Gyr and have a well-defined relation between absolute magnitude, age and $[\text{Fe}/\text{H}]$, allowing accurate estimates of their distances. In Baade's Window, about half of the stars with $I < 16$ are clump giants (Paczynski et al 1999). It is easy to measure their radial velocities and abundances, and verify their gravities using the Ca II 850 nm triplet. Clump stars are ideal tracers because we can measure their distances using reddenings individually determined from the 8620 Å diffuse interstellar band. The OGLE photometry shows that there are several thousand clump giants per WF MOS field, even in the outer bulge. Also included will be brighter giants, to measure the kinematics of other bulge populations, such as younger AGB stars and very old metal-poor stars in the bulge region. The younger stars are important tracers of any more recent evolution of the bulge. The metal-poor stars in the bulge are particularly interesting, because recent simulations suggest that the earliest pre-galactic stars will be concentrated now in the central regions of the Galaxy.

While LR kinematic studies will provide important clues in improving our understanding for the formation and evolution of the Galactic Bulge, for detailed comparison to evolution models will require the determination of the chemical properties of the Bulge population. WF MOS will be employed to undertake a HR survey to (i) establish the shape of the detailed metallicity distribution function (MDF) in each field, for comparison with chemical evolution models, and (ii) quantify the contribution of the more

metal-poor stars to the bulge and determine (in combination with kinematics) whether they are part of the bulge or part of the galactic stellar halo. Existing photometric MDFs do not have sufficient statistics for this purpose: we will dramatically improve this situation with our spectroscopic MDF. The bulge shows a strong vertical abundance gradient, and its overall MDF extends from $[Fe/H] = +0.3$ to -1.5 (e.g., Zoccali et al 2003; 2006). WFMOS will provide not only the mean metallicity but also the distribution of elemental abundances (most notably Fe-peak and alpha-elements) at different locations across the bulge, which will help us understand its chemical evolution. Observing an unbiased sample of giants in six fields distributed over the bulge, WFMOS will reveal how the MDF changes relative to the mean abundance gradient. The approach will employ the LR survey to identify candidates of interest (i.e., popIII members of the bulge) to be followed up in the HR mode, providing abundance fingerprinting of the differing contributors to the Bulge population.

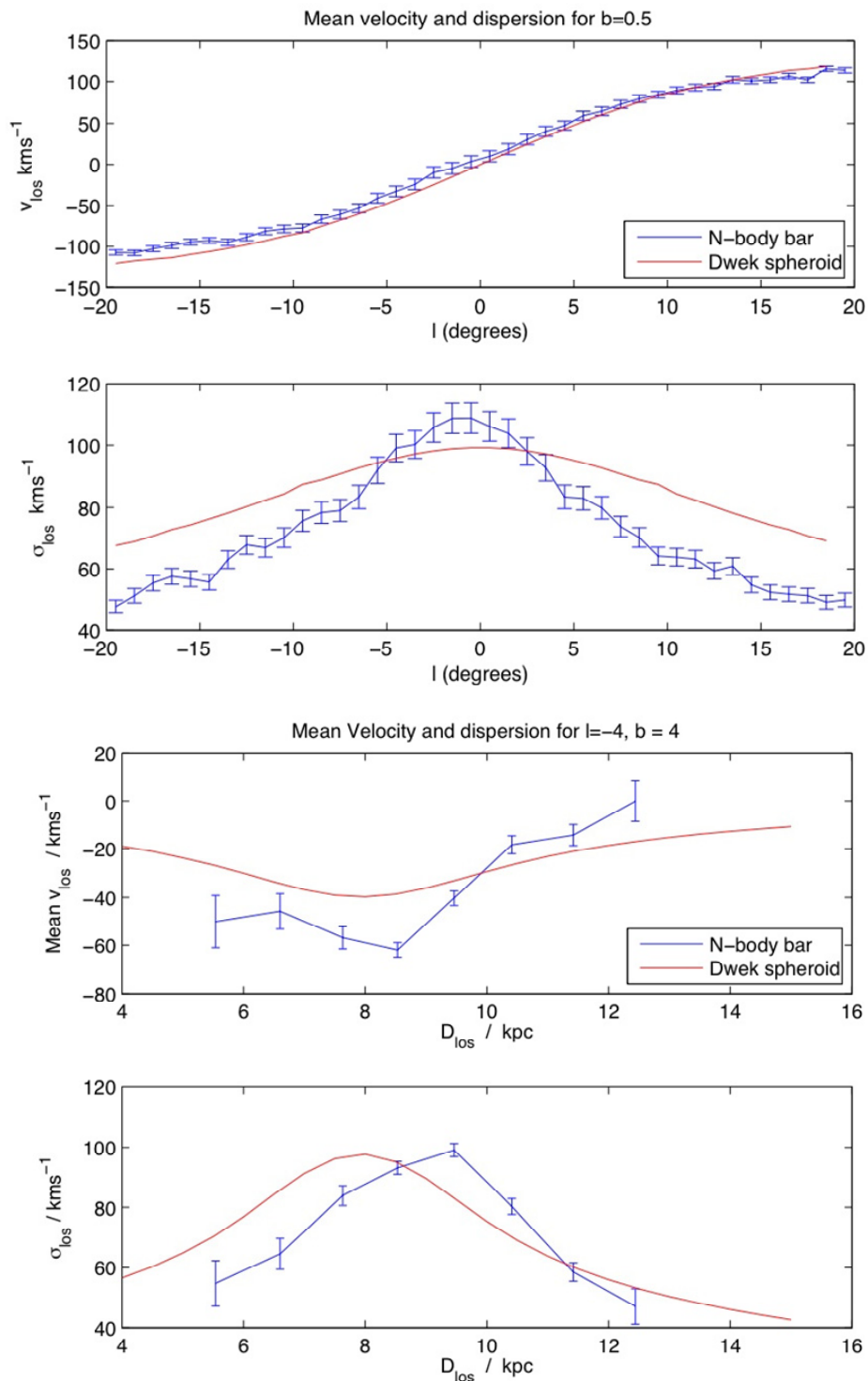


Figure 4-4: Dynamical predictions based upon a N-body simulation of a stellar bar and an axisymmetric bulge model. The comparison assists in determining the observing strategy necessary to distinguish different models for the Galactic bulge.

4.2.2 The Outer Disk

The outer disk is targeted for two primary reasons; firstly to characterize its structural properties, especially the functional decrease in the stellar density and truncation radius. Secondly, the survey will be used to identify any low latitude tidal streams whose demise will contribute to the thick disk population. In characterizing the outer stellar disk, the best region to target is toward the Galactic anti-centre, where we propose to characterize the stellar populations using three survey stripes at $l=160^\circ$, 180° and 200° , extending between $b=\pm 30^\circ$.

Figure 4-5 shows a numerical simulation of the demise of the putative Canis Major dwarf galaxy, produced by Penarrubia et al. (2005). The density excess characterizing the centre of the Canis Major region and its extension into the Monoceros ring has lead to much debate in the literature as to its nature: a close to in-plane accretion of a dwarf galaxy; or a flared warped outer disk compounded by a possible outer spiral arm. If a low latitude accretion this would have resulted in extensive tidal debris, reaching $\pm 40^\circ$. Clearly these would intercept the vertical stripes used to characterize the structure in the outer disk, and these would allow for the identification of significant substructure, including tidal streams, in the region of the outer disk. However, the strongest constraint on the evolution of the tidal disruption of equatorial systems are longitudinal velocity gradients, and hence the two additional survey stripes at $\pm 30^\circ$, extending between $l = 120^\circ$ and 240° , will be employed to measure these over large portions of tidal debris streams.

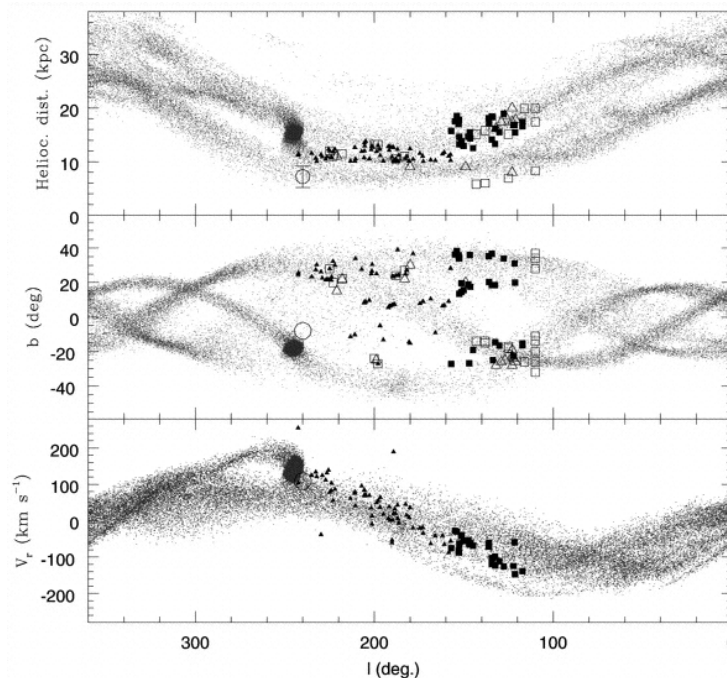


Figure 4-5: The properties of a numerical simulation of the demise of the putative Canis Major dwarf galaxy and the resultant Monoceros Stream (Penarrubia et al. 2005)

While kinematics will provide a first step to disentangling the various substructures expected in the outer disk, clear discrimination is only possible with abundance studies; each of the accreted progenitors will carry its own distinct chemical fingerprint which metallicity through proxy can only provide a first order discriminator. Hence, targeted regions of the streams and central body will be observed in HR mode to provide this information.

4.2.3 The Galactic Halo

The identification of halo streams is important for several of the key science goals of this survey, namely determining the mass and extent of the dark matter halo, as well as the identification of any putative dark substructures. Due to their low projected stellar density (>30 mag/sq arcsec), it is extremely difficult to identify tidal streams in the Galactic halo within photometric surveys; only kinematic and chemical signatures can be effective to locate accreted systems from the Galactic populations.

Figure 4-6 shows the distribution in RA and Dec of debris from a typical inner halo satellite at 12 Gyr. Orbital plane precession due to the non-spherical components of the Galactic gravitational potential means that the debris is distributed over much of the sky, although the surface density of material is low and highly non-uniform. Due to their proximity, an individual stream covers a huge swathe of sky and hence optimizing a survey to maximize the detection and characterization of a population of streams is not a straightforward task. In the following, N-body simulations (provided by A. Helmi) are used to construct mock skies such that differing observing strategies can be compared.

The simulations follow the evolution of satellite galaxies orbiting in a static Milky Way potential for 12 Gyrs. A total of 32 satellites with orbits in the inner halo (orbital apocenters less than ~ 20 kpc) were followed along with two satellites in the outer halo. All satellites were initially single-component Plummer spheres containing 100,000 particles. The orbital planes of the satellites were randomly oriented with respect to the plane of the Galaxy and the initial orbits were strongly radially anisotropic. A detailed description of the simulations, including the initial conditions, Milky Way model and integration scheme used is given in Helmi & de Zeeuw (2000). We construct an ensemble of debris trails by generating five realizations of each satellite's debris at 12 Gyr, obtained by first rotating in azimuthal angle and then observing the debris from the position of the Sun.

In order to establish the number of stars that would be observable in a given survey, we first estimate the fraction of satellite stars that are likely to be K-giants. Using the Besancon model of the Milky Way (Robin et al. 2003; <http://bison.obs-besancon.fr/modele/>) we find that 10–15 percent of the halo population are K-giants. In the Besancon model, the halo is represented by a old, metal-poor stellar population with an initial mass function $dn/dm \propto m^{-0.5}$ (Haywood et al. 1997), which is a reasonable first-order approximation to the stellar populations expected in the progenitors of halo streams.

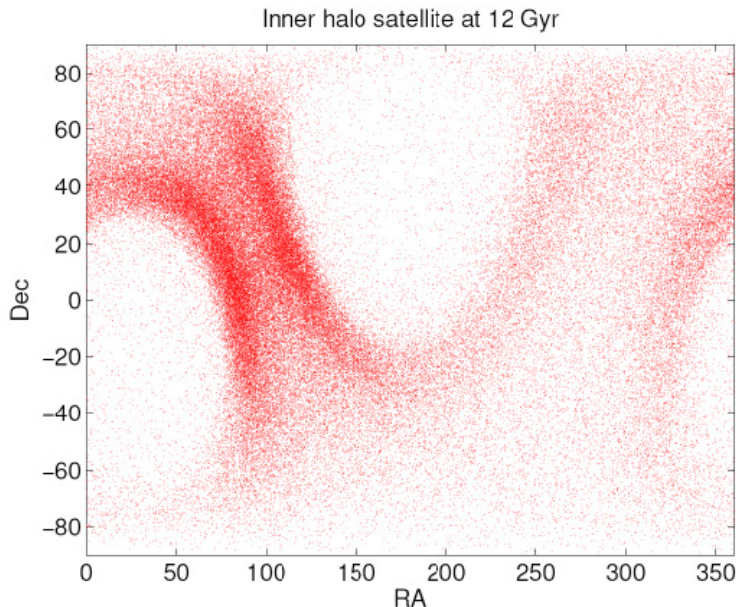


Figure 4-6: Distribution of debris from an inner halo satellite after 12 Gyr as a function of RA and Dec.

The goal is to detect *and then* characterize those streams we detect; the characterization of a stream includes a determination of the integrals of motion (e.g., energy E) of the satellite which gave rise to the stream, as well as an estimate of the internal velocity dispersion of the system based on the dispersion in the integrals of motion among stars in its debris trail. Relatively small numbers of stars suffice to detect the presence of substructure in velocity space. For example, Helmi & de Zeeuw (2000) show that the two-point correlation function in velocity space can be used to detect clumping - the presence of substructure shows up as an excess of stars with small velocity differences. Similarly, streams with favorable energies and angular momenta can be detected against the Galactic foreground with small samples of three-dimensional velocities - Helmi et al. (1999) identified a debris clump containing 13 stars (out of a sample of 97). We therefore assume that for a robust detection of the phase-space overdensity associated with a particular satellite, approximately 100 member stars would be required. However, to characterize such a population requires significantly more data, and in what follows we estimate that around 1000 satellite stars is the minimum required for adequate characterization.

Of course, all stellar debris in the halo will be observed through a foreground of Galactic stars. While multi-band photometric surveys (e.g., 2MASS, WFCAM, VISTA) can be used to preferentially target K-type stars, the selection will not be completely efficient. Using the Besancon model, we find that at Galactic latitude ($b \sim 30^\circ$) there are ~ 4000 stars per WF MOS field which satisfy $V < 20$ and $2 < V - K < 3$, as opposed to ~ 200000 at $b \sim 0^\circ$. Thus fields at $b > 30^\circ$ should be the primary focus of the search for halo streams. Naturally, this will mean that low-latitude, localized streams will not be detected. However, at low latitude the number of pointings to achieve complete targeting of K-giant candidates becomes prohibitively large - complete targeting is essential to ensure sufficient numbers of stars per stream will be

observed. In contrast at high latitude we will supplement the K-star selection with candidate MSTO and HB stars depending on the photometric survey results.

In the following, we restrict ourselves to considering several 800 deg² surveys to $V = 20$ with the Galactic foreground removed via observation of every K-giant candidate (i.e., $b > 30^\circ$). For each survey, one realization of each satellite is selected and the number of stars falling within the survey region is counted. It is assumed that 10 per cent of those stars will be K-giants, and that 1000 stars are required to characterize the satellite. The survey design considered comprised (a) a 5-degree-wide block ($b = [30^\circ, 35^\circ]$, $l = 0^\circ$ to 180°); (b) a cross made up of two 2-degree-wide strips ($l = 180^\circ$, $b = [-90^\circ, 90^\circ]$; $l = [0^\circ, 180^\circ]$, $b = [30^\circ]$); (c) a 10-degree-wide block ($b = [30^\circ, 40^\circ]$, $l = 0^\circ$ to 90°). The results of this analysis revealed that, even through the cross survey structure has the highest chance of ‘clipping’ a stream, the simple block structure was the most efficient design, allowing the characterization of ~30% of the substantial stellar streams in the inner halo (with a progenitor mass exceeding $10^7 M_\odot$). Reducing the survey area of the block regions to only 400 deg² reduces this to ~10–15%.

For the outer halo, streams are more spatially confined as the timescale for phase mixing are much longer and precession rates are much lower. However, we note that the nature of these streams makes them the easiest to detect as they are localized on the sky. It is therefore expected that the majority of such streams will have been identified prior to WFMOS using all-sky surveys (see e.g., the recent work by Belokurov et al. 2006). For as yet undiscovered massive streams in the outer halo, a cross-like pattern is preferred since the surface densities of the targets is sufficiently high for the intersection to yield enough members. We conclude that our survey should not be optimized for the detection of these streams, although we note that WFMOS will be the ideal instrument with which to obtain follow-up spectra in targeted regions of such streams in an efficient manner.

Table 4-3 summarizes the results of our analysis for block surveys, listing the percentage of massive (10^7 stars) and low-mass (10^6 stars) streams, which are characterized by block surveys. The 800 square degree survey also allows detection (100 stars per stream) of 50–100% of outer halo streams and ~90% of inner halo streams, although as noted above in-plane accretions are systematically missed. In summary, we conclude that an 800 square degree survey with the fields arranged in a 10-degree-wide block at high latitude ($b > 30^\circ$) will characterize about 30 per cent of all halo streams. We note that this survey could be supplemented by a low-latitude block to observe streams which were missed by the main survey.

Table 4-3: Summary of results of our analysis for block surveys

Block of 800 square degrees ($b \sim 30^\circ$)				Block of 400 square degrees ($b \sim 30^\circ$)			
$N = 10^7$		$N = 10^6$		$N = 10^7$		$N = 10^6$	
Inner	Outer	Inner	Outer	Inner	Outer	Inner	Outer
50 – 60%	50 – 100%	30%	50%	60%	50%	10%	25%

4.2.4 Targeting Substructure; Streams & Dwarfs

To help resolve the CDM satellite crisis, it is vital to uncover the true dark matter content of dwarf galaxies. In addition the distribution of dark matter within dwarfs will reveal the presence of central cores or cusps, providing a measure of the fundamental nature of dark matter itself. Such measures require targeted surveys of the known dwarf population. Given their relatively small spatial extent, dwarfs can be fully targeted using a small number of field pointings using low-resolution measurements to probe the overall kinematics and abundances of the stellar components. The central regions on the other hand provide a sufficient density of targets for HR followup in order to characterize the detailed chemical evolution of their, often, complex multi-component nature.

In contrast, streams require more extensive coverage to characterize their systemic velocity variation (and potentially abundance variation) as a function of position and the variation of the velocity dispersion azimuthally along the stream. Here low resolution surveys are key to quantifying these physical processes yielding measures that are extremely sensitive to, and hence make excellent probes of, the underlying Galactic potential and the nature of the dark matter component. Furthermore, the low contrast and large angular extent of the streams are well matched to the proposed WF MOS field-of-view and multiplexing.

4.2.5 Targeting M31 & M33

As noted previously, M31 and M33 offer the only realistic opportunity to obtain kinematic and metallicity information on individual stars in large galaxies other than our own. Recent mapping with wide field cameras have provided a detailed source catalogue of stars over one third of the halo of M31 (out to a radius of ~ 100 kpc), with future observations mapping the remaining two thirds. Such a catalogue provides a unique opportunity to obtain the kinematic and chemical information needed to unravel the formation and properties of the stellar and dark matter halo of an external L^* galaxy. Hence, the observing strategy is straightforward, using WF MOS to obtain spectra in LR mode to tile the halo. The limiting factor, however, is the spectrograph efficiency; assuming an end-to-end efficiency of 15%, an 8hr integration for an $I = 21.5$ star (probing 1 magnitude down the red giant branch) will result in a $S/N \sim 5/\text{\AA}$, sufficient to determine velocities to 5 km/s and $[\text{Fe}/\text{H}]$ (from the CaT proxy) to an accuracy of 0.2 dex. A panoramic study with WF MOS would require a targeted survey covering a total of ~ 400 sq degrees (~ 2 sq deg/night) for a total of 200 nights. This is impractical and hence, an efficient sampling, based on previously acquired photometric data, is necessary, focusing on a smaller subset of ~ 25 – 50 fields will be required. While this is still an ambitious undertaking, we note that the strongest constraint on the shape of any dark matter halo is the gradient along stellar streams and any sparse tiling strategy has to be carefully developed to efficiently enable the requisite measurements to be made.

4.2.6 Overall Survey Design

Exposure times and other technical details associated with the GA surveys are presented in Section 6. Here we summarize the survey details:

- Galactic LR mode; ½ hr integrations, 20/night
- Galactic HR mode; 1 hr integrations, 10/night
- M31/M33 LR mode; 6 hr integrations, 1/night

The ordering in this table represents a priority listing, initially targeting Streams/Dwarfs to obtain early results. Similarly, the Bulge survey will result in significant early key results, while the completed LR/HR data will provide resource to be mined over many years. Outer Disk and Halo will produce several initial results, but key results will come from the completed surveys.

Note: M31/M33 is a proposed future survey to be undertaken after the Primary Galactic Survey. It will be completed in two stages: Stage 1 targets known substructure and a coarse sampling of the halo, while Stage 2 is geared to provide a complete kinematic census of the halo of M31/M33

Primary Survey			
Target	Mode	Number of Fields	Number of Hours
Streams/Dwarfs	LR	330	165
	HR	110	110
Bulge	LR	300	150
	HR	600	600
Outer Disk	LR	270	135
	HR	100	100
Halo	LR	630	315
	HR	315	315
Total			1890 (190 nights)
Future Survey			
M31 & M33	LR	100 (Stage 1)	600
		130 (Stage 2)	780

The geometries of the surveys are depicted in Figure 4-7.

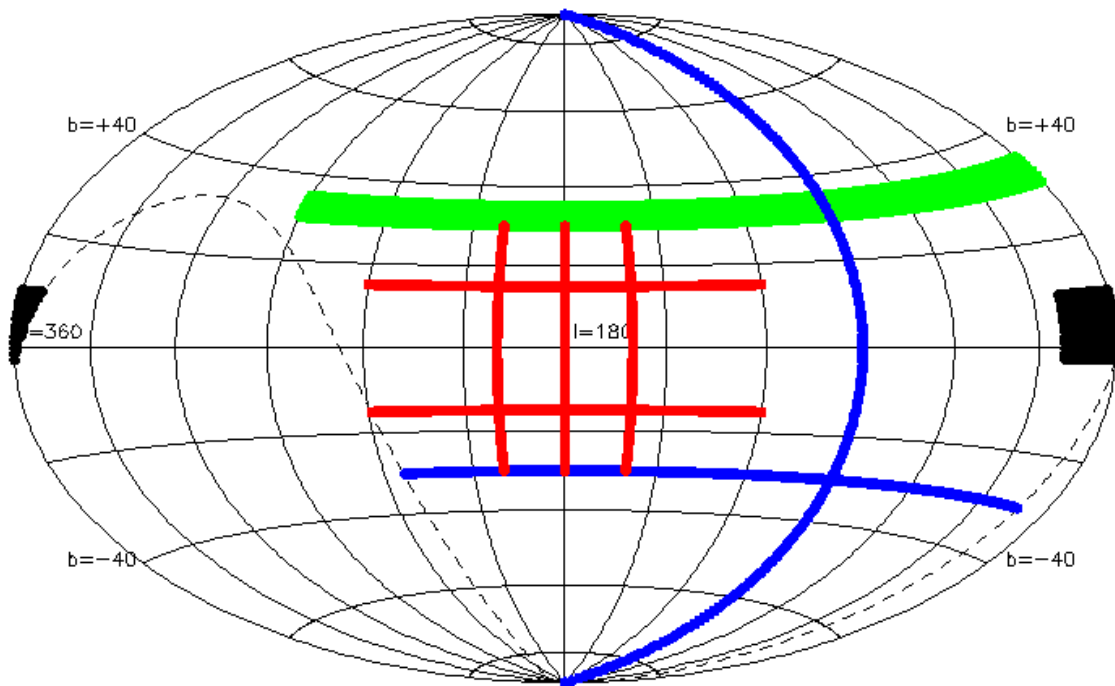


Figure 4-7: Aitoff projection of the proposed Primary Galactic Archaeology Survey.

4.3 Technical Considerations

Here we collate those technical considerations which flow down to instrument requirements as well as data reduction issues specific to the GA surveys.

4.3.1 Spectroscopic Requirements

For detailed HR abundance work most lines of interest are weak e.g., $EW < 100 \text{ m}\text{\AA}$. Ideally they should be on the linear part of the curve-of-growth (see Figure 4-8) but this is not always possible so we must contend with lines in the range $10 \text{ m}\text{\AA}$ to $250 \text{ m}\text{\AA}$. Notable exceptions are the CaT lines used in the LR analysis, which are generally heavily saturated and on the damped part of the curve-of-growth. Here the CaT line profiles are dominated by intrinsic broadening due to saturation (typically $FWHM 2\text{\AA} - 3\text{\AA}$) and to a lesser extent by the convolution due to the resolution of the spectrograph (at $R = 5000$ the spectrograph $FWHM \approx 1.7\text{\AA}$).

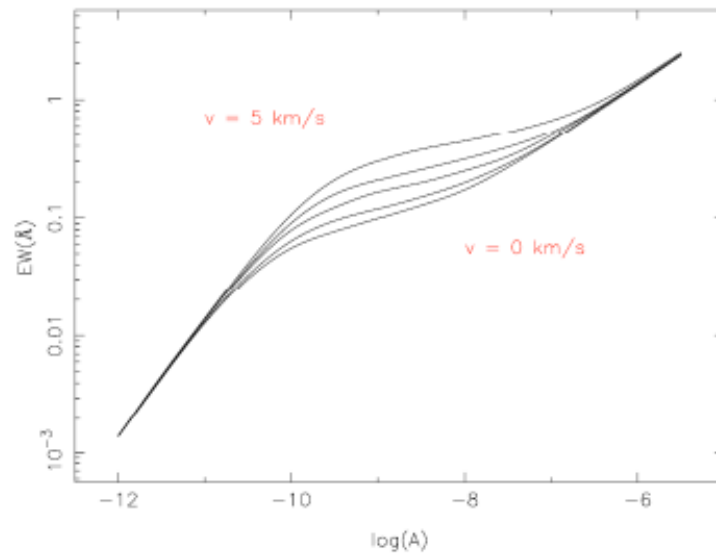


Figure 4-8: The curve-of-growth of typical weak lines highlighting the critical dependence of the abundance determination on knowledge of the microturbulent velocity

Turbulence and rotation velocities of late-type giants typically only broaden the line profiles by a few km/s, and hence the lines are unresolved at $R = 20,000$ ($\text{FWHM} \approx 15\text{km/s}$) and the line profile is generally dominated by the spectrograph. Early-type stars (and dwarfs) have velocity dispersions much greater than this (e.g., faster rotation velocities) and hence spectra are fully resolved.

Despite the dampening wings, to first order even the LR CaT lines can be reasonably well approximated by Gaussian functions (e.g., see Figure 4-9), and we can use this to gain some insight into the limiting factors that determine the accuracy of the velocity and EW measurements (cf. Battaglia et al. 2008).

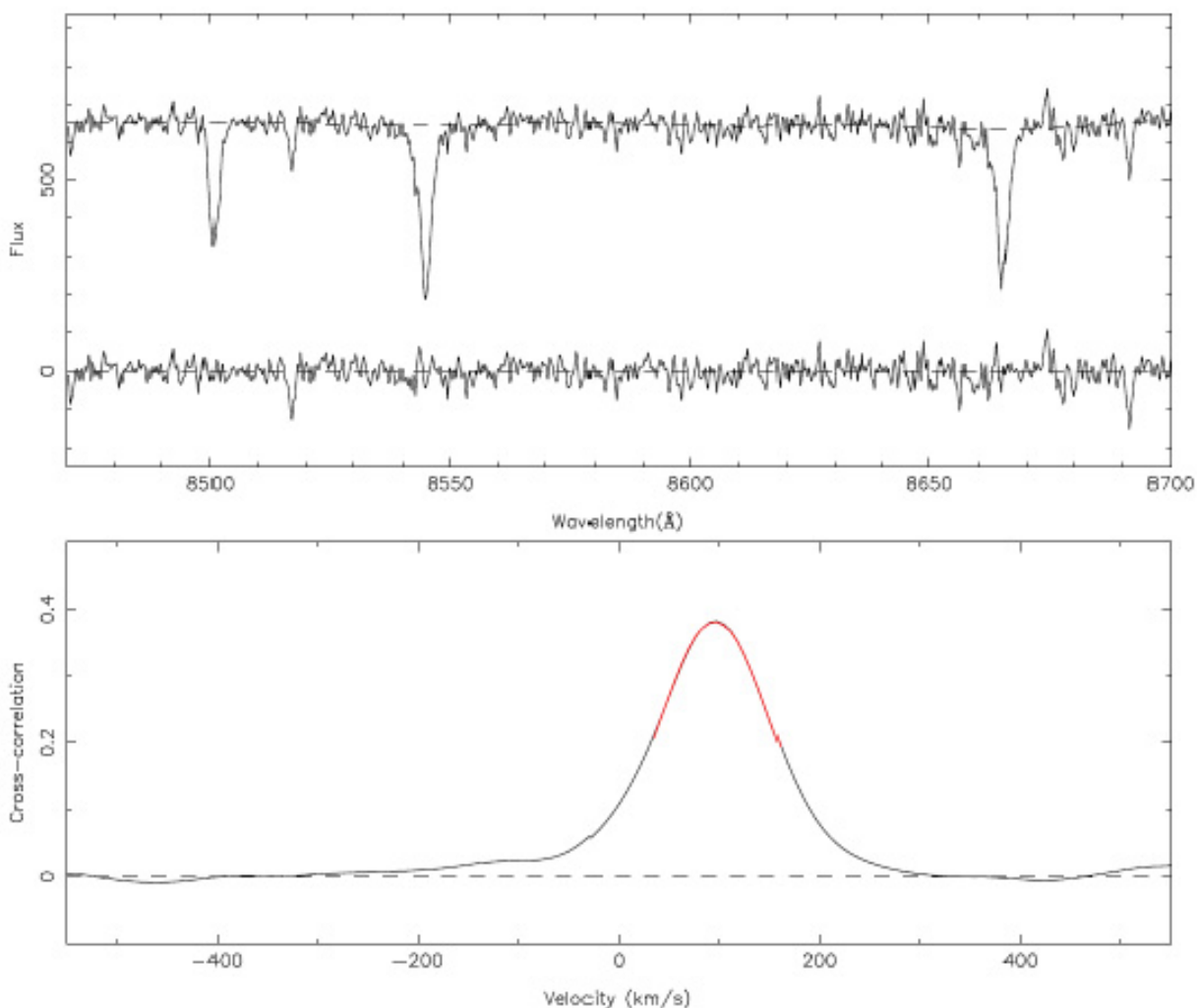


Figure 4-9: Top panel: the upper portion presents the CaT region for a K-giant in the Sculptor dSph with derived $[\text{Fe}/\text{H}] = -1.50$ dex LR (-1.63 dex HR), showing an example of automated continuum fitting (dashed line). The lower portion presents the residual after continuum removal and after subtracting Gaussian model fits to the three CaT lines. Lower panel: the derived cross-correlation function and associated Gaussian fit around the peak region.

Here we define resolution as $\text{FWHM} = 2.35\sigma$, where σ is the Gaussian profile equivalent scale parameter (e.g., $\sigma_v = 2$ km/s then the $\text{FWHM} = 4.7$ km/s, i.e., $\approx 0.1\text{\AA}$ at 6000\AA). Since the total line flux $= I_p \sqrt{2\pi\sigma} = I_p \times \text{FWHM} \times 1.07$, where I_p is the peak flux, this implies that line saturation (i.e., $I_p = C$) occurs when $\text{EW} \approx \text{FWHM}$. The intrinsic FWHM of weak lines in late-type giants is typically only a few km/s, i.e., lines with EWs of ≈ 100 m \AA and above are saturated. As noted previously, the CaT lines are heavily saturated anyway and typically have EWs well above 1\AA .

To a reasonable approximation, and certainly for weak lines, the noise in the continuum ($\sigma_n/\text{\AA}$) due to sky plus object dominates, and over any individual line the continuum level/ \AA , C , can be taken to be constant. Therefore, the EW and its error due to random noise, ΔEW , are given by

$$\text{EW} = \frac{I_{\text{total}}}{C} \Delta\text{EW} = \frac{\sigma_n \sqrt{w}}{C} = \frac{\sqrt{w}}{s:n}$$

where the total line flux is I_{total} , $s:n$ is signal:noise per \AA in the continuum, and w is effective width (\AA) the line is integrated over. For a fitted Gaussian profile $w = \sqrt{4\pi\sigma} \approx 1.5$ FWHM hence

$$\Delta\text{EW} = \frac{\sqrt{1.5\text{FWHM}}}{s:n} = \frac{\sqrt{1.5\lambda/R}}{s:n}$$

and the FWHM of the line(s) and the continuum signal-to-noise are the primary abundance error drivers from a measuring point-of-view.¹

In a similar way we can place constraints on the accuracy of measuring velocities. For Gaussian-like line profiles, which is a good approximation even for native saturated lines like the CaT, the minimum variance bound on the error in the estimated line position is given by

$$\text{var}\{\hat{\lambda}\} = \frac{\sigma^2}{\eta} \frac{\sigma_n^2 \sqrt{16\pi\sigma}}{\eta}$$

where the line flux is η and where the noise in the continuum, σ_n ($/\text{\AA}$), dominates and can be taken to be a constant over the region of interest. Rewriting this in terms of the FWHM of the line, the EW and the continuum signal-to-noise $s:n$, leads to

$$\Delta\hat{\lambda} \approx \frac{\text{FWHM}^{3/2}}{\text{EW } s:n}$$

where again all measurements are per \AA .

As examples: for LR the two strongest CaT lines, $\lambda_{8542} \text{\AA}$, $\lambda_{8662} \text{\AA}$, used in abundance analysis are heavily saturated and have a FWHM at a resolution of $R = 5000$ of $2 \text{\AA} - 3 \text{\AA}$, while the EW of each line is typically $\approx 2 \text{\AA}$. For a continuum signal-to-noise of $10-15/\text{\AA}$ this implies a lower bound on the combined EW error of $\approx 0.2-0.3 \text{\AA}$, which translates to an error of $\pm 0.1 \text{dex}$ in $[\text{Fe}/\text{H}]$. This also implies accuracies of wavelength centering of around 0.1\AA per line, or equivalently $\approx 2-3 \text{ km/s}$ velocity errors using all three CaT lines. Factoring in the LR Mgb region will then further reduce the achieved velocity to below $\pm 2 \text{ km/s}$. This should be achievable in $\approx 1800\text{s}$ integrations to $V = 20$.

¹ The last part of the equation on the RHS is only valid if the resolution of the spectrograph dominates the FWHM. This is not generally the case on the non-linear part of the curve-of-growth, or for early-type stars with high rotation velocities, or sub-dwarfs with high surface gravity.

At HR for the weaker lines of interest, EWs to $\approx 5\text{m}\text{\AA}$ accuracy will be a typical requirement. At $R=20000$, in many cases the resolution will be dominated by the spectrograph, which suggest that at a fiducial 6000 \AA with $s:n\ 150/\text{\AA}$ implies a $\Delta\text{EW} = 5\text{m}\text{\AA}$. This should be achievable in ≈ 3600 s integrations to $V = 17$. Line blending is not a serious issue for most lines of interest if standard multicomponent line profile model fitting is used for EW analysis.

A further requirement on the spectrograph is that scattered light is kept to a minimum since continuum level estimation can be seriously biased by “DC” offsets due to unexpected scattered light. Accurate stellar atmosphere modeling and subsequent chemical tagging also critically depends on the fine detail of series of EW measurements, any systematic bias in the continuum level is a serious impediment to accurate analysis. The effect on EW estimation is straightforward. If the continuum level is wrong by 5% due to a scattered light offset, then since the derived line flux, integrated with respect to the continuum will still be correct, the EWs will be wrong by the same fraction as the continuum level.

For the low resolution survey, EWs are typically quite large. For example, the sum of the 3 CaT line EWs is typically within a factor of 2 of about 5\AA . An EW error of 10% would therefore translate to a summed EW error of 0.5\AA which translates to a systematic error of 0.2 dex in derived $[\text{Fe}/\text{H}]$. We are aiming here for 0.1 dex rms errors so would certainly expect unpredictable systematic errors to be no larger than this. This would suggest that for LR the unpredictable scattered light component should be below 5% of the continuum level.

For the high resolution work, most of the lines of interest are in the range $10\text{m}\text{\AA}$ to $100\text{m}\text{\AA}$, with some up to $250\text{m}\text{\AA}$. Similar arguments hold: systematic errors should be no worse than the $5\text{m}\text{\AA}$ rms accuracy from $s:n$ considerations. This leads to the same 5% accuracy requirement for the high resolution survey.

Accurate fluxing of spectra is also a requirement since comparison with external galaxies over a range of redshift, via spectral synthesis models, depends on accurate calibration of line indices. Likewise linking the high redshift universe with detailed comparison of the Galactic Bulge components depends on good spectrophotometric calibration. Regular observations of flux standards should suffice to define the differential flux calibration, whilst fiber, slit and other losses can be monitored and corrected by direct comparison with broadband photometric data. A relative flux calibration of better than 5% will suffice and is typical of the accuracy of external galaxy spectrophotometry.

We summarize our discussion of the instrument requirements for the GA survey in the following table:

Table 4-4: Galactic Archaeology Spectroscopic Requirements Summary

High Resolution mode	R=20,000	V=17	S/N = 10-15 / Å
Low Resolution mode	R=5,000	V=20	S/N = 150 / Å
Wavelength accuracy:	0.1 Å		
Continuum estimation accuracy:	5%		
Relative flux calibration accuracy:	5%		

4.3.2 Data Reduction Requirements

Automated LR data analysis, particularly in the CaT region, is well advanced, but it is still worth applying information theory techniques in this wavelength regime in conjunction with the Mgb region to see if we can extract more information other than velocities and proxy [Fe/H] measurements (e.g., Munari et al. 2005). With a range of different species present in both wavelength ranges, albeit often as weak lines, several studies are currently underway in addition to our own efforts (e.g., Kirby et al. 2008) to ascertain if reliable global abundance ratios such as α -element ratios can be derived from LR spectra.

Automated HR data analysis presents a more complex challenge, although several promising lines of development are being investigated by members of our team. The first challenge is to combine photometric measurements, distance estimates and kinematics, with global spectral properties to derive reliable stellar atmosphere parameters (log g , effective temperature, microturbulent velocity, overall metallicity and α -element ratio) prior to undertaking detailed abundance estimates of individual species. A key area under investigation by our team is the use of new methods such as Artificial Neural Nets (ANNs), Self Organizing Maps (SoMs), or Principal/Independent Component Analysis (PCA/ICA). These may eventually improve upon traditional feature extraction approaches based on line lists (e.g., direct EW measurement) combined with model atmosphere template fitting (cf. Kurucz model atmospheres as in Munari's extensive library, or alternative stellar model atmospheres such as MARCS e.g., Gustafsson, et al. 2008).

Standard data processing can build on existing tools for basic instrumental signature removal, bookkeeping, spectral extraction and wavelength calibration (e.g., 2dF, 6dF, WYFFOS, FLAMES...). Specific additional issues to be dealt with include:

- Data formats, FITS file structure and HDU (Header Data Unit) content - all data structures should have sufficient meta-data present to be self-describing by, for example, also including fiber allocation table as FITS table extensions
- Instrument stability and calibration frequency - including flats, arcs, standard star observations both for flux calibration and velocity verification. Accurate, robust and stable wavelength calibration is a critical requirement for good sky subtraction (i.e., at least 1/20th of a resolution element accuracy over the entire wavelength range of interest is required).
- Automating sky subtraction in an efficient way is critical to the success of the both the GA and DE surveys - this is discussed further in Section 6

- It is crucial to benchmark data reduction (and analysis) strategies for testing data reduction techniques on realistic data sets. In this regard our active involvement in several VLT FLAMES surveys provides us with an excellent set of real benchmarking data that is being analyzed both with conventional methods and prototype analysis tools required for full GA data analysis.
- Data fidelity will be ensured to comply with Virtual Observatory standards for archiving and future dissemination.

An important aspect of the WF MOS GA survey will be the implementation of a complete data reduction pipeline that takes raw data to physical parameters efficiently, with as little user intervention as possible. Similar approaches are being adopted for ongoing stellar surveys (e.g., MATISSE; Recio-Blanco et al. 2006, SEQUE; Lee et al 2008a,b, Prieto et al 2008; Shetrone et al 2008; RAVE; Zwitter et al 2008). These automated methods are vital to the efficacy of large stellar surveys, contrasting with the historical reduction of high resolution stellar data which has been typically manual and extremely time consuming. The following sections outline our studies to date, but our development efforts will build on the successes (and note the difficulties) of ongoing projects. (Issues relating to sky subtraction, which are common to all WF MOS surveys, are dealt with separately in a later section.)

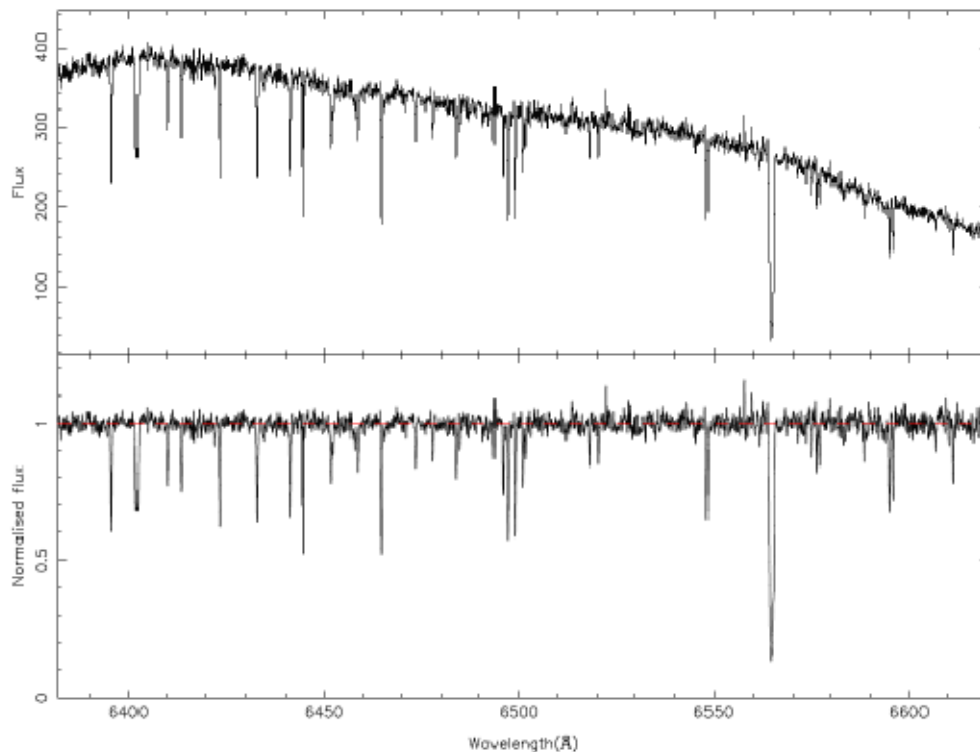


Figure 4-10: Example of automated continuum estimation and normalization using FLAMES benchmark HR test data.

4.3.3 Continuum Estimation

In a similar manner to the methods devised for optimising sky subtraction, iterative techniques for automating continuum estimation at both LR and HR exist (cf. Figure 4-10) and can be used to pre-normalize the spectra prior to more detailed analysis. Each spectrum is split into a line-only, and smoothly varying continuum-only component, using an iterative k-sigma clipped non-linear filter. Regions around selected strong lines, e.g., CaT or Mgb lines, can be optionally masked out, prior to filtering, to prevent the continuum tracking the wings of strong absorption features. The effective scale length of the filtering is here typically set to around 15\AA which, in conjunction with the masking and iterative clipping, is fine enough to follow continuum trends without being affected by the presence of other strong lines. At the same time an estimate of the overall signal-to-noise in the continuum is made by measuring the median continuum level in the analysis region and by measuring the pixel-to-pixel noise covariance matrix in regions containing no lines. The latter is needed to correct the apparent random noise for the cumulative smoothing effects of spectral interpolation and resampling, which we find typically results in a factor of ≈ 2 overall random noise reduction, and concomitant underestimation of derived parameter errors if not accounted for.

4.3.4 Velocity and EW Estimation

After normalizing by the computed continuum velocities are estimated by cross-correlating each spectrum with a model function template. We illustrate this for the CaT region where the template can be simply constructed using a zero-level continuum with three Gaussian absorption lines located at the vacuum rest wavelengths of the CaT lines superimposed.² Here the Gaussian line depths are scaled in the ratio 3:5:4 to reflect the different strengths of real CaT lines and all are set to have a full width at half maximum (FWHM) = 2.35\AA . An example of a continuum fitting to a Sculptor dSph K-giant spectrum together with the computed cross-correlation function and Gaussian fit to the peak is shown in Figure 4-9. As an alternative we have also used stellar model atmosphere spectra to provide excellent matching templates for velocity estimation.

An accurate estimate of the position of the cross-correlation peak is made by fitting a Gaussian to a localized region around the peak. This velocity is then used to define the wavelength region around each CaT line to use for EW estimation. After some trial and error we settled on a region 15\AA wide centered on each line as a reasonable tradeoff between including all the line flux and minimizing the noise in the simple integral estimator. In addition to the straightforward sum we also fit individual unconstrained Gaussian functions to each CaT line over the same wavelength region and use the derived flux as an alternative EW estimator. This also allows a semi-independent check on the accuracy of the derived

² Most of the weight in the least square fit comes from the core of the lines which are sufficiently Gaussian-like that a Gaussian fit provides an estimate close to the minimal rms error bound. Using more complex line profiles with correspondingly greater numbers of free parameters generally makes the rms error worse and is also more prone to wildly unstable solutions due to the inevitable presence of occasional artifacts in the data.

velocity by providing three separate velocity measures with associated errors. The weighted sum of these velocity errors provides the basic velocity error estimate for the velocity derived from the cross-correlation. We prefer to use the latter for the actual velocity estimate since it is effectively a constrained model fit. As a final step the derived velocity is corrected to a helio-centric system.

The combined equivalent widths for CaT lines #2 and #3 for both the integral and Gaussian fit are then compared and used to compute an overall correction to the Gaussian version. This is necessary since the real line profile is a complex function of many parameters, and in particular, the dampening wings visible in strong lines are distinctly non-Gaussian in appearance. This correction is equivalent to computing the average overlap integral between the real line profiles and the Gaussian fits and is accomplished by measuring the gradient between the two as a function of EW. We prefer to use the Gaussian-derived EW estimator since although the simple integral is unbiased it is also significantly noisier than a Gaussian fit.

4.3.5 Stellar Atmosphere Modelling

The general stellar atmospheric parameters that need to be estimated are: effective temperature T_{eff} , overall metallicity [m/H], systemic velocity V_{\odot} , microturbulent velocity V_{turb} and surface gravity $\log g$. By combining detailed broadband photometric measurements ranging from optical through near-infrared, with distance estimates and kinematic measurements, with global spectra properties we anticipate being able to quantify these parameters to the necessary precision to enable detailed abundance measurements of individual line species.

The most promising way forward involves extraction via line lists and direct EW measurements, combined with Maximum Likelihood model atmosphere template fitting using both Kurucz model atmospheres, as in Munari's extensive library or alternative stellar model atmospheres such as MARCS (Gustafsson et al. 2008). Additionally, we are exploring PCA/ICA decomposition methods to focus in on alpha-sensitive features in both LR and HR spectra, in conjunction with Maximum Likelihood model fitting to attempt automatic overall $[\alpha/\text{Fe}]$ estimation. An example of a model atmosphere fit is shown in Figure 4-11.

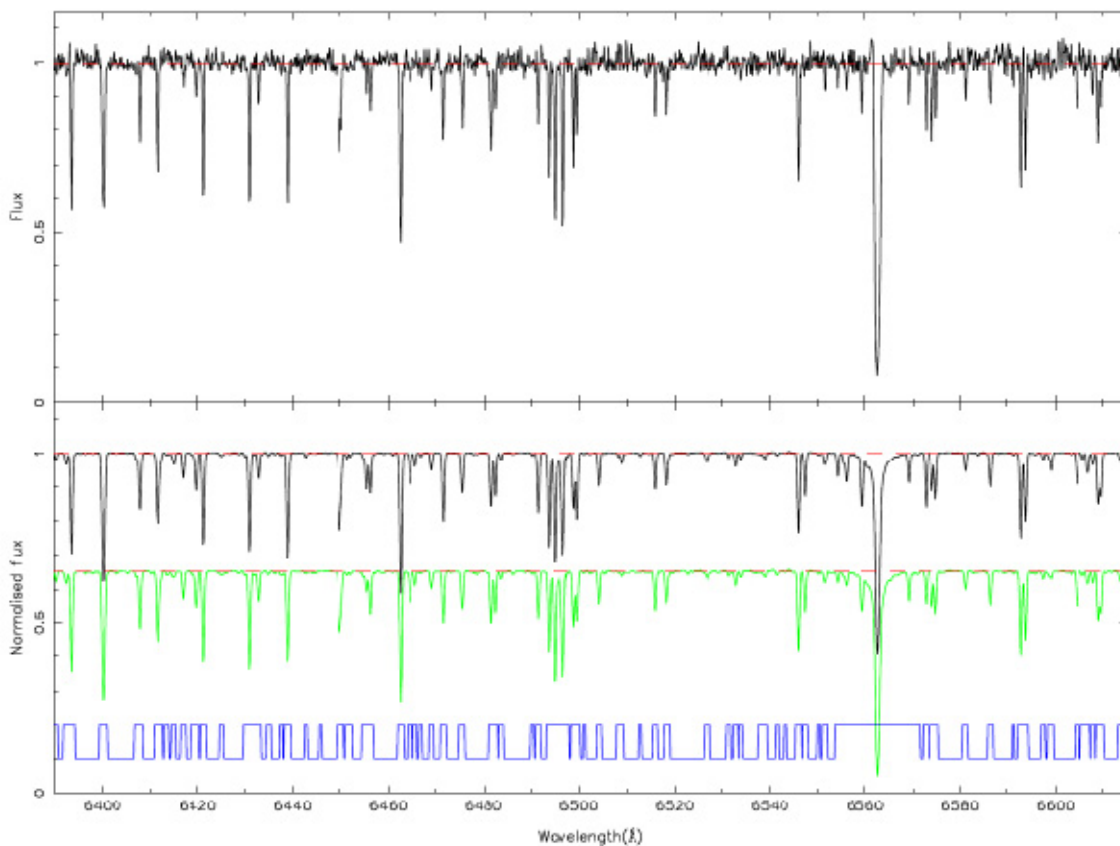


Figure 4-11: The best fitting continuum-subtracted model spectra for solar and alpha-enhanced abundance ratios compared to an HR VLT-FLAMES R=20000 continuum-subtracted spectrum with S:N $\sim 100/\text{\AA}$. Upper panel: continuum-normalized data; lower panel: top is alpha-enhanced model spectrum (black); middle offset solar ratio model spectrum (green); the mask function used in the fit is in blue. The solar abundance ratio spectrum gives a marginally better fit.

4.3.6 Chemical Tagging

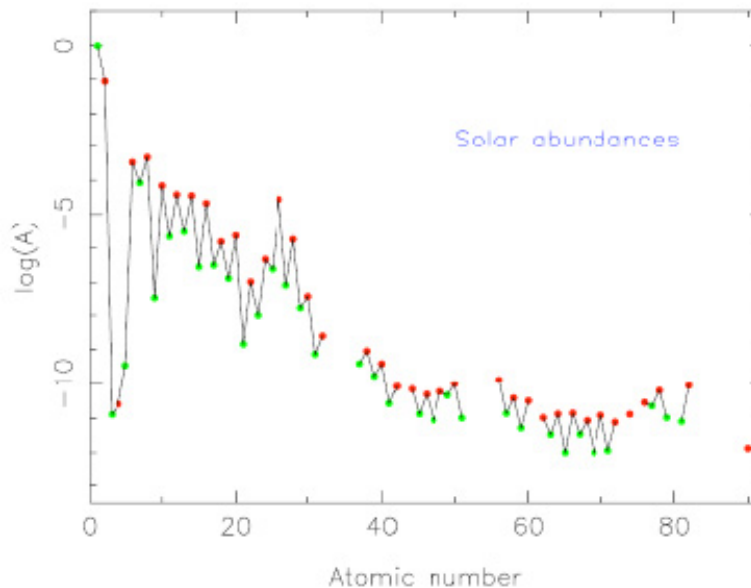


Figure 4-12: Example of chemical tagging for the solar spectrum

Stellar atmosphere modeling will result in a complete decomposition of the physical properties of the star and its chemical fingerprint (e.g., Figure 4-12). While a complete description of the chemical evolution within the Galactic environment is beyond this document, elements can be grouped in terms of their underlying physical processes, where the main categorization will be along the lines of the following:

- Light elements (e.g., C,N,O,Na,Mg,Al) are tracers of deep mixing patterns, found only in globular cluster (GC) environments, this gives a limit to the number of dissolved GCs in a stellar population. Evidence for differences in these ratios (to Fe) between field pop II giants and GC giants is shown, for example, in Pilachowski, Sneden and Kraft (1996); and Shetrone (1996).
- Alpha elements (e.g., O, Mg, Si, Ca, Ti) occur predominantly in SNeII,. The abundance of different alpha elements is sensitive to the mass of the SNeII progenitor, even Z alpha abundances limits the number of SNeII explosions and hence constrains the IMF /ejecta fractions with time
- Heavy elements ($Z > 30$) (e.g., Y, Ba, Ce, Sm, Eu) come from a mix of r- and s-processes *i.e.*, those beyond the iron peak formed by repeated neutron capture
- Rapid capture or r-process, occurs in high energy events such as in SNe explosions, e.g., Eu is thought to be produced almost entirely by the r-process
- Slow capture or s-process, probably in more quiescent situations, e.g., from stellar winds during AGB phase typical elements are Ba and La e.g., Ba/Eu is a measure of the contribution of AGB stars (note can be anomalous via self pollution but this causes large Ba/Fe ratio)
- Iron peak elements (V, Cr, Mn, Co, Ni, Cu, Zn) come mainly from SNeIa, *i.e.*, older binary systems so ratio of alpha to Fe gives leverage on SFH while Zn is a good tie in with high redshift

studies - also elements heavier than about Zn are predicted NOT to exist in zero metallicity stars - or those enriched purely by very massive first stars (especially pair production SN) another sign to look for. Cu is supposedly produced almost solely in SNe Ia

Note that the chemical decomposition will result in a high-dimensional parameter space and the application of clustering algorithms within this volume will be used to isolate populations with strongly similar chemical properties (and hence possibly from the same proto-stellar cloud); such identification is required to piece together the historical chemical evolution of the Galaxy. It is important to note that typical errors are 0.1 dex and the spread may only be 0.5 dex max. So this limits the likely detective work to ≈ 3 –5 divisions in each of the above tracer groups and even here many of these characteristics may be correlated. However, given so many different sites for chemical evolution the parameter space is still enormous and offers the potential to tag individual groups even in such complex regions as the Galactic Bulge (c.f. McWilliam 1997 and Tolstoy et al. 2003).

4.4 Competition

Although there is no direct competition with the same facility scope in terms of survey depth, spectroscopic wavelength coverage and resolution, there are several facilities either being used to conduct surveys or that will, or may, be available for GA-like surveys over the next 10-year period. We give a brief list of the main protagonists below to set the proposed WF MOS GA surveys in context.

- RAVE—is a southern hemisphere multi-fiber (150) survey of approximately 250,000 stars, with a possible extension to 1 million stars, at relatively bright magnitudes, $9 < I < 12$, being conducted on the 1.2-m UK Schmidt telescope in Australia (Steinmetz et al. 2006). The large field-of-view (6-degree diameter) and small aperture constrain the survey to bright limits and hence relatively nearby (5–10 kpc) stellar populations. The wavelength range, 8430–8740 Å, and resolution, $R=8500$, are similar to the planned Gaia spectroscopic survey. The survey began in 2003 and is designed to run for 5–10 years depending on final scope.
- Keck DEIMOS—although DEIMOS is a general purpose multi-slit (120) spectrograph it has been used for studies of nearby resolved stellar populations by several groups, mainly in the CaT region with a wavelength coverage of 2500 Å at a resolution of $R = 6000$. Its main advantages are the high overall throughput, $\approx 29\%$, 10-m aperture and reasonable field-of-view, 81.5 arcmin². This is well matched to studying nearby satellite systems such as small dwarf galaxies and globular clusters around the Milky Way and M31 (e.g., Simon & Geha 2007) and has been extensively used by two groups to probe the kinematics and overall metallicity of substructure in and around M31 and M33 (e.g., Ibata et al. 2005; Kalirai et al. 2006). Although the field-of-view is impressive for a 10-m-class telescope it is nowhere near large enough to efficiently map the stellar populations of either the Milky Way or the general M31 system, and it does not support a multi-object high-resolution mode.
- BRAVA – The Bulge Radial Velocity Assay program is being undertaken on the 4-m CTIO HYDRA, using 138 fibres to target 2MASS-selected M-giants in the Bulge at $R \sim 2800$, with the goal of mapping the kinematic structure of the Bulge and Bar. The current survey focuses on a

strip along $b \sim -4^\circ$, with a vertical extension at $l = 0^\circ$, each field covering 40 arcmins. With more than 3300 stellar velocities to date, this survey has published its initial results (Howard et al. 2008).

- FLAMES—is a multi-object fiber (130) spectrograph on one of the ESO VLTs with a 30-arcmin diameter field-of-view. In GIRAFFE mode it offers a similar set of resolution options in LR mode ($R \approx 6000$) and HR mode ($R \approx 20000$), to those proposed here for WF MOS. However, the limited wavelength coverage per setting, particularly in HR ($\approx 250 \text{ \AA}$), together with the wider field-of-view and number of fibers, gives WF MOS a 20–50 multiplex gain over FLAMES. As with Keck this setup has been used for a variety of studies of resolved nearby stellar populations with two of the ESO Large Programmes of particular note (e.g., Tolstoy et al. 2004; Koch et al. 2006). In some respects this is acting as a pathfinder system for trialling the approach we are proposing for the GA case.
- Magellan MIKE—is a double echelle spectrograph that gives simultaneous coverage in the blue (3200–4800 \AA) and red (4400–10000 \AA) wavelength regimes at resolutions of 19000 and 25000, respectively, over a 30-arcmin diameter field. In multi-fiber mode up to 256 objects can be simultaneously observed if suitable order blocking filters are used to select specific wavelength intervals (typically $\approx 200 \text{ \AA}$ wide). It has been extensively used to study stellar populations in southern Milky Way satellites (e.g., Walker et al. 2007). IMACS, a lower resolution imaging spectrograph, appears to have been mainly used for deep extragalactic projects, though in principle could be used for LR nearby stellar population studies. The limitations of both spectrographs relative to WF MOS are similar to FLAMES.
- AAOmega—on the 3.9-m AAT has the benefit of a 2-degree field-of-view and has two spectrographs fed from 392 fibers giving selected simultaneous blue and red wavelength coverage in the range 3700–9500 \AA . For stellar studies the relevant comparison is with the $R=8000$ –10000 gratings which allow simultaneous coverage of the Mgb (5100–5450 \AA) and CaT (8450–8850 \AA) regions. A modest survey of the Galactic Bulge region of some 20000 stars with $V < 18$ begun in 2008 is making a start on a chemo-dynamic analysis of the central regions of the Milky Way.
- SDSS/SEGUE I/II—primarily designed for galaxy redshift surveys, the 2.5-m SLOAN survey telescope has already been used for a sparse sampled stellar spectroscopic survey over large patches of (mainly) high galactic latitude sky. Although providing fascinating insights into the bulk distribution of Galactic components (e.g., Allende Prieto et al. 2006), the low resolution, $R=2000$ and the small telescope aperture preclude detailed investigation of stellar subcomponents. Future planned Galactic surveys include extending SEGUE I-II and an APOGEE H-band Bulge survey from 2009.
- LAMOST—is 4000-fiber spectroscopic survey instrument housed on a 4-m Schmidt telescope with a five-degree field-of-view (first light October 2008). It is expected to begin surveys during 2009/10/ and one of its main aims is to carry out a large area spectroscopic survey of the Milky Way. In survey mode the resolution will be relatively low, $R=1000$ –2000, and blue and red arms will give a wavelength coverage of 3700–5900 \AA and 5700–9000 \AA . The LR survey spectrographs have been optimized for galaxy redshift surveys and although it will compete effectively with the SDSS stellar surveys, again it will not have high enough survey resolution to carry out the main GA WF MOS programs.

- Gaia—the RVS component of Gaia will conduct an all-sky $V < 15$ survey from 2011/12 and then from a full combination of scans by 2020 the aim is to attain $V < 17$. The wavelength coverage will be limited to the CaT region, in this case 8450–8750 Å, at a resolution of $R=10000$. As noted earlier this and the astrometric goals of Gaia complement the proposed WF MOS LR surveys for kinematics and overall metallicity measures, while the WF MOS HR survey would provide detailed abundance analysis.
- HRMES—is a proposed 392-fiber $R = 30000$ spectrograph to be deployed on the 2DF positioner on the AAT. It is being designed to cover two 150-Å wide bands simultaneously and aims for first light in 2012. One of its primary science drivers is HR studies of nearby stellar populations.

5 GALAXY FORMATION AND LARGE SCALE STRUCTURE

5.1 Introduction

As introduced in §1.2, WF MOS has enormous potential beyond the original two DE/GA campaigns envisaged by Gemini Aspen process. Following presentations made at two recent conferences, it is clear that Japanese astronomers are excited by utilizing this instrument for many additional surveys. Establishing early synergy between the science potential envisaged by Japanese astronomers and our proposed design will enhance the likelihood that WF MOS is enthusiastically accepted within the broader Japanese community.

The earlier WF MOS Feasibility Study already discussed the broader potential of the Dark Energy survey, considering ‘value added science’ that would be possible exploiting the large $z \sim 1$ and $z \sim 3$ spectroscopic surveys for non-cosmological applications. In this section, we take the discussion further, however. Here we discuss *additional surveys* that might be undertaken with WF MOS, including some of those presented at the recent *Cosmology: Near and Far – Science with WF MOS* conference at Kona HI (May 2008). The key issue we wish to address is the extent to which these are compatible with the science requirements defined by the DE and GA surveys.

In compiling this brief review of additional surveys, we acknowledge useful input from a number of Japanese astronomers (M. Ouchi (convenor), T. Yamada, T. Kodama, M. Tanaka and K. Shimasaku).

5.2 Strategic Issues

By design the now-funded panoramic imager HyperSuprimeCam (HSC) has same field of view as WF MOS. Synergy between target imaging and subsequent spectroscopic follow-up is long-standing in astronomy and extends well beyond DE/GA applications. To date, it has been difficult to fully exploit the remarkable imaging capabilities of the existing Suprime-Cam imager because its 30 arcmin field is larger than the spectroscopic facilities available to the Japanese (e.g., FOCAS, GMOS, DEIMOS). This has certainly limited the potential discovery space of Subaru. The unique combination of HSC+WF MOS will rectify this problem over a wide range of science applications. As plans for the use of HSC materialize it is clear that this imager will undertake deep surveys other than just ones concerned with weak lensing discussed in §3.6; exploiting these with WF MOS will be an essential application.

There is an explosion of international interest in conducting surveys spanning areas of $\sim 10 \text{ deg}^2$ or greater. These include ultradeep imaging over moderate fields with 4 m telescopes (UKIDSS, VISTA) and ambitious campaigns with Spitzer, Herschel and future non-optical/IR facilities. We are seeing a revolution in multi-wavelength applications in astronomy and it is guaranteed that WF MOS will be an unique asset in this territory.

5.3 Sample Science Programs

Extensive redshift surveys have already been undertaken with 8-10 meter class telescopes. These include the color-selected Keck DEEP2 survey of $\sim 40,000$ galaxies with $0.5 < z < 1.3$ limited at $R < 24.1$, and the VLT VVDS survey which aims to survey 150,000 galaxies to $I = 24$. These are both multi-slit surveys offering better sky subtraction than WF MOS is likely to achieve with fibers and providing limited resolved data, e.g., for galaxy rotation curves.

The key gain of WF MOS, in concert with HSC, with respect to these earlier surveys will be to span much larger areas for rarer sources and perhaps to offer higher signal to noise for larger samples of brighter sources. Cosmic variance continues to plague statistical studies of galaxy evolution and WF MOS offers the potential of efficiently eliminating this uncertainty. Table 5-1 provides a useful overview of the potential applications of WF MOS beyond the confines of the earlier DE/GA applications.

Table 5-1: The Range of Survey Areas and Potential Applications

Survey Area	Comoving Volume (Mpc ³ /unit z) $1 < z < 10$	Main Targets
1 deg ²	$\sim 10^7$	Galaxy Evolution
10 deg ²	$\sim 10^8$	The most luminous objects, clusters large scale structure
100 deg ²	$\sim 10^9$	QSOs, cosmic web
1000 deg ²	$\sim 10^{10}$	Dark Energy Survey

It should also be remembered that surveys can be combined very effectively so that e.g., an imaging survey for WL and spectroscopic one for DE can, with minimal difficulty, encompass other applications and simultaneously cover (rarer) targets. Although some of the sources involved are faint, many have emission lines and stacking statistical samples may be powerful if limitations arising from sky subtraction can be addressed.

The following will serve as an illustration of the possibilities. They demonstrate that the wavelength range and resolution proposed for the GA/DE surveys is compatible with these additional applications. The programs discussed below are intended to sample the nested hierarchy of field areas listed in Table 5-1. We do not cost the execution of these surveys in our proposal.

5.3.1 A High Quality Spectroscopic Survey to $z \sim 1.6$

As the primary baryon oscillation survey at $z \sim 1$ (§3.7.2) is optimized for emission line galaxies with [O II] detections, the continuum signal/noise in a typical spectrum will be very low. The goal of that survey is to measure the redshifts of millions of galaxies in the most efficient manner possible. Thus, despite claims in the Feasibility Study, we believe it is unlikely that the main DE survey will generate spectroscopic data that is adequate for precision studies of galaxy properties (stellar populations, ages, metallicities etc).

An interesting proposal, therefore, is to exploit WF MOS to secure, for a much smaller area than that studied by the DE campaign, higher quality spectra for the purpose of more detailed galaxy studies

beyond $z \sim 1$. Such a mini-survey would complement FMOS H α emission line data secured in the same selected areas.

We have developed tools for predicting model WF MOS spectra as a function of the exponentially-declining star formation rate timescale τ and the metallicity Z . This allows us to evaluate the increased signal/noise that would be necessary to recover these valuable parameters. Figure 5-1 provides an illustration of this for a red I~22 $z \sim 0.7$ galaxy observed in the DE survey and that with a longer exposure achieving a continuum signal/noise of ~ 10 .

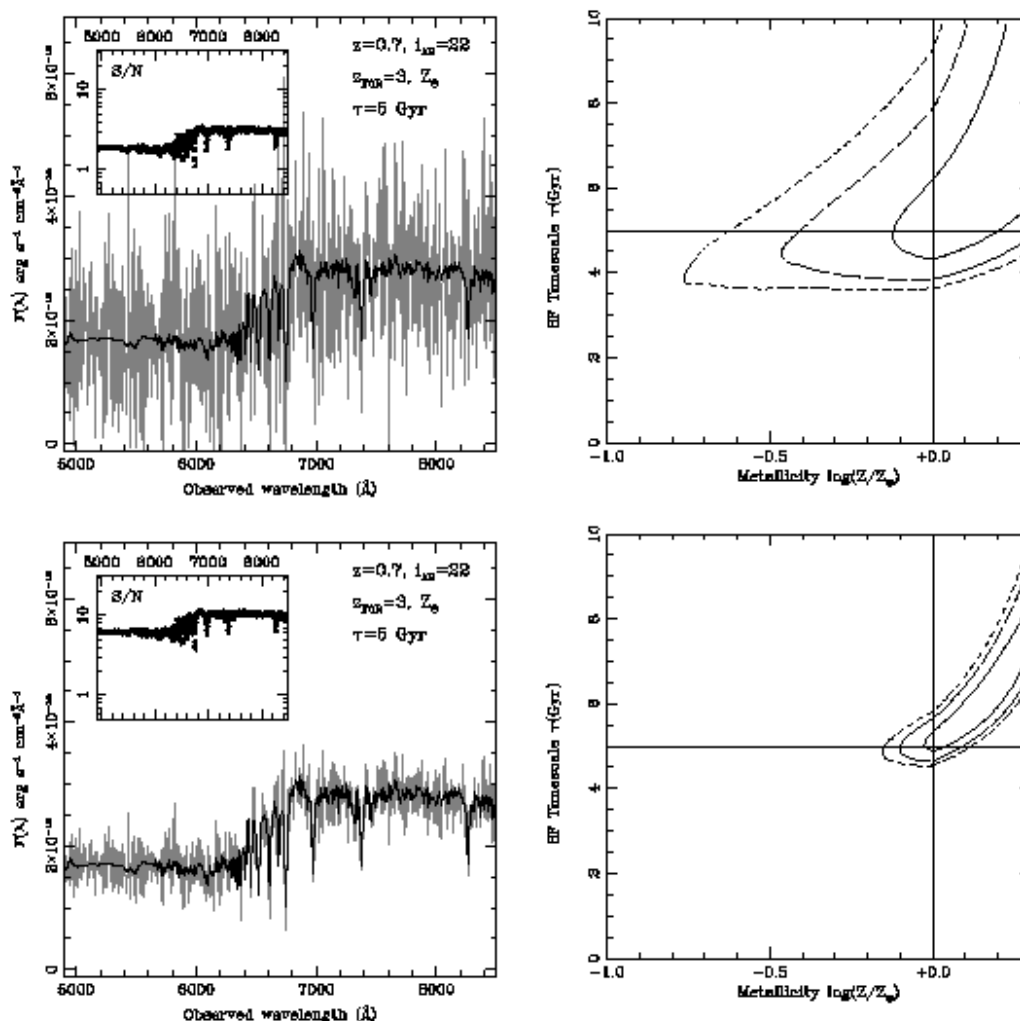


Figure 5-1: Recovering the star formation timescale (τ) and metallicity Z for a red I~22 $z \sim 0.7$ galaxy. The top panel refers to a low signal/noise spectrum such as that achieved for a dark energy survey of luminous red galaxies; the data is sufficient to secure the redshift but little more. The bottom panel refers to a much higher signal/noise spectrum such as would be possible with longer integrations on brighter objects ($R \sim 21$) over a wide area. In conjunction with an earlier survey by FMOS, it is proposed WF MOS could secure robust stellar properties for a large sample of bright galaxies over $0.7 < z < 1.6$.

5.3.2 Studies of $z > 3$ galaxies

Subaru has pioneered the statistical study of both Lyman break galaxies (LBGs) and Lyman alpha emitters (LAEs) beyond a redshift 3. It is clear the HSC will significantly advance this area and WF MOS can complement the relevant imaging campaigns by providing confirmatory spectroscopy and emission line statistics. As a key issue will be the depths achievable with a multi-fiber instrument; it is likely that most applications will be restricted to sources with strong Lyman α emission.

The surface density of luminous LBGs with $I < 24$ varies from 1400 deg^{-2} at $z \sim 3$ to $\sim 100 \text{ deg}^{-2}$ at $z \sim 5$. Photometric and narrow-band selection has enabled the mapping of LBGs and LAEs in a few selected areas over 200 Mpc scales (Figure 5-2) enabling their clustering and inter-relationship with other sources (e.g., sub-mm galaxies) to be determined. For the subset with strong emission lines, WF MOS would significantly enhance such surveys over very much wider fields.

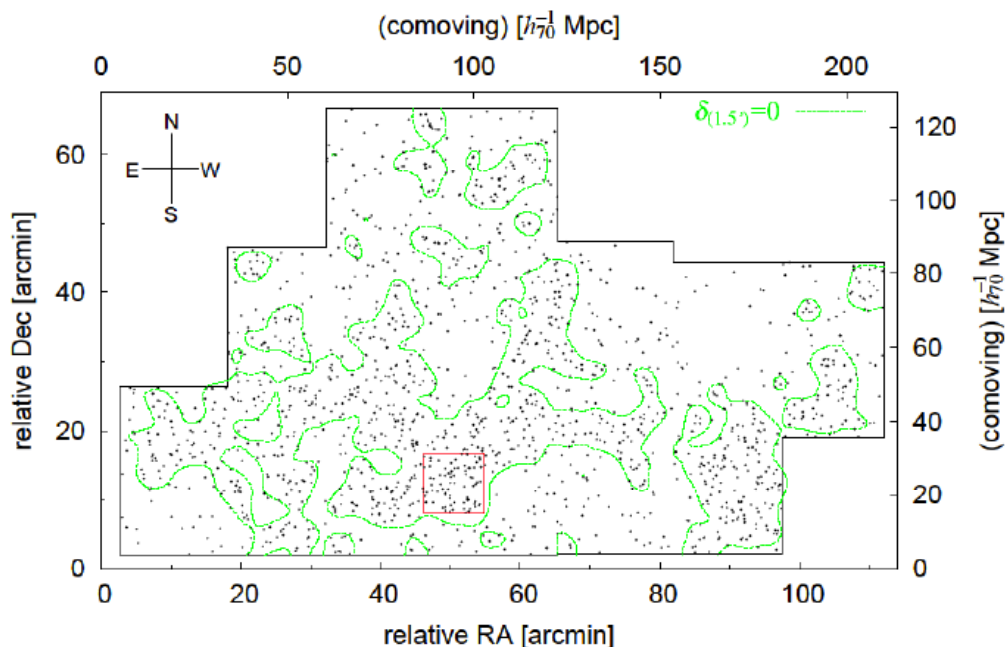


Figure 5-2: The spatial distribution Lyman alpha emitters in the well-studied SSA22 field (preliminary results from the ongoing survey, courtesy of Yamada et al). WF MOS, working in concert with HSC, would enable a huge increase in survey mapping speed and provide emission line statistics for yet larger samples.

WF MOS spectroscopy will yield the equivalent width of Ly α for both LBGs and LAEs and this can act as a valuable tracer of young stellar populations. By stacking spectra for selected higher redshift sources, the rare He II tracers of Population III stars can be sought. Line profile measures will also become feasible with WF MOS for the most luminous examples. Stacking spectra will increase the possibilities in redshift ranges where sky subtraction is straightforward, providing valuable insight into outflows and the nature of the local IGM (Figure 5-3).

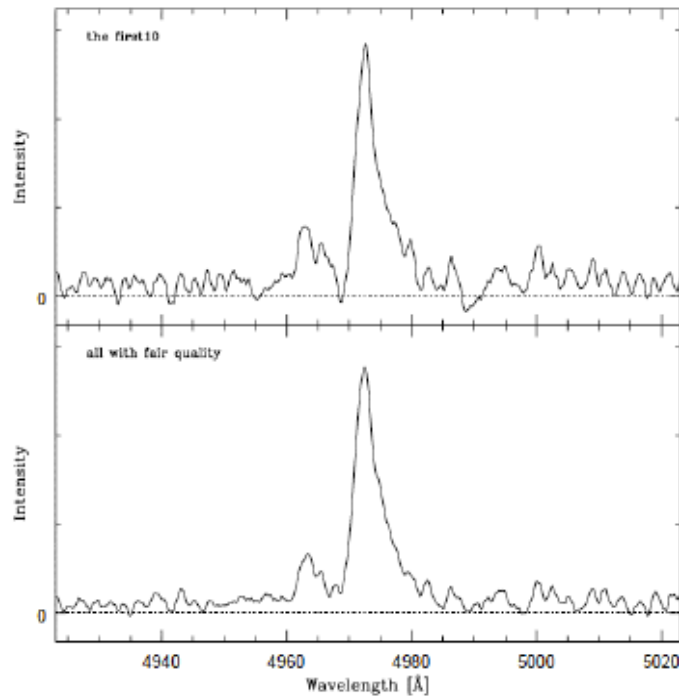


Figure 5-3: Stacked Lyman alpha line profiles for emitters located from Suprime-Cam narrow band imaging (from the ongoing survey by Yamada and co-workers). Line widths and profile shapes constrain outflow models and the nature of the local intergalactic medium.

5.3.3 QSOs, Clusters, and Other Sources

The unrivaled field of WF MOS means that very rare sources such as luminous QSOs will still be abundant within a given pointing and thus correlations between intervening absorbers and Lyman break galaxies will be possible over large scales. This is a key motive for a wide field spectrograph on the next generation of extremely large telescopes, but an early application with less dense sampling with WF MOS will be highly instructive.

Intermediate redshift clusters of galaxies are likewise natural targets for WF MOS. It is now thought that infalling field galaxies suffer changes to their star formation rates, morphologies and halo properties as they become influenced by the intracluster gas and the cluster potential. Spectroscopy is crucial for membership and post-burst age diagnostics. The panoramic field of WF MOS will accelerate progress dramatically in this area (Figure 5-4).

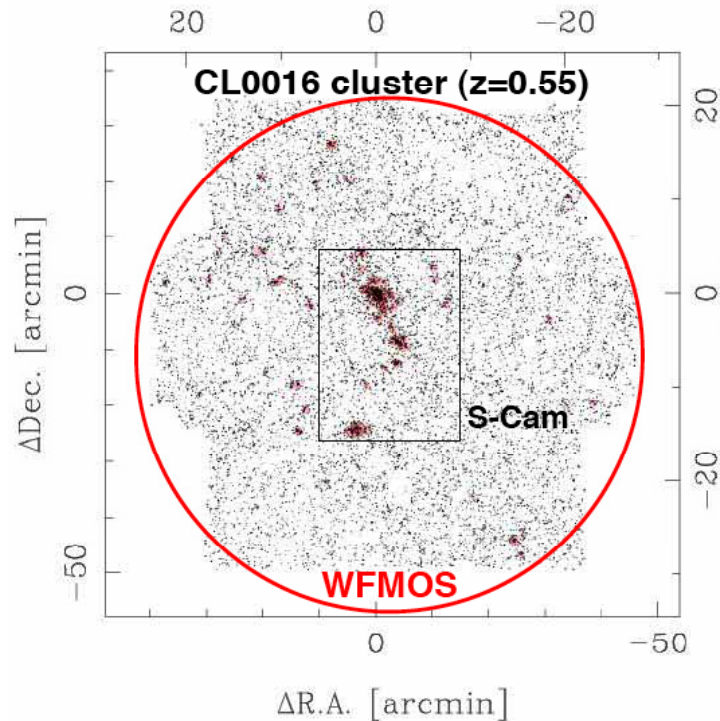


Figure 5-4: Panoramic spectroscopy of clusters of galaxies at intermediate redshift (courtesy of Tanaka & Kodama and collaborators). The turn-around region for galaxies falling into a rich $z\sim 0.5$ cluster corresponds to a diameter of $\sim 15\text{--}20$ Mpc and fits neatly within a single WF MOS pointing. Detailed spectroscopy provides velocities and star formation diagnostics for thousands of members per cluster. This will enable a variety of studies which attempt to understand how the cluster environment both enhances and truncates star formation and rearranges the galaxy morphologies.

5.3.4 Implications for Instrument Design

The above programs illustrate the broader potential of WF MOS beyond the confines of the more substantial DE and GA surveys. It is interesting to ask whether they can be conducted efficiently with the same requirements.

Fiber aperture: (currently 1.2 arcsec) this is regarded as adequate for a $z < 1.6$ redshift survey, the cluster and QSO applications. Although smaller fiber apertures would be desirable for the high z LBG and LAE applications, good progress is still possible with the current fiber aperture.

Wavelength coverage: (currently 4200–9700 Å). The red extension required for the $z\sim 1$ DE survey is highly advantageous for the Japanese; it maximizes synergy with the red sensitivity of HSC and ensures Ly α is visible to the highest redshifts practical.

Spectral resolution: (currently 3500–4000 across the full range, 20,000 in two selected regions, 5000 around Ca triplet). This is adequate for all the applications discussed above.

6 TECHNICAL DETAILS

6.1 Introduction

In this section we collate a variety of technical materials that would have interrupted the flow of science discussion in Sections 3–5. The discussion includes important issues such as the required imaging data and photometric methods to be used for target selection for the DE surveys, simulations of sky subtraction without ‘nod and shuffle’, fiber allocation efficiencies and how these impinge on survey strategies, and exposure time calculations which govern the eventual Subaru observing time requests.

6.2 Target Catalogs – Dark Energy Surveys

First we outline the planned and ongoing imaging surveys that will become available for target selection for the DE campaign. We then define a plan of how target selection should proceed given our current knowledge of these surveys and their data policies. The relevant surveys include CFHTLS-Wide, KIDS, Dark Energy Survey (DES), Pan-STARRS1 and HyperSuprimeCam (HSC) surveys. Where it is known, the sky coverage of these is summarized in Figure 6-1.

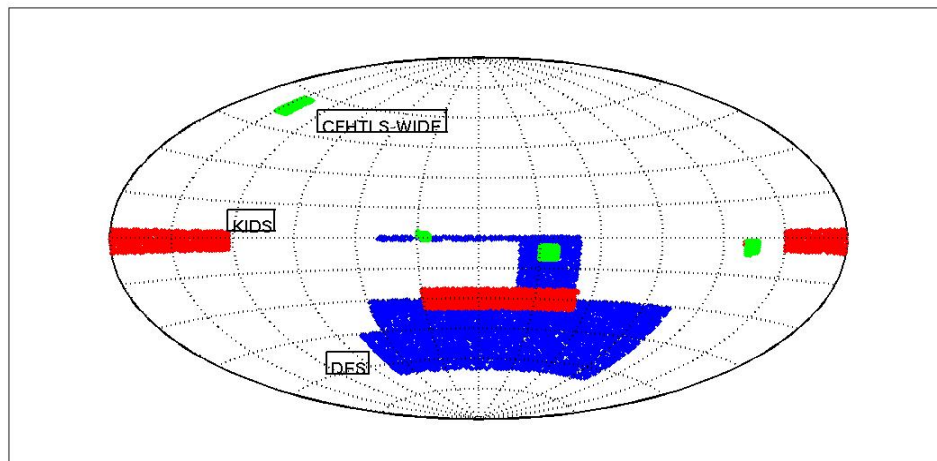


Figure 6-1: Sky coverage for DES (blue, 5000 deg²), KIDS (red, 1500 deg²) and CFHTLS-Wide (green, 150 deg²). Pan-STARRS (omitted for clarity) will map 3π steradians seen from Hawaii. HSC coverage is not yet decided.

We first give a brief description of each survey:

- **CFHTLS-Wide** (the Canada-France-Hawaii Telescope Legacy Survey Wide): This survey is ongoing and is planned to cover 150 deg² in *ugriz* over four different fields. The CFHTLS-Wide survey should be completed in the next few years and has already a considerable amount of data publicly available. Contrary to most planned surveys the CFHTLS has a considerable depth in the bluer filters including a u band photometry planned to a depth of 26.4 AB.

- **KIDS** (the Kilo-Degree Survey): This will cover 1500 deg² in *ugri* and 2800 deg² in *z* by utilizing the VST/OmegaCAM in Chile. KIDS will cover two regions on the sky: an equatorial strip on the North Galactic Cap and a patch around the South Galactic Pole. The same area will also be covered by VISTA in *JHK_s*. The expected magnitude limits are given in Table 6-1. The VST has seen major delays in its commissioning, but survey operations are now expected at the end of 2009 (Bender, private communication).
- **DES** (the Dark Energy Survey): This international collaboration (US-UK-Spain-Brazil) will use the Blanco 4m telescope in Chile. It will image the sky with five filters: *griz* and *Y* bands. The instrument will be used down to $i = 24$ (see Table 6-1) over approximately 5000 deg² of the Southern sky during 2011-2016. In addition VISTA Hemisphere Survey will map the same area as DES in *J*, *H* and *K_s*. This will provide significant improvement in the derived photometric redshifts for $1.3 < z < 2$ (e.g., Banerji et al. 2008).
- **Pan-STARRS**: The Pan-STARRS observatory in Hawaii will have four 1.8 m telescopes, with *grizy* and *w* filters (but not *u*). The optics delivers a 3 deg field of view. The first telescope of Pan-STARRS achieved first light in 2007 and has undergone an extensive commissioning process during 2008. The camera and telescope have passed a formal Operations Readiness Review, and full survey operations are expected from April 2009. Pan-STARRS1 will pursue a 3π survey of the sky observable at Hawaii during the following 3.5 years.
- **HyperSuprimeCam (HSC)**: With its field of view matching the WF MOS field of view, and a planned survey, which will precede the WF MOS surveys, it is also the only camera located on an 8m aperture appropriate for target selection. Although the survey is not yet confirmed it is likely to be 2000 deg² to depths listed in Table 6-1.

We note that the latitude of Hawaii (the site of Subaru) is +18°, while the imaging surveys will be taken from either Hawaii (Pan-Starrs or Subaru) or from Chile (KIDS or the Dark Energy Survey), at latitude of about -30°. Clearly a considerable fraction of the surveys obtained from telescopes in Chile will not be observable by Subaru.

Table 6-1: Planned imaging surveys: AB magnitude limits per SDSS-like filter. Depths are taken from various survey websites. HSC depths follow a private communication (Takada)

Band	DES	KIDS	PanStarrs1	HSC	CFHTLS
u	NA	24.1	NA	NA	26.4
g	24.6	24.6	24.35	26.5	26.6
r	24.1	24.4	23.85	26.4	25.9
i	24.3	23.4	23.05	25.8	25.5
z	23.9	22.4	22.45	24.9	24.8
Y	21.5	NA	21	23.7	NA

6.3 Strategy for Target Selection

The aim in the BAO survey at $z \sim 1$ is to concentrate on [OII] emitting objects at $0.7 < z < 1.6$ over a 3200 deg² area. The minimum photometric selection should thus be sufficient to locate the galaxy in a broad redshift bin. This problem was effectively solved using only BRI photometry ($B_{AB} < 24$, $R_{AB} < 23$ and $I_{AB} < 25$) in the DEEP2 survey for galaxies with $R_{AB} < 24$. As outlined in Section 3, as we are selecting galaxies with $R_{AB} < 23.0$, the depth requirements should be less demanding than for the DEEP2 survey by

roughly a magnitude. We show a simulation of this selection Figure 6.2 where galaxies can be clearly separated into 2 broad redshift bins above and below $z \sim 0.7$.

Each of the surveys discussed above will yield a photometric redshift accuracy superior to that defined by BRI photometry, as is illustrated by the photo- z precision of the DES survey shown in Figure 6.2. Therefore, for the low redshift DE survey the key issue is whether the imaging is located in a suitable part of the sky with sufficient area, and whether the data is available to the WF MOS team.

Our $z \sim 1$ DE survey requires 3200 deg² observable from Subaru with suitable imaging. We conclude that 2000 deg² of imaging required be taken from the HSC survey which will be completed previous to the WF MOS survey. An additional 1200 deg² would be equatorial and taken from the 3π survey produced with Pan-STARRS.

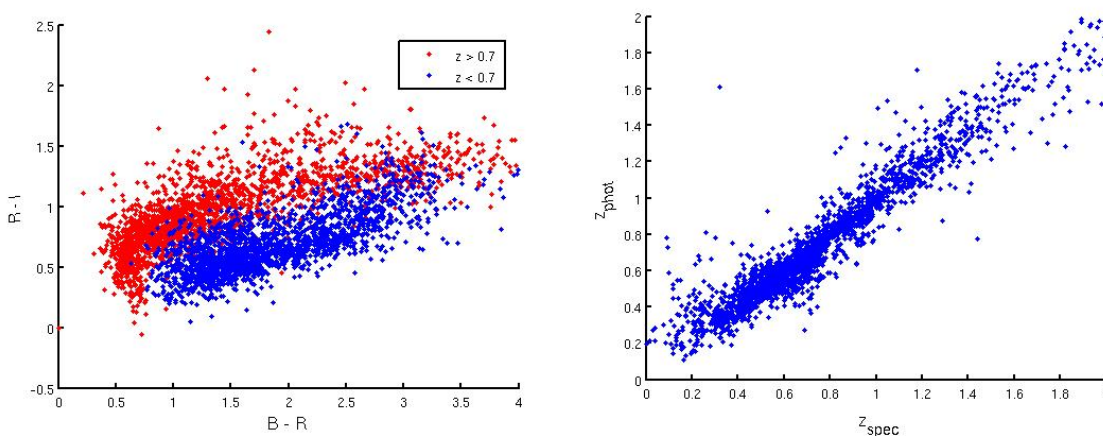


Figure 6-2: (Left): Photometric selection from the DEEP2 survey: red and blue points represent galaxies above and below a redshift of 0.7 respectively, based on BRI photometry alone. (Right): Simulation illustrating substantially improved photometric redshifts expected for the Dark Energy Survey (grizY filters) combined with the VISTA Hemisphere Survey (JHK filters). Deeper data such as that possible with HyperSuprimeCam would further improve the accuracy.

The high redshift DE survey will target Lyman break galaxies with $2.5 < z < 3.3$. In this case a Steidel-like selection ($R_{\text{AB}} < 24.5$ $G_{\text{AB}} < 25.5$ $U_{\text{AB}} < 26.5$) is required. Most planned surveys (DES, Pan-STARRS, KIDS and HSC) will not deliver data as deep as required in the ultraviolet. If one were to obtain the U band data directly from HSC it would take a further 15-20 clear nights of survey time for target selection over 100 deg². Fortunately, the CFHTLS-Wide has obtained significant (~ 150 deg²) imaging with u band depth suitable for the $z \sim 3$ target selection ($u' = 26.4$, $S/N = 5$, 1.5 arcsec aperture).

We recommend that 100 deg² of ultraviolet imaging required for target selection for the high redshift survey be taken from the CFHT-Wide survey which is partially completed and will be finished before the WF MOS survey starts. The longer wavelength data will be derived from the HSC weak lensing surveys. A further 15 to 20 clear nights would be needed if the required ultraviolet imaging were done at Subaru.

Clearly, we would prefer Subaru HSC imaging datasets as the material for WF MOS targets. This is still possible in principle; although, our $z \sim 1$ survey requires over 3000 deg^2 of coverage, which will probably exceed the expected 2000 deg^2 weak lensing survey field area. Among the other datasets described in this section to augment the material, KIDS is an ESO public survey. Similarly the raw DES data should become public after a year of being taken. We have team members who have access to both the DES and Pan-STARRS survey data. Via future agreements these imaging data should be available to the WF MOS team. Some of the CFHT U band data required for the $z \sim 3$ survey are already available to the community, and we can expect the full 150 deg^2 should be available prior to the commencement of a WF MOS survey.

6.4 Predicting Emission Lines from Broad-Band Photometry

Although a multicolor (e.g., BRI) photometry cut is effective in selecting galaxies higher than redshift 0.7 for our $z \sim 1$ DE survey, a further selection in this (or another) color plane can yield samples of blue galaxies with prominent emission lines. We have investigated how to improve this selection by applying non-linear statistical methods to the ensemble of DEEP2 galaxies.

Provided with magnitudes (BRI in the case of DEEP2, or *ugriz* magnitudes if available), magnitude errors and [O II] EWs for a subsample of galaxies, we have shown that it is possible to improve the selection by using a non-linear correlator such as a neural network (cf. ANNz; Collister & Lahav 2004) which can usefully predict the emission line strengths (Figure 6-3). This technique will significantly increase the efficiency of looking for emission line objects ahead of WF MOS spectroscopy, particularly given the likelihood of improved multicolor data from KIDS, DES, Pan-STARRS or HSC. For photometry in the BRI bands as in the DEEP2 target selection catalog, a predicted scatter on the log of the equivalent width of 0.21 can be achieved. This should improve with more bands (including U) and should also improve if these bands are deeper as shown by Abdalla et al. (2008).

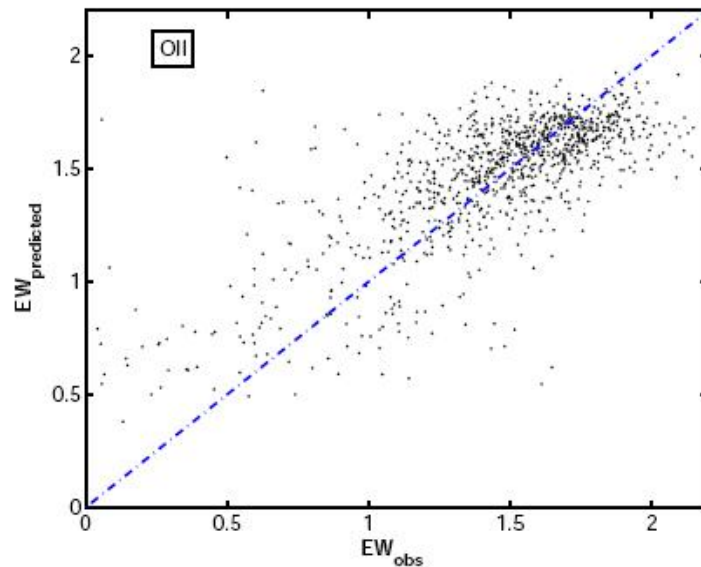


Figure 6-3: Neural network prediction of the [OII] equivalent width given BRI data used to pre-select DEEP2 galaxies. With more bands it will be possible to improve this performance.

6.5 Spectroscopic Simulations – Dark Energy Surveys

We now turn to a more rigorous estimate of the exposure times necessary to retrieve reliable redshifts for the low and high redshift DE surveys. This is done by simulating galaxy spectra with different signal to noise ratios and attempt to retrieve their redshifts.

For the low redshift survey we simulate a galaxy at $z = 1.5$ and concentrate on the [OII] doublet. We proceed in two ways: we compute simulated spectra and fit the line directly and also determine a figure of merit to determine the redshift. Both approaches agree on the signal to noise required.

In order to find a figure of merit to determine the redshift, the Figure 6-4 (Right) shows our definition of “Significance.” We measure the flux within two windows centered in the 3726 Å and 3729 Å lines, width ± 1 Å (shaded region). For each choice of redshift we compare the flux in these regions as a ratio of the RMS of the continuum flux in the same spectral region. The product of ratios for the blue and the red lines of the doublet is equivalent to a conditional probability of having both lines detected. From these low redshift simulations we find a minimum signal to noise of 7 for the [OII] line is necessary for a correct determination.

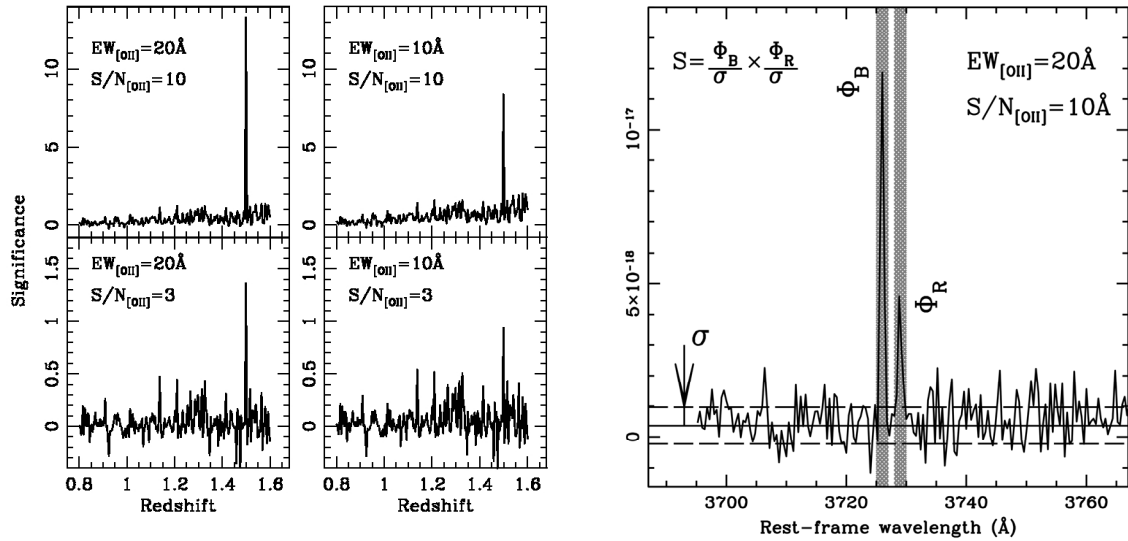


Figure 6-4: (Left) Simulation of WF MOS spectra using realistic sky subtracted noise. We show as an example a galaxy at the high redshift end of the range for the $z \sim 1$ DE survey. (Right) Illustration of the significance needed in order to confirm that the line is indeed [OII].

For the high redshift survey we simulated three possibilities:

- (a) The redshift is detected by the line emission ($\text{Ly}\alpha$)
- (b) The redshift is detected by the Lyman break
- (c) The redshift is detected by absorption lines seen in a prominent continuum

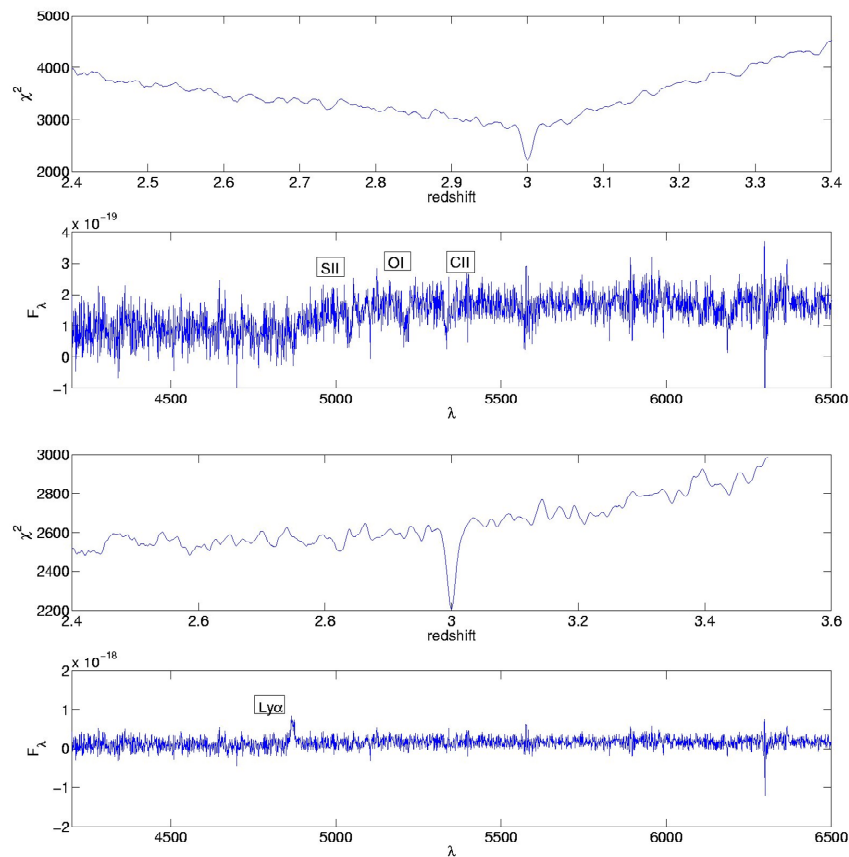


Figure 6-5: Simulations of high redshift Lyman break galaxies in two different cases: via absorption lines (top) and via Lyman alpha emission (bottom). The absorption line detection requires a continuum signal to noise of four and the emission line detection requires a continuum signal to noise of one.

Our simulations indicate that redshifts can be secured through either absorption or emission line properties. A continuum signal to noise ratio of four is required for the former, but a much smaller integration time would be needed for galaxies with Ly α emission.

According to Shapley et al. (2005), 25% of LBG have a Ly α line strength comparable to the simulated galaxy with $EW = 20$ in Figure 6-5. Hence a practical proposition is to proceed with multiple exposures which would combine to provide a continuum signal to noise of four, reconfiguring on the fly as emission line sources are detected in individual sub-exposures.

6.6 Target Catalogs – Galactic Archaeology

Provision of suitable source catalogs for the main GA surveys is straightforward due to the relatively bright photometric depths that define the main surveys.

All-sky coverage in the near-infrared is already provided by 2MASS (Cutri et al. 2003) which is an excellent source of J,H,K photometry for selecting relatively clean samples of the redder K- and M-giants out to ≈ 100 Kpc. More recent large area surveys being conducted on UKIRT using WFCAM

(e.g., Lawrence et al. 2007), and shortly to begin with VIRCAM on VISTA, will provide essentially complete coverage at signal-to-noise of 10:1 to $K=18$, $H=19$ and $J=20$ for all GA regions of interest.

In the optical these surveys are already supplemented by existing SDSS u,g,r,i,z coverage of over 10,000 sq degrees of mainly Northern hemisphere locations with a survey depth equivalent to $V = 22$ at signal-to-noise of 10:1 (e.g., Adelman-McCarthy et al. 2008). The SDSS Segue extensions can also be used for general object selection in lower latitude regions. In the southern hemisphere using the VLT survey telescope VST, several public surveys, including a large area Galactic Plane survey and a large area high latitude survey are due to begin at the end of 2009 and will survey to at least a comparable depth as SDSS in the North.

The region around M31 and M33 is being targeted in the PAndAS project (PI Alan McConnachie) using MegaCam on the CFHT to image in g- and i-band to AB magnitudes of 26 and 25 respectively. By the end of the current observing season (2008B), this will have covered half of the entire halo of M31 in projection out to 150 Kpc, plus an extension around M33. This is a continuation of a successful M31 survey project (e.g., Ibata et al. 2007) and by end of 2010 will have finished surveying the entire M31 halo out to roughly 150 Kpc in projection, some 300 square degrees of sky.

This effectively opens up access to all planned targets to the full survey depth without the need for commissioning special photometric surveys. In addition, for the Galactic work, the full optical--NIR range enables exquisite control over target selection, allowing a focused approach in the more crowded regions of the Galactic Plane and Bulge.

6.7 Sky Subtraction

Sky subtraction by 'nod and shuffle', as proposed in the Feasibility Study, is hardly an efficient use of a 8 m class telescope since it requires four times longer integration to achieve the same rms signal/noise (half the time on target, twice as much sky variance). Alternative strategies of nodding to target on a different fiber halve this loss but at the expense of dedicating half of the fibers to sky measurements.

Can more sophisticated sky subtraction strategies coupled with a more stable fiber-fed spectrograph design eliminate the need for nod and shuffle? For a stable fiber-fed spectrograph there are very promising alternative strategies (e.g., Tolstoy et al. 2004 with FLAMES data; and Wild and Hewitt 2004 on SDSS data). We have investigated these, extending the above model fitting and PCA decomposition approaches by making use of Genetic Algorithms and Artificial Neural Networks. Recovering up to a factor four in telescope time for a given survey is a sufficient motive!

Here we summarize the results of our simulations, first for stellar spectra and then for galaxy spectra.

FLAMES data, available at comparable LR and HR resolutions provides a good benchmark for our tests. An example of a LR spectrum in the CaT region produced by the GIRBLDRS FLAMES pipeline is shown in Figure 6-6. The numerous skylines visible in this part of the spectrum not only serve as an

independent check on the overall wavelength calibration, but also enable an update of the wavelength calibration of the individual spectra. Modeling the sky spectrum using dedicated sky fibers works well providing the requisite processing steps are included (e.g., Bataglia et al. 2007) and we show an example of such automated sky subtraction and the necessary steps to implement it for processing FLAMES spectra are described below.

The first step is to combine all the sky spectra (typically, 10–20 sky fibers were allocated) using k-sigma clipping to remove spurious features. The average sky spectrum is then split into continuum and sky-line components using an iterative k-sigma clipped non-linear filter (a combination of median and boxcar). The average “sky-line” spectrum is used to define a sky-line template mask, essentially to isolate those regions of the sky spectrum with significant features and mask out the remainder.

Processing of individual object spectra then proceeds as follows:

- Each spectrum is filtered as before to split the spectra into a line and continuum component, but this time additionally masking out those regions affected by sky lines to help in defining the continuum;
- The object line spectrum, which includes sky lines, is then cross-correlated with the masked line component of the average sky spectrum, to provide an accurate differential wavelength update and(re)interpolated to be on the same wavelength system as the average sky spectrum;
- Sky subtraction then involves finding the optimum scale factor and profile matching kernel that produces a minimum L1 norm (average absolute deviation) when comparing the masked sky-line and object-line spectra, and applying it to the line-only spectra;
- Finally, the object continuum is added back to the wavelength-updated object-line spectrum, the sky continuum is removed using the sky-line scaling factor and the sky-subtracted spectrum is saved for the next stage in the processing.

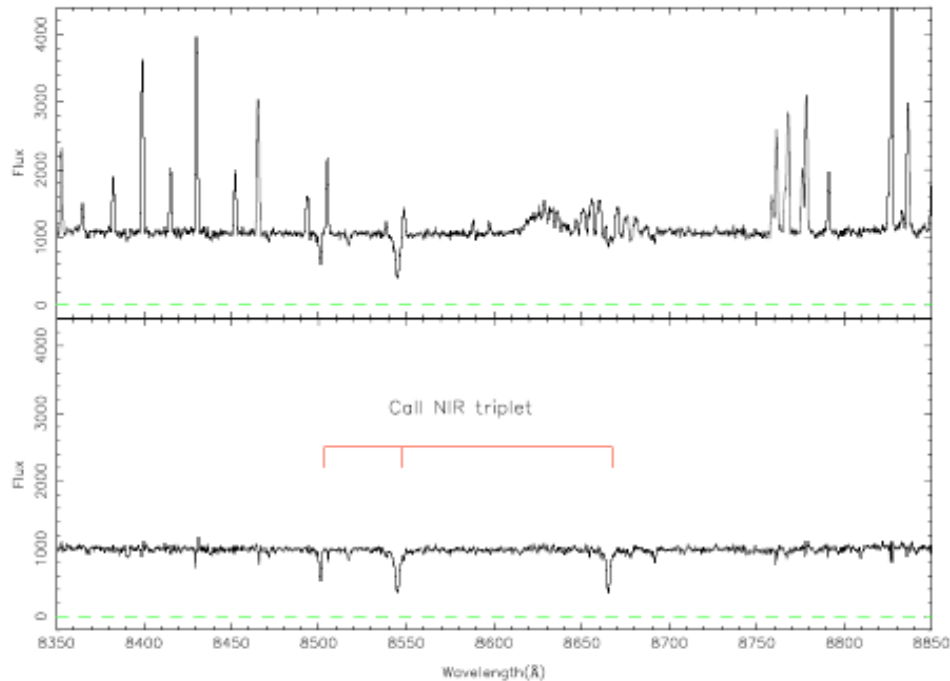


Figure 6-6: Example of automated LR sky subtraction from FLAMES benchmark test data.

The sky subtraction process described above involves three key components all of which are crucial to achieve good results. Accurate wavelength registration is absolutely vital for good sky subtraction and is (ironically) facilitated by the presence of copious numbers of strong sky lines. These sky lines are unresolved at this resolution and at the signal-to-noise achieved (see later) readily enables sub-km/s precision in wavelength alignment. This also has the added advantage of ensuring that systematic offsets due to wavelength calibration for later derived velocities are negligible. As a final step in this process, all the average sky spectra from each FLAMES observation are cross-correlated with a chosen reference sky spectrum and used to put all the observations on the same internal system.

The effects of combining the sky spectra to form an average sky and re-interpolating the object spectrum to this average wavelength system, almost invariably results in a slight mis-match between the spectral line profiles of the object and average sky spectra. This is circumvented by applying a Hanning smoothing kernel to each in turn and finding which combination of smoothed and unsmoothed gives the best results (as determined by the optimum scale factor). More sophisticated adaptive kernel matching (e.g., Alard & Lupton 2000) is probably unwarranted in this case.

The optimum-scaling factor, which in this case is chosen to minimize the L1 norm rather than the commoner L2 norm to reduce sensitivity to non-Gaussian outliers, is derived using a simple grid search with progressively finer step size. As noted previously, a mask is used to isolate the relevant regions of the sky spectrum to match. By first removing the continua from both sky and object, more emphasis is placed on minimizing the impact of sky lines residuals. Of course, implicit in the sky correction is the reasonable assumption that the derived scale factor for both sky lines and sky continuum is the same.

In a similar fashion for galaxy spectra, a PCA is performed in the observed-frame sky spectrum, taking advantage of the correlations between the sky subtraction residuals present in each spectrum. A test of the method on SDSS data shows very good removal of the OH emission features (see Figure 6-7). Some of our Team members are part of the GAMA survey (essentially 2dFGRS repeated 2 magnitudes fainter); the PCA method has been applied to sky-dominated fiber spectra in this survey, and gives very clean results.

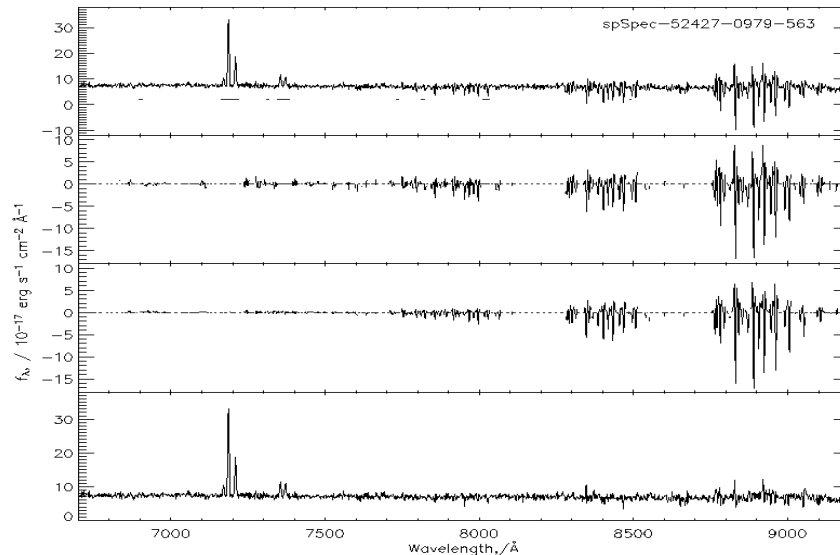


Figure 6-7: An illustration of sky subtraction on a SDSS galaxy spectrum. The top panel is the observed spectrum from the SDSS archive, while the bottom panel is the ‘clean’ spectrum after sky subtraction with the PCA method. The second and third plots from the top show the ‘sky’ pixels and the reconstructed sky spectrum, respectively (from Wild & Hewett 2005).

6.8 Fiber Allocation Efficiency

An important aspect of any fiber positioner scheme is the efficiency in which the individual positioner elements can direct or allocate fibers to the targets of interest for spectroscopy. The positioner allocation efficiency is defined as the fraction of positioner elements that can be successfully placed on a target of interest for a given target density and configuration.

The positioner comprises a large number of elements, each of which has a defined patrol region. If the number of targets is very large compared to the number of positioner elements, then every element will have many targets available to choose from and the positioner allocation success rate will be high. If there are few targets, then most positioner elements will not have a target available, but most targets will be successfully allocated. In this limit, the degree of overlap between adjacent patrol regions is less important. It is important, however, that there are not significant gaps between patrol regions, so that the few targets that do exist will not be missed. At intermediate target density, the positioner allocation

efficiency will be in between these two extremes, and will depend on the degree of overlap of adjacent patrol regions.

We have performed Monte Carlo simulations of the allocation process with both fields of randomly distributed targets, and also a clustered set: a sharp redshift selection of $0.7 < z < 1.3$ is used, where the sky distribution is generated using a semianalytic calculation in which the luminosity function is adjusted to match reality. The coupling between apparent magnitude and clustering should thus be as realistic as is possible with current knowledge. With such simulations, a variety of numbers of positioners, patrol diameters, and target densities were considered. The following points emerge from our studies:

(1) The fraction of unallocated fibers (i.e., waste) is a function of patrol diameter

(2) It is difficult to achieve high completeness ($> 80\%$) on a real sample with a single observation. Multiple observations of the same field increase completeness at the expense of lower efficiency, as more fibers are unallocated to targets in the later observations. The most efficient strategy will always be to accept some incompleteness and some fraction of fibers as unallocated using a single observation per field, unless there is a strong science requirement for full completeness in a given field.

(3) Magnitude dependent reallocation (i.e., bright objects need shorter exposures than faint ones) seems unlikely to offer a major improvement in observing efficiency given the survey cases described in earlier sections. A possible exception could be surveys in which the expected exposures are very long (so that overheads associated with reallocation do not dominate) and without steep number counts, so that there is sufficient diversity in required exposure times for the ensemble of objects.

(4) Clustering of sources will, of course, have an impact on allocation efficiency. If the probability of having more than one source in one patrol region and zero sources in a neighboring patrol region go up, then the allocation efficiency will go down. We have investigated this effect for the distribution of galaxies for our $z=1$ BAO survey, and have concluded that this is not a large effect.

(5) The allocation of fibers from the focal plane to the spectrographs has a significant effect on observing efficiency. If the number of available simultaneous spectra is smaller than the number of fiber positioners (as it is for the high resolution spectrograph described in the WF MOS Feasibility Study), then the efficiency can easily become dominated by the spectrograph capability rather than the fiber positioner properties.

The result of positioner allocation efficiency simulations for surveys in low-resolution spectrograph mode is shown in Figure 6-8.

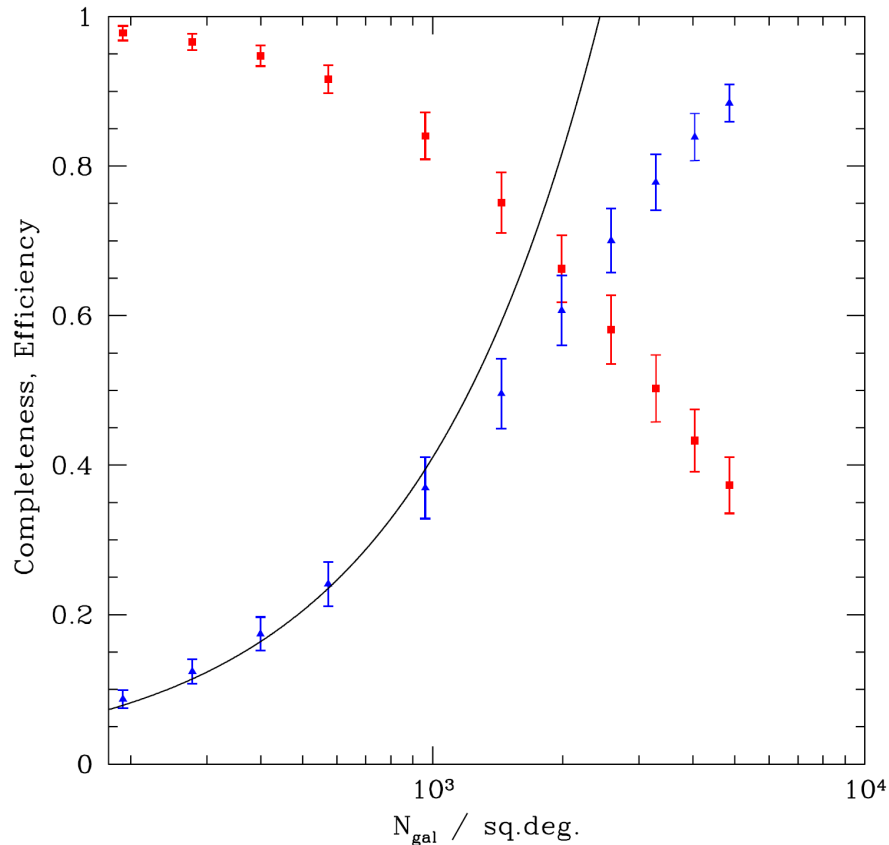


Figure 6-8: Efficiency and completeness as a function of target density. Blue points represent the allocation efficiency (the estimated fraction of positioner units that can be successfully assigned to a target) as a function of target density. Error bars are due to the size of sample variance on the scale of one target field. The black line is the ideal allocation efficiency as might be achieved by a plug-plate system. In red is the estimated completeness (i.e., the fraction of targets successfully assigned to a positioner) as a function of target density, assuming one observation per field.

For high spectral resolution, the spectrographs can support up to 600 simultaneous spectra. A flexible subset of the 2400 positioners is used for target acquisition, while the remaining are steered underneath Blocking Spots to reduce unwanted sky background. We have simulated the allocation efficiency for this scheme; the result is shown in Figure 6-9. This approach leads to significantly higher allocation efficiency than could be achieved by only using a fixed subset of the 2400 positioners.

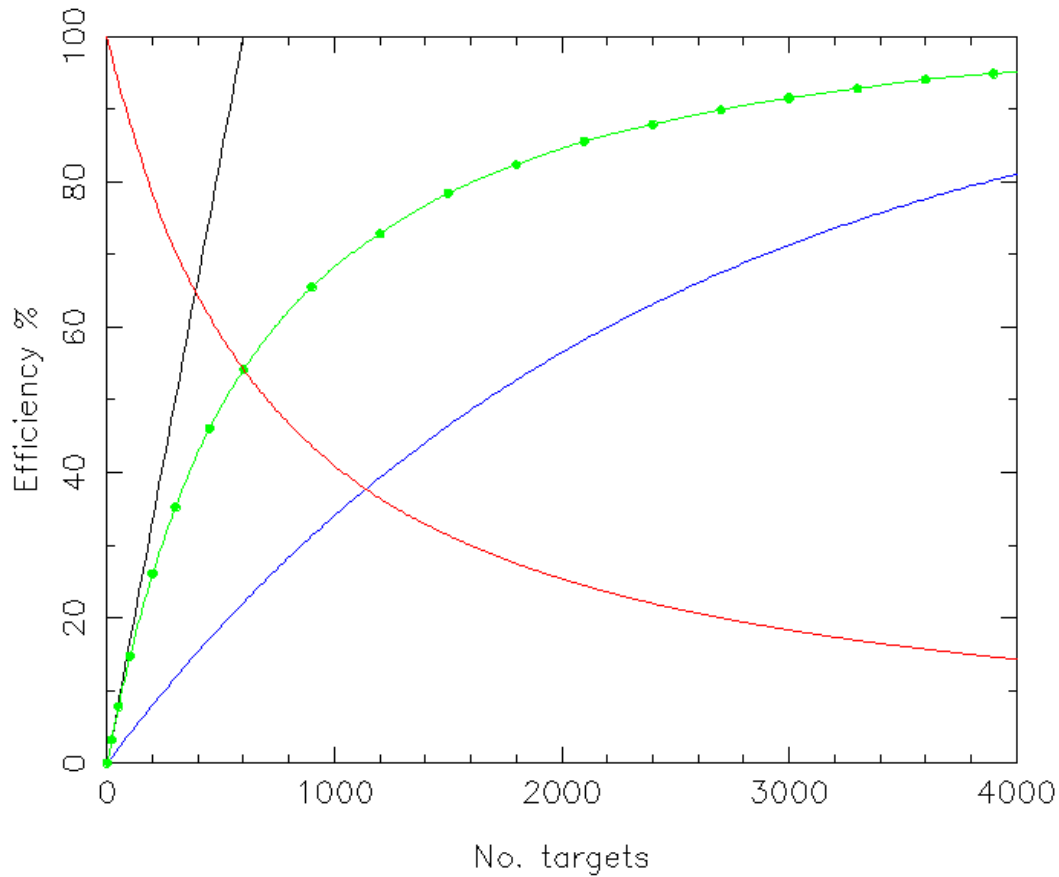


Figure 6-9: Positioner allocation efficiency for the high-resolution spectrograph mode versus number of targets in the field. Shown are the efficiencies for ideal allocation (black), such as one might expect from a plug-plate allocation scheme, and the WFMOS high resolution spectrograph mode (green). The WFMOS efficiency is superior to that achieved by a system that selects a fixed subset of fibers to route to the high resolution spectrograph (in blue), as assumed in the FS. Shown in red is the fraction of astronomical targets successfully assigned to a fiber.

As noted earlier, and is evident in the above Figures, the allocation efficiency depends on the surface density of available targets. For stellar surveys, Table 6-2 below shows the relevant densities as a function of magnitude and galactic latitude.

Table 6-2. Estimated V-band stellar density (per square degree) as a function of galactic latitude and magnitude limit.

$ b =$	20°	30°	60°	90°
V = 17	2290	1318	468	355
18	4074	2239	741	550
19	7079	3631	1122	832
20	11482	5623	1698	1230
21	17378	8128	2455	1778
22	23988	11220	3467	2399

6.9 Fiber Diameter

In order to assess the issue of the optimum fiber diameter, we conducted simulations based on actual Subaru SuprimeCam imaging data taken in 0.72 arcsec seeing - close to the median value for the observatory. We examined the fraction of total flux captured by the fiber as a function of fiber diameter, assuming negligible astrometric error.

In typical conditions, 20% of the PSF flux remains outside the fiber, even for a 2.0 arcsec diameter. Coupling this analysis with the sky background leads to a signal/noise versus diameter shown in Figure 6-10, which concludes a diameter of 1.2 arcsec is optimal – somewhat larger than in the FS.

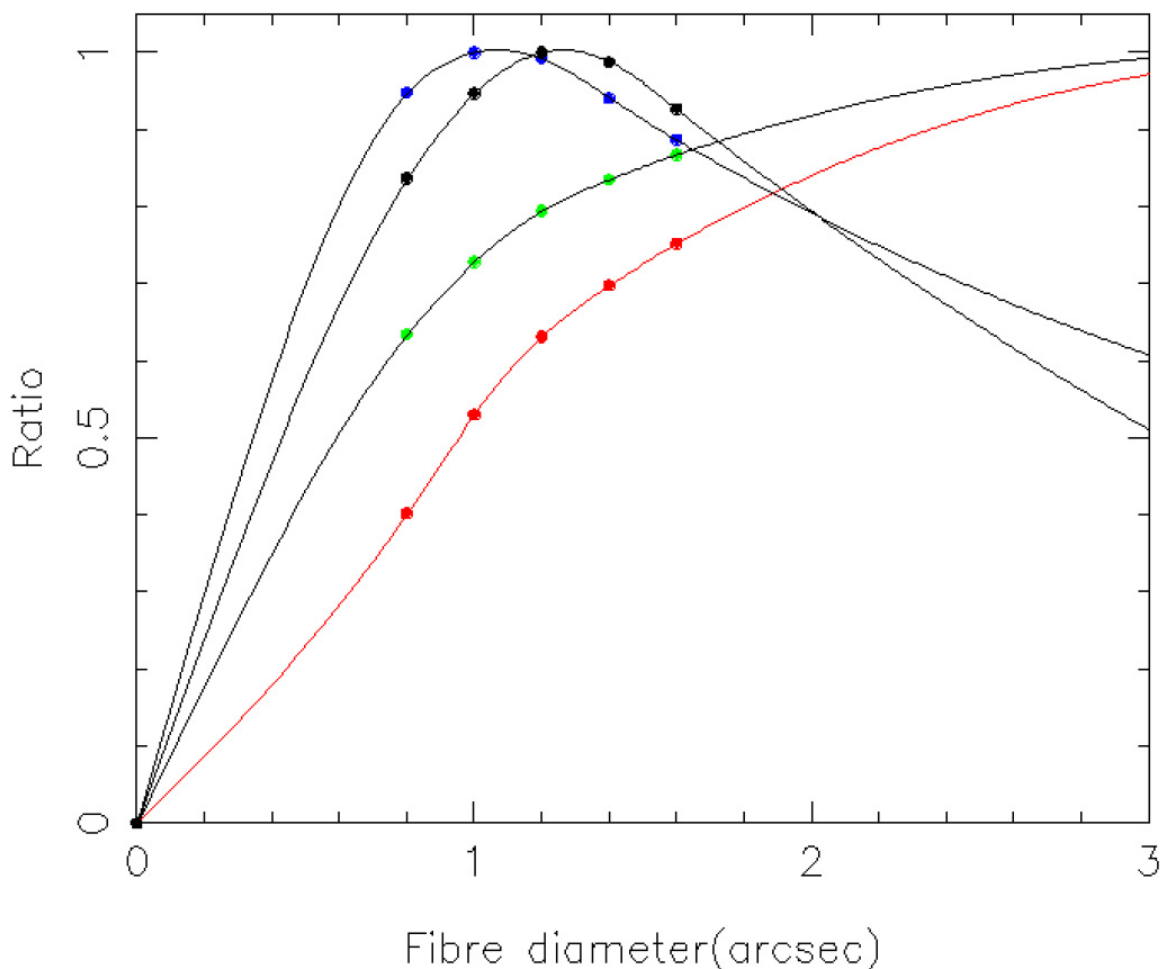


Figure 6-10: Signal to noise ratio (S/N) relative to peak S/N as function of fiber angular diameter, as measured in 0.72 arc sec seeing (i.e., close to the expected median seeing) with existing Subaru imaging data. Red points show curve-of-growth of flux for stellar objects. Green data points are S/N vs fiber diameter for bright stellar objects (i.e., negligible sky background), while black data points are for objects with similar mag to sky brightness per sq arcsec. Blue points show S/N for objects 3–4 mags fainter than sky.

6.10 Estimated Survey Time

6.10.1 Dark Energy

For the low-redshift dark energy survey (DELZ), we will rely primarily on emission line galaxies, using [OII] to identify the redshift. The allocation efficiency of the positioner system depends on the number of targets in the field, as shown in Figure 6-8. The desired surface density of galaxies is 1245 gal/deg², as described in Section 3. For a single observation of a field at this density, the average completeness is 67%, with some variation from field to field. We adopt a strategy of re-observing 20% of the fields, selecting the ones with the worst completeness. In the re-observed fields, a different set of targets is observed. This boosts the average completeness of the survey, as shown in Figure 6-11. It also has the benefit of allowing the repeated fields to be used as a systematic check on the results of the survey.

To reach our goal of measuring 4 million galaxies, assuming an 80% successful redshift fraction, we find we need 2380 fields to be measured once and 473 fields to be measured twice. The details appear in Table 6-3. From similar considerations, we find that we need a catalog from which to select objects to target that has a surface density on the sky of 2132/deg² (Table 6-4). Using DEEP2 number counts, we find the required limiting magnitude is $R_{AB} < 23.0$. The total survey time is summarized in Table 6-5.

Table 6-3: Number of fields required for low redshift dark energy survey. We adopt a two-tier strategy where most (80%) of fields are observed once. The 20% of fields with the worst completeness are re-observed, yielding higher average completeness with minimal additional survey time.

Low Redshift Dark Energy (DELZ) Survey - Field Strategy					
No. galaxies	Number of positioners	Redshift Success Rate	Number of times field is observed	Average completeness per field	Number of fields
$0.8 \times 4 \times 10^6$	2400	0.8	1	0.70	2380
$0.2 \times 4 \times 10^6$	2400	0.8	2	0.88	473

Table 6-4: Required density of galaxies for the low redshift dark energy survey. The required surface density of successful redshifts is 1245/deg². To achieve this density, we must start with a catalog of galaxies that reaches $R_{AB} = 23.0$.

Low Redshift Dark Energy (DELZ) Survey Galaxy Density			
Required Surface Density (/deg ²)	Redshift Success Rate	Average survey completeness	Required Catalog Density (/deg ²)
1245	0.8	0.73	2132

Table 6-5: Survey time requirements for the dark energy surveys.

Summary of Dark Energy Survey Times					
Survey	Exposure Time incl. overheads (hrs)	No. Fields w/ 1 obs.	No. Fields w/ 2 obs.	Total Obs.	Survey Time (hrs/nights)
Low Redshift (DELZ)	0.25	2380	473	3326	832 / 83.2
High Redshift (DEHZ)	4	69	-	69	286 / 28.6

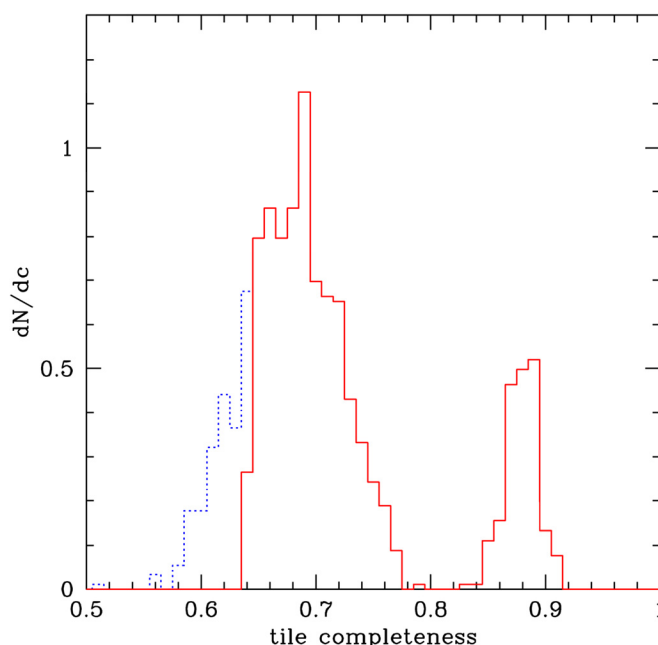


Figure 6-11: The red curve shows a histogram of the completeness of our survey fields. We have assumed that 80% of the fields are observed once (which gives the leftmost bump in the red curve), and 20% of the fields with poor initial completeness are reobserved, yielding higher completeness (rightmost bump in red curve). Shown in blue is the tail of the distribution that would have remained if these 20% were not re-observed.

The high redshift survey target allocation efficiency will be similar to the low-redshift survey. Angular clustering will be less, however, and we therefore dispense with the two-tier observation strategy, and instead rely on a single observation per field at an average completeness of 67%. The result is that 69 fields must be observed to reach 10^5 galaxies for the high-redshift survey, as summarized in Table 6-6.

Table 6-6: Number of required fields for the high redshift dark energy survey.

High Redshift Dark Energy (DEHZ) Survey - Field Strategy					
No. galaxies	Number of positioners	Redshift Success Rate	Number of times field is observed	Average completeness per field	Number of fields
10^5	2400	0.9	1	0.67	69

Section 6.4 describes simulated galaxy spectra. These simulations indicate that a continuum s/n ratio of 4 is sufficient for secure redshift identification using absorption line features. The corresponding

exposure time of 4 hours results in a total survey time for the high redshift dark energy survey of 286 hours.

6.10.2 Galactic Archaeology

From the estimated WF MOS system throughput, we can estimate the time required for the GA surveys. Exposure times estimates were validated through comparison to FLAMES. Included in these estimates is a measure of the fiber allocation efficiency. The allocation efficiency for the Low Resolution Galactic Archaeology Survey (GALR) follows the same function as the two dark energy survey modes. For the High Resolution Galactic Archaeology Survey (GAHR) mode, however, the allocation efficiency differs. The spectrograph is capable of producing up to 600 simultaneous spectra in this mode; this capability needs to be efficiently assigned to targets. The result is depicted in Figure 6-9.

The GA survey design is described in section 4, and requires observing 1530 fields for the Low Resolution Survey, and 1125 fields for the High Resolution Survey. We have also described a potential future survey (beyond the baseline GA survey) of 230 fields in M31 & M33. The total time required for these surveys is summarized in Table 6-7.

Table 6-7: Galactic Archaeology survey time requirements.

Galactic Archaeology Survey Time Requirements			
Survey	Exposure Time (hrs)	No. Fields	Survey Time (hrs/nights)
Low Resolution	0.5	1530	765 / 76.5
High Resolution	1	1125	1125 / 112.5
M31/M33 (stage 1)	6	100	600 / 60
M31/M33 (stage 2)	6	130	1300 / 130

7 SCIENCE REQUIREMENTS SUMMARY

Listing specific science objectives and requirements is useful and necessary for deriving instrument requirements and in understanding the flow of requirements from science to detailed engineering. In this section, the science requirements discussed in previous sections are summarized in a formal list. The list does not contain the derived instrument requirements, such as detector wavelength range and spectrograph throughput; the lower level requirements are described in the Functional Performance Requirements Document. The required wavelength range and spectral resolution are not consolidated into one master science requirement – listing these as separate requirements for each survey has allowed us to develop an instrument concept with separate spectrograph modes for the four surveys. The resulting flexibility has resulted in an optimized instrument design.

Below we list three categories of science requirements: (1) science objectives, (2) top level science requirements, (3) derived observing requirements. The science objectives describe the science results that we seek, but, because they may involve some assumptions about the universe are not directly verifiable. The top level science requirements and observing requirements are intended to be directly verifiable items. The context and motivation for the science objectives and survey requirements are described in earlier sections. Each item is given a short description. The designator “L1.X” is used for each of these requirements to indicate that they are Level 1 Science requirements and to distinguish them from the Instrument and Subsystem Requirements at Level 2 and below. The lower level requirements are described in the Initial Functional Performance Requirements Document.

7.1 Dark Energy Science Objectives and Top Level Requirements

The dark energy requirements are:

- **L1.1: (Science Objective)** WF MOS should use the BAO method to measure the distance to a mean redshift 1.2 with an accuracy of 0.6%, thereby providing a constraint on w at the pivot redshift to 3%. The survey will cover a range of redshifts, from 0.7 to 1.6

Rationale: The survey redshift coverage and precision on w is complementary to other planned surveys. The context is described in sections 3.6.1 and 3.6.2.
- **L1.2: (Science Objective)** WF MOS should use the redshift space distortions technique to measure the growth factor, $f_g(z) \equiv d \ln \delta / d \ln a$, in 4 independent redshift bins between redshifts 1 and 3 to a precision of 0.02 near redshift 1 and a precision of 0.1 near redshift 3.

Rationale: The redshift distortion survey provides an important, complementary probe of dark energy by measuring the growth rate of density fluctuations. The survey redshift range and precision would provide a major advance over the current state of knowledge and over currently planned experiments. The context is described in Sections 3.6.2 and 3.6.3.
- **L1.3: (Goal)** WF MOS should be designed to accomplish objectives L1.1 and L1.2 in less than 2000 hours of observing time.

Rationale: As described in Sections 1 and 3, the Subaru telescope is the primary resource available to the Japanese scientific community and will be in demand for a variety of scientific projects. The goal survey time represents our view of an acceptable allocation. The current survey estimate (Section 6) for the required survey time is 1120 hours.

- **L1.4 (Requirement)** WF MOS shall conduct a Low Redshift Dark Energy spectroscopic galaxy survey with the characteristics described in following table:

Low Redshift Dark Energy Survey	
Redshift Range	$0.7 \leq z \leq 1.6$
Number of galaxies	> 4,000,000
Target density for successful redshifts	1245 / deg ²
Incorrect Redshift Fraction	< 1%
Redshift precision, accuracy	$\Delta z < 0.001$

Rationale: The above survey parameters are required to provide sufficient accuracy for the BAO technique, including sufficient cosmological volume, in order to support L1.1, and the redshift 1 portion of L1.2 The parameters are derived in section 3.6.2. The approximate target density for successful redshifts is discussed in both section 3.6 and section 6.

- **L1.5 (Requirement)** The Low Redshift Dark Energy Survey shall meet the following observing properties:

Low Redshift Dark Energy Survey – Derived Observing Requirements	
Spectral range	6300-9700 Å
Spectral Resolution	3500
Magnitude Limit	$R_{AB} < 23.0$
Line S/N ratio	>7

Rationale: These properties must be met in order to achieve the survey required by L1.4 and are directly derived from it, as described in section 3.6.2. The required spectral range allows the measurement of the [OII] 3727 Å spectral double over the required redshift range. The spectral resolution is required to be sufficient to resolve the doublet, providing a unique identifier. An absolute minimum of 1340 is required to resolve the doublet. Higher resolution (e.g., up to 5000) may reduce sky brightness contamination, but starts to incur a detector read noise penalty, producing less efficient observations. The current design is a resolution of 3500, which is a balance between these factors. The magnitude limit is chosen to provide a sufficient source density so that the successful target density requirement of L1.4 can be met.

- **L1.6 (Requirement)** WMOS shall conduct a High Redshift Dark Energy spectroscopic galaxy survey with the following characteristics:

High Redshift Dark Energy Survey	
Redshift Range	$2.5 \leq z \leq 3.3$
Number of galaxies	> 100,000
Target density for successful redshifts	1000 / deg ²
Incorrect Redshift Fraction	< 1%
Redshift precision, accuracy	$\Delta z < 0.001$

Rationale: The above survey supports L1.2, a redshift distortion measurement, and is described in section 3.6.3.

- **L1.7 (Requirement)** The High Redshift Dark Energy Survey must meet the following observing requirements.

High Redshift Dark Energy Survey – Derived Observing Requirement	
Spectral range	4200-6500 Å
Spectral Resolution	1500
Magnitude Limit	$R < 25$
Continuum S/N ratio	>4

Rationale: These requirements are derived from L1.6 and are described in section 3.6.3.

7.2 Galactic Archaeology Science Objectives and Top Level Requirements

There are five top level science objectives for the Galactic Archaeology Science Case:

- **L1.10 (Science Objective):** WMOS should measure the mass, extent, substructure, and other properties of the Milky Way dark matter halo through characterizing approximately 30% of substantial stellar streams in the halo.
- **L1.11 (Science Objective):** WMOS should perform kinematic measurements of dSph candidates to confirm their status and measure the masses, density profiles, and extent of dSphs.
- **L1.12 (Science Objective):** WMOS should measure the extent, (sub)structure, and kinematics of Milky Way stellar populations.
- **L1.13 (Science Objective):** WMOS should compare the overall history and properties of the Milky Way with M31 and M33.
- **L1.14 (Science Objective):** WMOS should explore the fossil record of chemical evolution of stellar populations in the Milky Way.

Rationale: The above goals are described in detail in Section 4.1.4.

- **L1.15 (Goal):** WF MOS should be designed to accomplish the GA science objectives in less than 2500 hours of observing time, with a nominal allocation of 2/3 time to the high resolution survey and 1/3 time to the low resolution survey.

Rationale: As described in Sections 1 and 4, the Subaru telescope is the primary resource available to the Japanese scientific community and will be in demand for a variety of scientific projects. The goal survey time represents our view of an acceptable allocation. The current estimate (Section 6) for the required survey time is 1890 hours.

- **L1.16 (Requirement):** WF MOS shall perform a low resolution galactic archaeology survey with the following characteristics:

Galactic Archaeology Low Resolution Survey	
Area	2000 deg ²
Number of stars	3 x 10 ⁶
Resolution	5000
Sensitivity Limit	V=20, S:N = 10-15 / Å
Wavelength coverage	8150 – 8850 Å 4800 – 5500 Å
Wavelength centering	0.1 Å
Continuum Estimation Accuracy	5%
Relative Flux Calibration Accuracy	5%

Rationale: The survey properties are derived from science objectives L1.10 – L1.13, and are described in detail in section 4.1.

- **L1.17 (Requirement):** WF MOS shall perform a high resolution galactic archaeology survey with the following characteristics:

Galactic Archaeology High Resolution Survey	
Area	2000 deg ²
Number of stars	1 x 10 ⁶
Resolution	20,000
Sensitivity Limit	V=17, S:N = 150 / Å
Contiguous wavelength coverage	4800 – 6800
Wavelength centering	0.1 Å
Continuum Estimation Accuracy	5%
Relative Flux Calibration Accuracy	5%

Rationale: The survey properties are derived from science objectives L1.14, and are described in detail in section 4.1. The continuum estimate required allows sufficient precision in measuring equivalent widths. Relative flux calibration allows comparison with external galaxies.

8 INSTRUMENT DESCRIPTION

8.1 System Description

WF MOS is a fiber fed spectrograph designed to be mounted at the prime focus of the Subaru telescope located on the summit of Mauna Kea, Hawaii. The instrument allows simultaneous low resolution spectral observations of up to 2400 astronomical targets. In high resolution mode, WF MOS can observe 600 simultaneous targets.

We repeat the summary description of the instrument here for reference. Greater detail on the instrument, interactions, and components appear in the WF MOS Study Summary and in the Detailed Design Document.

WF MOS comprises components mounted in several locations. System elements required to be at the prime focus of the telescope are housed within a **Prime Focus Unit (PFU)**. The three Spectrographs along with their Detectors and support systems will be located in a spectrograph room adjacent to the telescope, above the Naysmith focus.

WF MOS will use several Subaru provided elements that are being developed for the **HyperSuprimeCam (HSC)** instrument. These include the HSC **Field Rotator**, **Hexapod**, structure, and a **Wide Field Corrector (WFC)**.

The filter and dewar window used with HSC are replaced by the WF MOS **Field Element**, located close to the telescope prime focus. The Field Element is a flat window of 30 mm thickness and enables efficient coupling of the light from the WFC to the WF MOS fibers. It compensates for the removal of the Dewar window and filter that are part of the design for HSC. The Field Element also contains an array of small obscuring spots under which unused spectrograph fibers can be parked.

An array of 2400 optical fibers is located in the PFU, with each fiber tip position being controllable in-plane by a piezo-electric **Fiber Positioner**, nicknamed “Cobra.” Each fiber tip can be positioned within its 9.5 mm diameter circular patrol region. The patrol regions are in a hexagonal close-packed pattern, with 8 mm separation, and fill a hexagonally shaped 1.4 degree field of view. The overlap between adjacent patrol regions enables 100% sky coverage of this hexagonal field. The hexagonal shape of the field of view allows efficient tiling of the sky for large area surveys.

The fibers can be reconfigured for new observation fields in 40 seconds, with each fiber tip placed to an accuracy of 5 microns (corresponding to less than 0.054 arc seconds on the sky). Fibers tips are translated (rather than tilted) within the image plane, providing uniform coupling efficiency for all configurations.

The small fraction of fibers which are not allocated to astronomical targets will measure the spectrum of the sky. In the case of the GAHR survey, which is cross-dispersed, three out of every four fibers is

obscured by positioning the fiber tip behind a small dot on the back of the field element to avoid overlaying spectra or adding unnecessary sky background.

The **Fiber System** consists of 2400 fibers which relay light incident at the instrument's focal plane to three spectrographs located remotely in a room adjacent to the telescope. The fibers are 60 meters in length and are divided into three groups providing 800 inputs to each spectrograph. A key component of the fiber system is a **Fiber Connector** which allows most of the fiber bundle to be permanently installed to the telescope while facilitating the removal of the PFU as necessary. The connector is located five meters from the positioner end, allowing removal of the Top End Unit while leaving 55 m of the fiber bundle on the telescope structure.

After the science fibers enter the spectrograph room, they are divided three ways and arranged as linear arrays of 800 fibers at the input to each of three identical **Spectrographs**. The Spectrographs provide the capability to simultaneously measure 2400 spectra in low-resolution mode and 600 spectra in high-resolution mode. During high-resolution spectral observations, the unused fibers are positioned underneath **Blocking Spots** to reduce the sky background contribution to the spectra in the high-resolution mode. Each Spectrograph uses a Schmidt optics system composed of a collimator, grating, and camera optics which are reconfigurable to support the four primary science surveys, which require different spectral resolutions and spectral ranges.

At the image plane of each spectrograph is a **Detector System** consisting of a pair of close butted 2880×5760 pixel CCDs inside a dewar and associated cooling system. The 800 spectra are dispersed along the columns (5760 pixels), so the gap falls between spectra. In the case of the GAHR survey, the 200 cross dispersed spectra fill the detector array. The CCDs have exceptionally high quantum efficiency, which improves overall instrument efficiency.

The **Acquisition and Guide System** is composed of four cameras located on the instrument optics bench in the PFU. Once calibrated to the fiber optic focal plane the Acquisition and Guide System will provide feedback to update the telescope's pointing and field rotation by tracking on guide stars within the cameras' field of view.

There are four **Metrology** cameras, mounted on the prime focus support struts looking down at back-illuminated fiber tips via the primary mirror of Subaru. The metrology cameras determine the location of the fiber tips, allowing accurate positioning of the fibers on the selected science targets. Each metrology camera consists of imaging optics with a CCD detector and includes an internal flat field source. Calibration of geometrical distortion inherent in the optics of the metrology cameras is achieved by having 154 illuminated fixed **Fiducial Fibers** whose positions are known accurately. Ninety one of the fixed fiducials are within the bounds of the hexagonal field of view, while 48 fixed fiducial fibers are at the perimeter of the hexagonal field. Beyond the perimeter of the hexagonal field, fifteen are used to

provide encoding of the rotator angle. The fiducial fibers also allow correction for geometric distortion in the WFC, through measurement and modeling.

The field of view of each Metrology camera is designed to image 1/4 of the optics bench fibers. The cameras image the backlit science fibers by viewing the optics bench through the telescope optical system including the WFC and the primary mirror. The centroid of each fiber image is calculated and used to determine each science fiber position with respect to the fixed fiber locations. This coordinate system is accurately referenced to the A&G camera allowing accurate placement of astronomical targets on the science fibers.

The science fibers are back-illuminated by sources located inside the three spectrographs. Only one set of 800 fibers is illuminated at a time, in a manner allowing no ambiguity in determining fiber positions in the case that two fibers occupy a region of overlapping patrol regions.

The **Prime Focus Unit** (PFU) will house the WF MOS Optical Bench which contains the Field Element, Fiber Positioner System, Acquisition and Guide System, and components of the Fiber System. Additional components of the Fiber System, Power Distribution System and Thermal System are contained in the top end of the PFU. The PFU can be installed and removed from the telescope as a single unit. The optical bench is mounted to the Rotator within the PFU via a bi-conic structure. This structure is tuned in stiffness to compensate for differential flexure between the WFC and the Rotator interface where the WF MOS components are mounted.

The **Power Distribution System** is located within the PFU to provide power conditioning and control to the electronics associated with the Fiber Positioner System, the Acquisition and Guide System, and the Metrology System. The distribution system interfaces to the telescope facility power and receives power control inputs from the System Control function. The **Thermal System** provides the interface between the telescope facility cooling system and the instrument systems located in the PFU to prevent excess heat from disturbing the telescope's viewing environment.

The **Spectral Calibration Lamps** provide the capability to measure the spectral response of the WF MOS instrument by providing a spectral source at the input to the telescope. The calibration lamps will be mounted on the telescope apart from the Prime Focus Unit.

The **System Control** provides the capability to manage an observation's preparation and execution. Preparation tasks include parsing large surveys into a series of individual observations, matching fibers to designated targets and selecting appropriate guide stars, predicting exposure times, and describing observations in a Subaru-format file. During telescope observations the System Control orchestrates the instrument systems to achieve successful data collection, sequences the Metrology and Fiber Positioner Systems to achieve target acquisition with the fibers, interfaces to the Subaru Observatory Software System, and provides operator interfaces for quick-look data and instrument health and safety displays.

The System Control also provides the capability to perform high level engineering tests to aid in instrument integration and troubleshooting.

The **Data Reduction** function receives raw data read from the Detector System and uses it to produce calibrated spectra ready for scientific analysis. The Data Reduction function provides the capability to reduce data of varying spectral resolution and saves all spectroscopic and image files in the required data format. The Data Reduction function will also provide the capability to quickly assess the quality (completeness, signal-to noise ratio, etc.) of the data collected.

A typical observation proceeds as follows. After initialization, instructions are executed to configure the telescope and instrument for the desired observation. The details of each observation are pre-planned using software provided by the System Control to aid the researcher in orchestrating the survey. Using information derived from a catalogue of astronomical objects, the field configuration including the positions for each of the 2400 fibers is computed prior to the start of the observation. The spectrograph configuration is determined by which of the 4 primary science surveys is being executed. A typical observing night might use more than one spectrograph configuration in order to optimize survey efficiency as sky brightness or the seeing changes.

Execution of an observation begins with moving the telescope to the desired field center. While the telescope is slewing, the Fiber Positioning System executes commands from the Control System to simultaneously move each of the 2400 fibers to their required positions. The Metrology System is used to verify each fiber's position. The positioning process proceeds as follows:

1. The current position of each science fiber is determined relative to a set of fixed fiducial fibers. These fixed fibers are back-lit by a dedicated calibration lamp. The back-lit fibers are imaged by the Metrology System and the centroid of each fiber is calculated. Similarly, the 2400 science fibers are back-lit by calibration lamps in each spectrograph and imaged by the Metrology System. The centroids of each science fiber image are computed in order to determine their relative positions.
2. The Control System computes and issues the necessary commands to the Fiber Positioning System to move the 2400 Science Fibers to the positions required for the observation. The metrology and the fiber movements are coordinated in 3 groups of 800 fibers. Some operations proceed in parallel.
3. Steps 1 and 2 will be repeated several times to accurately position each fiber.

The positioning process is estimated to take approximately 40 s from start of telescope pointing to completion of fiber positioning. In parallel with this process, the Acquisition and Guide System refines the pointing of the telescope. The Acquisition and Guide System provides feedback to the telescope pointing and rotator position during the observation. The hexapod is commanded to the appropriate position to maintain the WFC alignment in the presence of flexure in the PFU.

Once positioning is complete, the Detector System collects data. The Data Reduction System produces quick-look information on the completed observation so that survey progress can be monitored.

8.2 Instrument Operational Modes

The WF MOS instrument will support the following types of operational mode at the telescope:

- Start-up
- Target Acquisition
- Observation
- Calibration
- Testing

A typical observing night will consist of the use of several of these modes. We describe each of these modes below. The descriptions are necessarily preliminary; greater detail will be developed in the course of the progression of the instrument design and construction.

In addition, the health and status of the instrument will be monitored continuously, and is therefore not listed as a separate operational “mode.” The “monitor status” function is described in Section 9.

8.2.1 Start-up

The Start-up mode is used to initialize the WF MOS instrument at the beginning of an observing session. All subsystems are powered up, self-tested and made ready for observation. The observations to be made during the session are selected.

- Power systems on.
- Initialize subsystems.
- Perform power-up tests.
- Load the description of the observations to be made.

Start-up also includes a subset of commands used to configure the spectrograph (selected grating, filter wheel setting, camera angle, etc). These commands will generally be used once at the beginning of the observing night. The system allows the spectrograph to be reconfigured for a different spectral mode during the course of the observing night, as might be useful to optimize survey strategies with respect to weather, moonrise, or other constraints.

8.2.2 Target Acquisition

The Target Acquisition mode is used to acquire a new target field for observation. If the new target field is at a different location on the sky from the previous observation, the Subaru telescope is slewed to a new target field. At the same time the positioner subsystem is configured to place the science fibers at the expected positions of the science targets in the focal plane (the positions having been calculated in advance by the observation preparation system). The metrology camera is used to provide feedback on the

position of the fibers. When the telescope has reached the target field it begins tracking. The instrument rotator also begins tracking the field. The autoguider CCDs locate the guide stars (whose positions are known relative to the science targets) and start sending tracking corrections to the Subaru TCS. The system aligns the target field.

- Acquire target field with acquisition system.
- Enable ADC operation.
- Focus and identify stars on at least two of the autoguider detectors to determine telescope offset and rotational offset.
- Command telescope to initiate offset to bring stars to required position
- Lock in acquisition using the Acquisition and Guide System (A&G).
- Fine tune focus using the A&G system.
- Initiate guiding.

8.2.3 Observation

In Observation mode, the WF MOS instrument carries out the steps needed to make science observations. For efficiency, this mode may be overlapped with Target Acquisition (e.g., the instrument may be configured at the same time the telescope is slewing, and the telescope may be slewed to the next target as soon as the instrument and detector systems have finished acquiring data). The spectrographs are configured as required for the observations and the detectors are set to make one or more science exposures, as requested by the user. At the conclusion of each exposure, the data are read out and passed to the Data Pipeline for archival and online data reduction.

- Take required number of exposures.
- Fine tune fiber positions as required (For observations with a total time longer than approximately 60 minutes, fibers will need to be repositioned to account for the changes in the astrometric distortion due to atmospheric refraction. A detailed plan for this will be developed before the instrument Preliminary Design Review).
- Reassign fibers to new targets as required in-between exposures to optimize data collection, as determined by the observation planning software (using Target Acquisition mode). We do not envision reassigning subsets of fibers between telescope pointings for the four primary science surveys. The instrument system, however, does have this capability inherently, which may be useful for future additional surveys.
- Collect FITS header information and send data to online data reduction pipeline and Subaru data archive.
- Execute quick look data reduction at end of each exposure.

The following distinct types of science observation will be made:

- Low redshift dark energy survey (DELZ):

- All 2400 fibers are available to be allocated to science targets. Allocation efficiency of fibers will be less than 100%; unallocated fibers will be used for sky background subtraction.
- The spectrographs are configured into DELZ mode.
- The science data will consist of three images (one per spectrograph), each containing 800 spectra, for up to 800 distinct science targets.
- High redshift dark energy survey (DEHZ):
 - All 2400 fibers are available to be allocated to science targets.
 - The spectrographs are configured into DEHZ mode.
 - The science data will consist of three images (one per spectrograph), each containing 800 spectra, for 800 distinct science targets.
- Low resolution galactic archaeology survey (GALR):
 - All 2400 fibers are available to be allocated to science targets.
 - The spectrographs are configured into GALR mode.
 - The science data will consist of three images (one per spectrograph), each containing 800 spectra, for 800 distinct science targets.
- High resolution galactic archaeology survey (GAHR):
 - A specific subset of up to 600 fibers are allocated to science targets.
 - The spectrographs are configured into GAHR mode.
 - The science data will consist of three images (one per spectrograph), each containing up to cross-dispersed 200 spectra, corresponding to 200 distinct science targets. Each cross-dispersed spectrum will be recorded on the detector in 4 separate segments
- Miscellaneous observation LR and HR:
 - Miscellaneous observations can be made by mixing and matching features from the above four survey modes. In addition, the wavelength range and spectral resolution of the spectrographs can be tailored for a particular science project, and are not limited to the fixed ranges specified for the survey modes. It may be possible to operate each of the spectrographs simultaneously in a different mode.
 - Used for added value science and miscellaneous observations.
 - All 2400 science fibers may be allocated to science targets for low spectral resolution (LR) observations, or up to 600 science fibers may be allocated to science targets for high spectral resolution (HR) observations.
 - The spectrograph is configured to the desired spectral resolution and wavelength range by selecting the appropriate grating, filter and camera-collimator angle combination.
 - The science data will consist of three images (one per spectrograph), whose layout depends on the chosen spectral resolution.

The low spectral resolution modes (DELZ, DEHZ, GALR and Miscellaneous LR) will require a different data reduction procedure from the high spectral resolution modes (GAHR and Miscellaneous HR), which generate cross-dispersed spectra.

8.2.4 Calibration

The Calibration mode is used to calibrate the instrument so that the observed data can be converted into a form that has most instrumental signatures calibrated or removed. A variety of calibration frames are required including, but not necessarily limited to, the following: bias, dark, flat field, and wavelength.

It is a goal to have the spectrographs stable enough during the night and after fiber reconfiguration that daytime calibrations will be sufficient for the nightly observations. This will certainly be easy to achieve for the bias and darks, but may be risky for the flat fields and wavelength calibrations depending on the level of calibration required for the data. Further study will be required during the design phase.

- Obtain required set of biases in the daytime.
- Obtain required set of darks in the daytime.
- Obtain required set of flat fields for each fiber configuration using set of calibration lamps mounted on the spider vane. Goal is to be able to do this during the daytime, but may need to be done at the time of observation if the fiber performance is not stable against fiber reconfiguration.
- Obtain required set of wavelength calibration frames using set of calibration lamps mounted on the spider vane. Goal is to be able to do this during the daytime, but may need to be done at the time of observation if the spectrograph stability proves to be insufficient or if fiber configurations impact on the calibration stability.

8.2.5 Testing

This is a mode of operation in which all capabilities of the instrument can be tested for engineering purposes. This mode of operation can be performed when the instrument is either on or off of the telescope and is primarily used for maintenance, problem fixing, and diagnostics. Special fixtures may be required for off telescope testing, such as back illumination of the fibers on the positioner or calibration lamp illumination of the spectrographs. Many of the instrument components will have a mode which allows that component to be exercised, and faults reported. Examples include the fiber health system, the positioner configuration, and the detector readout. The full scope and capability of this mode will be developed before the Preliminary Design Review.

9 OPERATIONAL CONCEPT MODEL

9.1 Introduction

To provide insight into how the WF MOS instrument will be used to accomplish the desired science surveys, we provide the following description of system level interactions. The operational WF MOS system can be divided into four distinct packages:

- **WF MOS Observation Preparation**—this package includes all the facilities to prepare WF MOS observations for submission to the observatory. It allows proposals to be submitted, approved and then prepared for execution.
- **WF MOS Observation Execution**—this package includes all the facilities for making WF MOS observations at the observatory.
- **WF MOS Pipeline**—this package includes all the facilities for processing WF MOS data. It provides a quick look display to the observer and provides reduced data for the Gemini Science Archive.
- **WF MOS Engineering**—this package contains all the engineering operations that are needed to support WF MOS.

The operation of the system can be described by these set of “Use Cases.” The Use Case notation is defined in Figure 9-1. Detail on each of these is provided in the following sections.

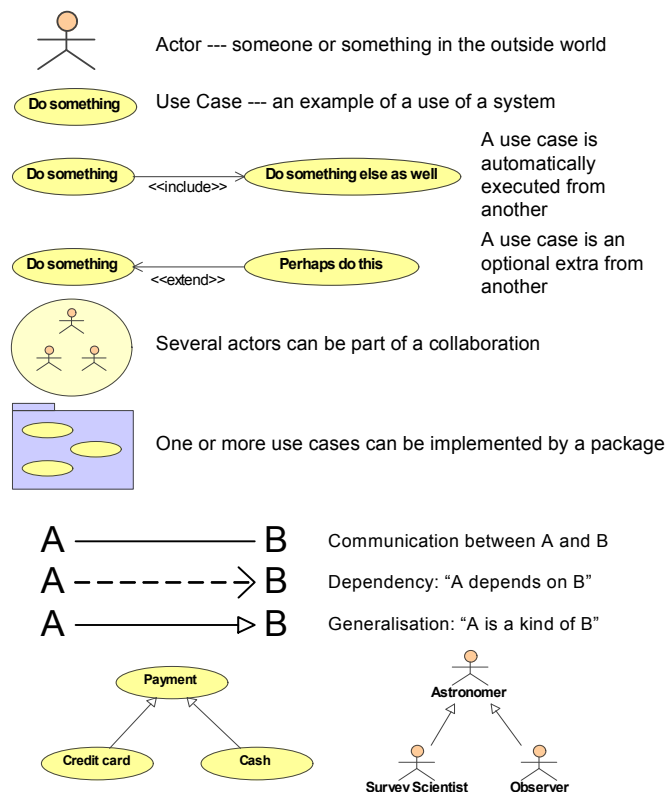


Figure 9-1: Use Case Diagrams Key

9.2 WF MOS Observation Preparation

Figure 9-2 shows a use case diagram for the WF MOS observation preparation package.

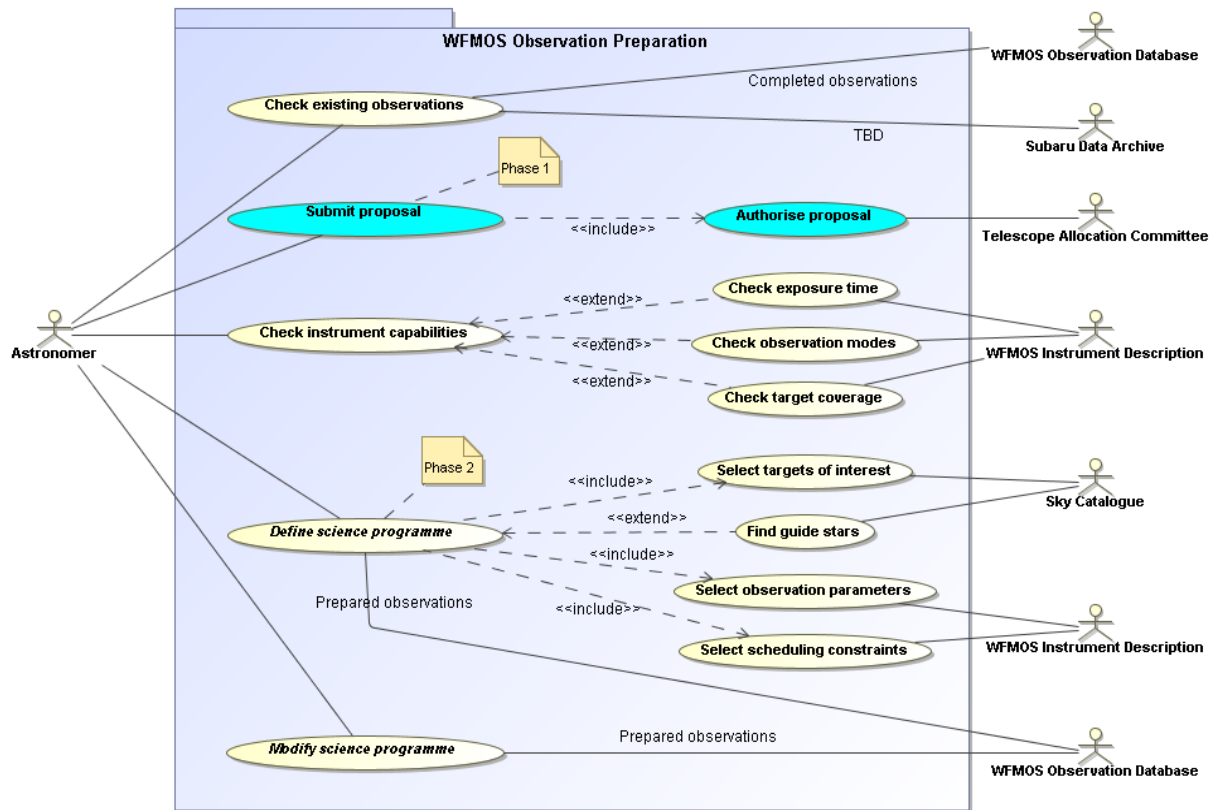


Figure 9-2: Use Cases for WF MOS Observation Preparation

The package needs to support the following operations:

Submit Proposal: An astronomer submits a proposal to make one or more observations with WF MOS, perhaps using the existing Gemini phase 1 submission tool. A proposal can be an idea for an entire survey, a proposal to make a specific observation, or a list of serendipitous targets that could be observed during a survey observation if there are any spare fibers.

Authorize Proposal: WF MOS observation proposals are authorized by a Telescope Allocation Committee and then move on to phase 2. The authorization procedure is decided by the Gemini and Subaru observatories.

Check existing observations: The status of existing observations in the science archive is checked and reported. There needs to be a facility for checking the current status of each survey, and for listing the fields already observed.

Define science program: This represents the preparation of a series of WF MOS observations designed to fulfil an astronomical project. The astronomer specifies the observation in terms of area of sky to be covered, type of objects to be observed and required magnitude range, and perhaps a list of wavelength ranges and grating resolutions required for each object. Suitable guide stars are chosen for each target field. The end product will be a series of individual observations that make up the survey, which are saved to the “Prepared Observations” part of the Observation Database. Observations made in adjacent fields can be mosaiced together, or observations in a crowded field may be divided into different fiber configurations at the same telescope pointing. The exact choice of survey field centers may be determined by the availability of suitable guide stars (e.g., at the Galactic poles).

We distinguish between five different types of survey preparations namely:

- Define Low Redshift Dark Energy survey
- Define High Redshift Dark Energy survey
- Define high resolution Galactic Archaeology survey
- Define low resolution Galactic Archaeology survey
- Define other surveys (TBD)

Modify science program: This facility allows a prepared science program to be modified. The observations may be adjusted to cope with a change to the instrument (such as broken fibers) or some new serendipitous observations can be piggy-backed onto an existing science program to make use of the non-allocated fibers.

It is assumed that the Subaru telescope allocation committee will decide which nights will be allocated to WF MOS observations.

9.3 WF MOS Observation Execution

Figure 9-4 shows a use case diagram for the WF MOS observation execution package.

Execute science observation and **Execute calibration observation** represent the kinds of observation that can be made, with the main difference being that **Execute calibration observation** could be executed during the day.

Acquire target includes all the procedures needed to set up the Subaru telescope, including the acquisition of guide stars and the configuration of the positioner.

Shutdown/End of session—All the procedures that need to take place at the end of any session, including parking the telescope, protecting the instrument and shutting everything down.

Monitor status—The health and status of the instrument will be monitored continuously. The operator will be provided with display screens to follow the progress of an observation and show instrument parameters, such as temperature and pressures. Any faults or alarms are reported to the operator. Any significant events that happen during the night are written to the Observation Log.

9.4 WFMOS Engineering

The WFMOS engineering use cases are summarized in Figure 9-5.

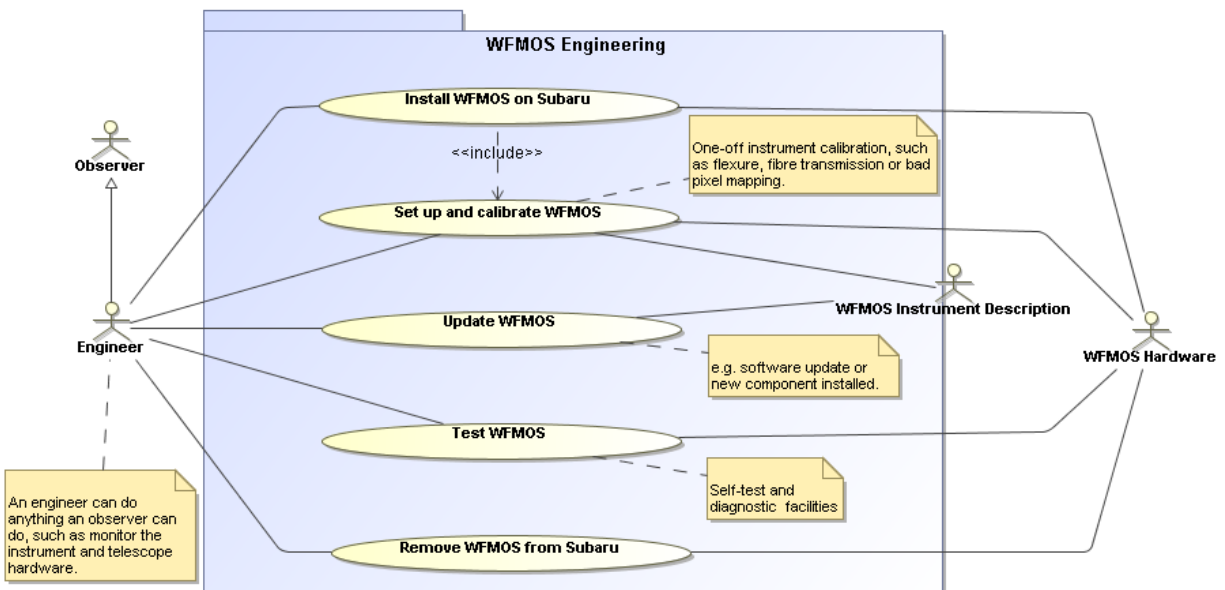


Figure 9-4: Use Cases for WFMOS Engineering

These facilities support engineering work and any other operations necessary to keep WFMOS operating to full performance:

Install WFMOS on Subaru: Each time the instrument is installed on the Subaru top-end, engineering facilities will be needed to check the instrument has been installed correctly, check the health of the instrument (e.g., fiber connectivity), update any calibration information that might have changed, and update the instrument configuration.

Remove WF MOS from Subaru: When the instrument is removed from the Subaru top-end, engineering facilities will be needed to update the instrument configuration.

Set up and calibrate WF MOS: WF MOS will need maintenance procedures to

- Make one-off calibration measurements, such as measuring the flexure and transmission of the fibers and mapping any bad pixels on the detectors.
- Make daytime calibration observations.
- Test and maintain a record of the health and performance of the instrument (see below).
- Support instrument updates (see below).

Update WF MOS: WF MOS will need engineering facilities to support any changes to the instrument system. A change could be a new release of the software, a recalibration of the instrument's configuration data (following the installation of a new piece of exchangeable hardware, such as a filter), or a quick repair made during the night to correct a problem.

Test WF MOS: WF MOS will need verify facilities to measure and record the performance of the instrument. Two such procedures ("POSITIONER metrology observation" and "FeRaS fiber health measurement") are already known about.

10 REFERENCES

- Abdalla F., Mateus A., Santos W., Sodre L.Jr., Ferreras I., Lahav O., 2008, MNRAS 387, 945
- Abdalla, F.B., et al. MNRAS, 387, 969 (2008)
- Albrecht A. et al., 2006, DETF Report, arxiv: astro-ph/0609591
- Albrecht A. et al., 2009, arxiv: 0901.0721
- Alcock C., Paczynski B., 1979, Nature 281, 358
- Allende Prieto, C. et al 2008, AJ, 136, 2070
- Allende Prieto, C., et al 2006, ApJ, 636, 804
- Ballinger W.E., Peacock J.A., Heavens A.F., 1996, MNRAS, 282, 877
- Banerji, M., Abdalla, F.B., Lahav, O., Lin, H., MNRAS, 386, 1219 (2008)
- Battaglia G., et al., 2005, MNRAS, 364 433
- Battaglia G., et al., 2008, MNRAS (in press)
- Bica E., 1988, A&A, 195, 76
- Binney J.J., Evans N.W., 2001, MNRAS, 327, L27
- Blake C., Glazebrook K., 2003, ApJ, 594, 669
- Bode P., Ostriker J.P., Turok N., 2001, ApJ, 556, 93
- Chevallier M., Polarski D., 2001, Int. J. Mod. Phys. D10, 213 [gr-qc/0009008]
- Christlieb N., 2003, Reviews of Modern Astronomy, 16, 191
- Coil A. et al., 2004, ApJ, 617, 765
- Coil A.L. et al., 2004, ApJ, 609, 525
- Collister, A. & Lahav, O., PASP, 116, 345 (2004)
- Cook, D., et al 2007, BAASS, 38, 896
- DeDeo S., Caldwell R.R., Steinhardt P.J., 2003, Phys. Rev. D 67, 103509
- Dvali G., Gabadadze G., Porrati M., 2000, Phys. Lett., B485, 208
- Efstathiou, G. Sutherland W. & Maddox S.J., 1990, Nature, 348, 705
- Eisenstein D.J. et al., 2005, ApJ, 633, 560
- Eisenstein D.J., Seo H.-J., Sirko E., Spergel, D.N., 2007, ApJ, 664, 675
- Eisenstein D.J., Seo H.-J., White M., 2007, ApJ, 664, 660
- Elgarøy O., Lahav O., 2005, New J. Phys., 7, 61 (hep-ph/0412075)
- Fairbairn M., Goobar A., 2006, Phys. Lett. B, 642, 432
- Feldman H.A., Kaiser N., Peacock J.A., 1994, ApJ, 426, 23
- Fellhauer M., et al., 2006, MNRAS, submitted
- Fux R., 1997, A&A, 327, 983
- Glazebrook K., Blake C., 2005, ApJ, 631, 1

- Gustafsson, B., et al. 2008, astro-ph 0805.0554
- Guzzo L. et al., 2008, Nature, 451, 541
- Hawkins E. et al. (the 2dFGRS Team), 2003, MNRAS 346, 78
- Heavens A.F., 2003, MNRAS, 343, 1327
- Hildebrandt H. et al. 2005, A&A, 441, 905
- Host O. et al., 2007, Phys.Rev.D 76, 113005
- Howard, C. D. et al 2008, ApJ, 688, 1060
- Hu W., Jain B., 2004, Phys. Rev. D, 70, 043009
- Hu W., Sawicki I., 2007, arXiv:0708.1190
- Hu W., Sawicki I., 2007, Phys. Rev. D 76, 104043 [arXiv:0708.1190]
- Huterer D., Takada M., Bernstein G., Jain B., 2006, MNRAS, 366, 101
- Jain B., Connolly A., Takada M., 2007, JCAP, 03, 013
- Kaiser N., 1986, MNRAS, 219, 785
- Kaiser N., 1987, MNRAS, 227, 1
- Kiakotou A., Elgarøy O., Lahav O., 2008, Phys. Rev. D 77, 063005
- Kirby E., et al. 2008, astro-ph 0804.3590
- Kirby, E. N., Guhathakurta, P. & Sneden, C. 2008 ApJ, 682, 1217
- Kleyna et al. 2001, ApJ, 564, L115
- Kleyna J.T., et al., 2005, ApJ, 630, L141
- Kolb E.W. et al., 2006, DETF Report
- Komatsu E. et al., 2008, arxiv:0803.0547
- Lee, Y.S. et al 2008b, AJ, 136, 2050
- Lee, Y.S., et al 2008a AJ, 136, 2022
- Lesgourgues J., Pastor S., 2006, Physics Reports 429, 307
- Linder E.V., 2003, Phys. Rev. Lett. 90 , 091301
- Linder E.V., 2005, Phys. Rev. D, 72, 043529
- Ma Z., Hu W., Huterer D., 2006, ApJ, 636, 21
- Madgwick D.S. et al. (the 2dFGRS Team), 2003, MNRAS 344, 847
- Majewski S. R., et al., 2005, AJ, 130, 2677
- Mateo et al., 1998, AJ, 116, 2315
- Matsubara T., 2004, ApJ, 615, 573
- Matsubara T., Suto Y., 1996, ApJ, 470, L1
- Mcdonald P., Seljak U., 2008, arXiv: 0810.0323
- Meiksin A., White M., Peacock J.A., 1999, MNRAS, 304, 851
- Meneux B. et al., 2006, A&A, 452, 387

- Moore B., et al., 1999, ApJ, 524, L19
- Munari, U., et al., 2005, A&A, 442, 1127
- Muñoz R. R., et al., 2005, ApJ, 631, L137
- Newman G., 2008, arxiv : 0805.1409
- Norberg P. et al. (the 2dFGRS Team), 2002, MNRAS, 332, 827
- Peacock J.A. et al., 2001, Nature, 410, 169
- Peacock J.A. et al., 2006, ESA-ESO report, arxiv:astro-ph/0610906
- Peacock J.A., Smith R.E., 2000, MNRAS, 318, 1144
- Percival W.J. et al., 2007, MNRAS, 381, 1053
- Perlmutter S. et al., 1999, ApJ, 517, 565
- Quillen A. C., 2002, AJ, 124, 722
- Rassat A. et al., 2008, arXiv :0810.0003
- Recio-Blanco, A., Bijaoui, A. & de Laverny, P. 2006, MNRAS, 370, 141
- Riess A. et al., 1998, AJ, 116, 1009
- Ross N.P. et al., 2007, MNRAS 381, 573
- Saito S., Takada M., Taruya A., 2008, Phys. Rev. Lett., 100, 191301
- Sawicki I., Carroll S., 2005, astro-ph/0510364
- Scoccimarro R., 2004, Phys. Rev. D, 70, 083007
- Seljak U., 2000, MNRAS, 318, 203
- Seo H.-J., Eisenstein D.J., 2003, ApJ, 598, 720
- Seo H.-J., Eisenstein D.J., 2005, ApJ, 633, 575
- Seo H.-J., Eisenstein D.J., 2007, ApJ, 665, 14
- Shapley, A. et al. (2005)
- Simpson F., Bridle S., 2006, Phys. Rev. D73, 083001
- Spergel D. et al., 2003, ApJ Suppl., 148, 175
- Spergel D. et al., 2006, astro-ph/0603449
- Springel V. et al., 2005, Nature 435, 629
- Takada M., Komatsu E., Futamase T., 2006, Phys. Rev. D, 73, 083520
- Trotta R., Bower R., 2006, arXiv:astro-ph/0607066
- Verde L. et al., 2002, MNRAS, 335, 432
- Walker, M. G., Mateo, M. & Olszewski, E. W. 2008, ApJ, 688, L75
- Wild V., Hewett P.C., 2005, 358, 1083
- Wild, V., Hewett, P.C., MNRAS, 358, 1083 (2005)
- Wilkinson M.I., et al., 2004, ApJ, 611, L21
- Wilkinson M.I., Evans, N.W., 1999, MNRAS, 310, 645

Willman B., et al., 2005, ApJ, 626, L85

Zoccali M., et al, 2003, A&A, 399, 931

Zoccali, M. et al 2006, A&A, 457, L1

Zwitter, T. et al 2008, AJ, 136, 421

11 ACRONYMS AND ABBREVIATIONS

1D	One-Dimensional
2dF	The 2 Degree Field instrument
2dFDR	2dF Data Reduction
2dFGRS	The 2dF Galaxy Redshift Survey
3D	Three-Dimensional
A&G	Acquisition and Guiding
A/R	Antireflection
AAO	Anglo-Australian Observatory
AAT	Anglo-Australian Telescope
ACSIS	Auto-Correlation Spectrometer and Imaging System
ACTDP	Advanced Cryocooler Technology Development Programs
AD	Applicable Document
ADC	Atmospheric Dispersion Compensator
ADU	Analog-to-Digital Unit
AES	Auger Electron Spectroscopy
AF2	Auto-fib2
AG	Autoguider
AGC	Acquisition and Guidance Camera
AIV	Assembly, Integration, and Verification
ALMA	Atacama Large Millimeter Array
AMNH	American Museum of Natural History
ANA	Analysis workstation
AO	Adaptive Optics
APD	Astronomy and Physics Directorate (JPL)
APG	Annealed Pyrolytic Graphite
API	Application Programming Interface
APS	Alignment and Phasing System
AR	Antireflection
ARC	Astronomical Research Cameras
ARGOS	Abundance and Radial Velocity Galactic Origins and Structure Survey
ARL	Applied Research Laboratory
ARR	Acceptance Readiness Review
ATC	Astronomy Technology Centre
ATP	Acceptance Test Plan
AURA	Association of Universities for Research in Astronomy
BAO	Baryonic Acoustic Oscillations
BBAR	Broadband AR
bHROS	Bench-mounted High Resolution Optical Spectrograph (Gemini)
BIT	Built in Test
BOM	Bill of Material
BOSS	Baryon Oscillation Spectroscopic Survey
BRI	Standard photometric bands (Johnson)
CAD	Computer-Aided Design
Caltech	California Institute of Technology
CAS	Central Alarm System
CCB	Change Control Board
CCD	Charge-Coupled Device
CCW	Counter-Clockwise
CDD	Concept Design Documentation

CDR	Critical Design Review
CELT	California Extremely Large Telescope
CFHT	Canada-France-Hawaii Telescope
CGS4	Cooled Grating Spectrometer 4
CIB	Configuration Implementation Board
CIRPASS	Cambridge Infrared Panoramic Survey Spectrograph
CIT	California Institute of Technology
CL	Center Line; <i>also</i> confidence level
CLD	Center for Life Detection
CM	Configuration Management
CMB	Cosmic Microwave Background
CMII	Configuration Management II
CMM	Coordinate Measuring Machine
CMOS	Complementary Metal Oxide Semiconductor
CMP	Configuration Management Plan
CMS	Configuration Management System
CNC	Computer Numerical Control
COB	Chip on Board
CoDR	Concept Design Review
COO	Caltech Optical Observatories
CosmoMC	A Markov-Chain Monte-Carlo software package
COTS	Commercial-Off-the-Shelf
CPU	Central Processing Unit
CR	Change Request; <i>also</i> Cosmic Ray
CRB	Configuration Review Board
CSRP	Center for Space Research Programs
CTE	Charge Transfer Energy
CTIO	Cerro Tololo Inter-American Observatory
CTM	Contract Technical Manager
CV	Curriculum Vitae
CVD	Chemical Vapor Deposition
CW	Clockwise
DAQtk	Data Acquisition Toolkit
DAZLE	Dark Age Z Lyman-alpha Explorer
DBSP	Double Spectrograph at Hale 200" Cass focus
DC	Direct Current
DCS	Detector Control Software
DE	Dark Energy
DEC	Declination
DEHZ	Dark Energy, High z / High Redshift Dark Energy
DE-HZ	Dark Energy, High z / High Redshift Dark Energy
DEIMOS	Deep Imaging Multi-Object Spectrograph (Keck)
DELZ	Dark Energy, Low z / Low Redshift Dark Energy
DETF	Dark Energy Task Force
DHS	Data Handling System
DID	Data Item Description
DLD	Digital Logic Decoder
DMA	Direct Memory Access
DoD	Department of Defense
DOE	Department of Energy
DOF	Degrees of Freedom

DOORS	Dynamic Object Oriented Requirements System
DPM	Deputy Project Manager
DR	Data Reduction
DRR	Design Release Review
DS	Data Set
DSP	Digital Signal Processor
E2V	e2v Technologies PLC, Essex, England
ECN	Enterprise Change Notice; <i>also</i> Engineering Change Notice
ECoS	Eberly College of Science
EGSE	Electrical Ground Support Equipment
ELT	Extremely Large Telescope
EM	Engineering Model
EMC	Electromagnetic Compatibility
EMI	Electromagnetic Interference
ESA	European Space Agency
ESD	Electro-Static Discharge
ESO	European Southern Observatory
EU	European Union
FAR	Final Acceptance Review
FEA	Finite Element Analysis
FIS	Fiducial Illumination System
FITS	Flexible Image Transport System
FLAMES	Fiber Large Array Multi Element Spectrograph
FLCG	Field Lens Collimator Group
FMEA	Failure Modes Effects and Analysis
FMOS	Faint Multi-Object Spectrograph
FOCCOS	Fiber Optical Cable and Connector System
FOV	Field of View
FPC	Fiber Positioner Controller
FPGA	Field-Programmable Gate Array
FPRD	Functional Performance Requirements Document
FRD	Focal Ratio Degradation
FRS	Fiber Routing System
FS	Feasibility Study; <i>also</i> Frame Set
FSL	Frequency Standards Laboratory
FTE	Full-Time Equivalent
Fundep	Fundação de Desenvolvimento da Pesquisa
FWHM	Full Width at Half Maximum
GA	Galactic Archaeology
GAHR	Galactic Archaeology–High Resolution / High Resolution Galactic Archaeology
GA-HR	Galactic Archaeology–High Resolution / High Resolution Galactic Archaeology
Gaia	An ESA-led astrometry space mission
GALEX	Galaxy Evolution Explorer
GALR	Galactic Archaeology–Low Resolution / Low Resolution Galactic Archaeology
GA-LR	Galactic Archaeology–Low Resolution / Low Resolution Galactic Archaeology
GCal	Gemini Calibration Unit
Gen2	.Generation 2. (next generation Subaru Operations System Software (SOSS))
G-ICD	Gemini ICD
GMOS	Gemini Multi-Object Spectrograph
GOODS	Great Observatory Origins Deep Survey

GPI	Gemini Planet Imager
GPMC	Governing Program Management Council
GPol	Gemini Polarimeter
gri	Standard photometric bands (SDSS)
GRS	Galaxy Redshift Survey
GSA	Gemini Science Archive
GUI	Graphical User Interface
H/W	Hardware
HALT	Highly Accelerated Life Test
HASS	Highly Accelerated Stress Streening
HETDEX	Hobby Eberly Telescope Dark Energy Experiment
HOMER	High Altitude Ozone Monitoring Experimental Rocket
HR	High Resolution
HRNIRS	High Resolution Near Infrared Spectrograph
HSC	HyperSuprimeCam
HTTP	Hypertext Transfer Protocol
I&T	Integration and Test
ICD	Interface Control Document
ICM	Institute of Configuration Management
ICS	Instrument Control Software
IFS	Integral Field Spectrograph
IFU	Integral Field Unit
IoA	Institute of Astronomy (Cambridge)
IP	Internet Protocol
IPAC	Infrared Processing and Analysis Center
IR	Infrared
IRAF	a library of astronomical data reduction software
IRMOS	Infrared Multi-Object Spectrograph
IRR	Integration Readiness Review
IS	Investigation Scientist; <i>also</i> Information System
ISOCAM	Infrared Space Observatory Camera
ISW	Integrated Sachs-Wolfe
IT	Information Technology
ITL	Imaging Technology Laboratory, University of Arizona
ITO	Indium Tin Oxide
IVOA	International Virtual Observatory Alliance
JAC OT	Joint Astronomy Center Observing Tool
JCMT	James Clerk Maxwell Telescope
JFET	Junction Field Effect Transistor
JHU	Johns Hopkins University
JPL	Jet Propulsion Laboratory
JWST	James Webb Space Telescope
K.A.O.S.	Kilo-Aperture Optical Spectrograph
KIDS	Kilo-Degree Survey
KPP	Key Performance Parameter
KVM-o-IP	Keyboard, Video, Mouse over Internet Protocol
LARS	Laboratory for Reliable Software
LBL	Lawrence Berkeley Laboratory
LBNL	Lawrence Berkeley National Laboratories
LDB	Logic Decoding Board
LED	Light-Emitting Diode

LFC	The Palomar Large-Format Camera
LGS	Laser Guide Star
LISA	Laser Interferometer Space Antenna
LNA	Laboratório Nacional de Astrofísica
LOE	Level of Effort
LR	Low Resolution
LRIS	Low Resolution Imaging Spectrometer
LRU	Line Replaceable Unit
M1CS	M1 Control System
M ³	Moon Mineralogy Mapper
MATLAB	Programming language for technical computing from The MathWorks
MAXR	The maximum resolution spectrograph mode
MBE	Molecular Beam Epitaxy
MCT	Ministry of Science and Technology
MDD	Mechanical Design Description
MDL	Micro Devices Laboratory
ME	Mechanical Engineer
Michelle	Mid-Infrared Echelle Spectrograph
MIP	Material Inventory Plan
MIRI	Mid-Infrared Instrument
MLS	Microwave Limb Sounder
MMR	Monthly Management Review
MMT	Multiple Mirror Telescope
MNRAS	Monthly Notices of the Royal Astronomical Society
MOE	Measure of Effectiveness
MOP	Measure of Performance
MOS	Multi-Object Spectrograph
MOSFET	Metal Oxide Semiconductor Field Effect Transistor
MPO	Multi-Fiber Push-on (a type of fiber optic connector)
MPS	Movement Planning Software
MRO	Mars Reconnaissance Orbiter
MROI	Magdalena Ridge Optical Interferometer
MRR	Make Release Review; <i>also</i> Manufacture Readiness Review
MS	Mechanical Specification
MT	Media-termination (a type of connector)
MTBF	Mean Time Between Failures
MTHR	Moderate to High Resolution Spectrograph
MTO	Motor Toggle Order
MUSE	Multi-Object Spectroscopic Explorer (ESO VLT)
N&S	Nod and Shuffle
NA	Not Applicable; <i>also</i> Numerical Aperture
NAOJ	National Astronomical Observatory of Japan
NAS	Network Attached Storage
NASA	National Aeronautics and Space Administration
NDEAA	Nondestructive Evaluation and Advanced Actuators
NIR	Near-Infrared
NOAO	National Optical Astronomy Observatory
NSCAT	NASA Scatterometer
NSF	National Science Foundation
NST	New Scale Technologies
OBCP	Observation Control Processor

OBS	Operational Business Schedule
OCD	Operational Concept Design
OCDD	Operational Concept Design Document; <i>also</i> Operational Concepts Definition Document
OCS	Observatory Control System; <i>also</i> Observation Control Software
OD	Optical Designer; <i>also</i> Outer Diameter
OFHC	Oxygen Free High Conductivity
OFS	Fiber connector manufacturer
OG	Output Gate
OIO	Oliveira Instrumentos Opticos
OLDP	On-Line Data Processing
OPE	Observation Procedure Editor
ORB	Orbital Sciences
ORR	Operations Readiness Review
OSL	Optical Science Laboratory
OSM	Object Selection Mechanism
OWS	Observation Workstation
OzPoz	A fiber positioner unit for the Very Large Telescope (VLT)
P2PP	Phase 2 Proposal Preparation
PALM-LGS	Palomar Laser Guide Star
PanSTARRS	Panaromic Survey Telescope and Rapid Response System
PASP	Publications of the Astronomical Society of the Pacific
PBS	Product Breakdown Structure
PC	Personal Computer
PCA	Principal Component Analysis
PCB	Printed Circuit Board
PCD	Product Concept Design
PCI	A computer bus standard
PCO	Project Close Out
PDMS	Project Database Management System
PDR	Preliminary Design Review
PDS	Power Distribution System
PECVD	Plasma Enhanced CVD
PFC	Prime Focus Corrector
PFI	Prime Focus Instrument
PFU	Prime Focus Unit
PHSC	PFU from the HyperSuprimeCam
PI	Project Initiation; <i>also</i> Principal Investigator
PM	Project Manager
PMS	Project Master Schedule
POP	Program Operating Plan
POSM	Prismatic Object Selection Mechanism
PPARC	Particle Physics and Astronomy Research Council
PRA	Project Resource Analyst
PRS	Pipeline Reduction System
PS	Project Scientist
PSA	Project Schedule Analyst
PSE	Project System Engineer
PSF	Point Spread Function
PSR	Pre-Ship Review
PSU	Pennsylvania State University

PTFE	Polytetrafluoroethylene – Teflon
PTI	Palomar Testbed Interferometer
QA	Quality Assurance
QC	Quality Control
QE	Quantum Efficiency
QH	Quartz Halogen; <i>also</i> Quiet Hour
QTH	Quartz Tungsten Halogen
RA	Right Ascension
RAVE	Radial Velocity Experiment
RD	Reset Drain; <i>also</i> Reference Document
Req	Requirement
RFP	Request for Proposal
RM	Risk Management
RMS	Root Mean Square
ROE	Royal Observatory Edinburgh
ROI	Region of Interest
ROM	Rough Order of Magnitude
ROMPS	Robotically Manipulated Plug-Plate System
RR	Requirements Review
RSD	Redshift Space Distortions
RSS	Root Sum Squared
RTD	Resistance Temperature Detector; <i>also</i> Real Time Display
S/N	Signal to Noise
S/W	Software
SAA	Space Act Agreement
SAMP	Simple Application Messaging Protocol
SAN	Storage Area Network
SARR	System Architecture and Requirements Review
SC	Subprime Cam
SCP	Service Connection Point
SCUBA	Submillimeter Common-User Bolometer Array
SCUBA2	Submillimeter Common-User Bolometer Array 2
SDSS	Sloan Digital Sky Survey
SE	Systems Engineering
SEGUE	Sloan Extension for Galactic Understanding and Exploration
SHARAD	Shallow Radar
SIA	Simple Image Access
S-ICD	Subaru ICD
SIM	Space Interferometry Mission
SimCam	(a working name for the next generation instrument interface)
SIR-C	Spaceborne Imaging Radar–C
SIRR	System Integration Readiness Review
SKA	Square Kilometer Array
SKADS	Square Kilometre Array Design Studies
SNAP	SuperNova Acceleration Probe
SNR	Signal-to-Noise Ratio
SOAR	Southern Astrophysical Research Telescope
SOSS	Subaru Operations System Software
SOW	Statement of Work
SPEC	Specification
SPIE	Society of Photo-Optical Instrumentation Engineers

SPIRE	Spectral and Photometric Imaging Receiver
SPLAT	Spectral Analysis Tool
SQR	Rotary Squiggle Motors
SRB	Strain Relief Box
SRE	Spectral Resolution Element
SRF	Sequence Request File
SRL	Significant Risk List
SRR	System Requirements Review
SRS	Software Requirements Specification
SSA	SuperCosmos Science Archive
ST7	Space Technology 7
STARS	Subaru Telescope Archive System
STCS	Subaru TCS
STELAS	SOAR Telescope Echelle Spectrograph
STFC	Science and Technology Facilities Council
SUBARU	Subaru Telescope Archive System
SW	Software
SWIFT	Short Wavelength Integral Field Spectrograph
TBA	To Be Announced
TBC	To Be Confirmed
TBD	To Be Defined; <i>also</i> To Be Decided
TBR	To Be Reviewed
TCP	Transmission Control Protocol
TCS	Telescope Control System
TES	Top-End Structure
TFCALC	Software package used for designing thin films
ThAr	Thorium Argon
TIKI	Telescope Interface Kit
TIM	Technical Interchange Meeting
TMC	Technical and Management Committee
TMT	Thirty-Meter Telescope
TPF	Terrestrial Planet Finder
TPM	Technical Performance Measure
TUE	Top-End Unit Exchange
UARC	University Affiliated Research Center
UCL	University College London
UCLES	University College London Echelle Spectrograph
UK	United Kingdom
UK ATC	United Kingdom Astronomy Technology Centre
UKIRT	United Kingdom Infrared Telescope
USA	United States of America
USM	Ultrasonic Motor
UUV	Unmanned Undersea Vehicle
UV	Ultraviolet
UVES	UV-Visual Echelle Spectrograph
V	Volts
V&V	Verification and Validation
VCP	Verification and Commissioning Plan
VDD	Version Description Document
VIPERS	VIMOS Public Extragalactic Redshift Survey
VISTA	Visible and Infrared Survey Telescope for Astronomy

VISTAIR-CAM	VISTA Infrared Camera
VLT	Very Large Telescope
VME	Versa Module Europa
VNC	Virtual Network Computing
VO	Virtual Observatory
VPH	Volume Phased Hologram
VPHG	Volume Phase Holographic Grating
WBS	Work Breakdown Structure
WCS	WF MOS Control System
WCSE	WF MOS WCS Electronics
WFC	Wide Field Corrector
WFCAM	Wide-field camera (IR camera for UKIRT)
WF MOS	Wide Field Fiber-Fed Optical Multi-Object Spectrometer
WFS	Wavefront Sensor
WHT	William Herschel Telescope
WM	Work Month
WMAP	Wilkinson Microwave Anisotropy Probe
WWW	World Wide Web
WY	Work Year
WYFFOS	An intermediate dispersion spectrograph for the WHT
XML	Extensible Markup Language